

# **An Advancement in Electric Vehicle Battery Thermal Management with Innovative Cold Plate Designs**

## **THESIS**

Submitted in partial fulfilment  
of the requirements for the degree of  
**DOCTOR OF PHILOSOPHY**

by

**KOKKULA MONIKA**  
**ID. No. 2018PHXF0449H**

Under the Supervision of  
**Prof. SANTANU PRASAD DATTA**

**&**

Under the Co-Supervision of  
**Prof. SOUNAK ROY**  
**Dr. CHANCHAL CHAKRABORTY**



**BITS Pilani**  
Pilani | Dubai | Goa | Hyderabad

**BIRLA INSTITUTE OF TECHNOLOGY AND SCIENCE, PILANI**

**2024**

**BIRLA INSTITUTE OF TECHNOLOGY AND SCIENCE, PILANI**

**CERTIFICATE**

This is to certify that the thesis titled "**An Advancement in Electric Vehicle Battery Thermal Management with Innovative Cold Plate Designs**", submitted by Ms. **Kokkula Monika** ID No **2018PHXF0449H** for the award of Ph.D. of the Institute, embodies original work done by her under my supervision.

Signature of the Supervisor:

Name in capital letters: **Prof. SANTANU PRASAD DATTA**

Designation: **Associate Professor**

Date: **27.06.2024**

Signature of the Co-Supervisor:

Name in capital letters: **Prof. SOUNAK ROY**

Designation: **Professor**

Date: **27.06.2024**

Signature of the Co-Supervisor:

Name in capital letters: **Dr. CHANCHAL CHAKRABORTY**

Designation: **Assistant Professor**

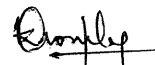
Date: **27.06.2024**

# BIRLA INSTITUTE OF TECHNOLOGY AND SCIENCE, PILANI

## Declaration

I hereby declare that

- a. The work contained in the thesis is original and has been done by myself under the general supervision of my supervisors.
- b. The work has not been submitted to any other institute for any degree or diploma.
- c. I have followed the guidelines provided by the institute in writing the thesis.
- d. I have conformed to the norms and guidelines given in the Ethical Code of Conduct of the Institute.
- e. Whenever I have used materials (data, theoretical analysis, and text) from other sources, I have given due credit to them by citing them in the text of the thesis and giving their details in the references.



---

**Kokkula Monika**  
(Doctoral Candidate)  
Department of Mechanical Engineering  
BITS Pilani Hyderabad Campus  
Hyderabad-500078, India.

# ACKNOWLEDGEMENTS

---

---

As I reflect upon the odyssey of my doctoral research, a profound sense of gratitude envelops me to extend sincere acknowledgements to all the people who have significantly contributed to various aspects of my life and, crucially, to the realization of this doctoral dissertation.

I would like to express my sincere indebtedness and heartiest regards to my esteemed supervisors, Prof. Santanu Prasad Datta from the Department of Mechanical Engineering, Prof. Sounak Roy and Dr. Chanchal Chakraborty from the Department of Chemistry. Their unwavering encouragement, consistent support, and effective guidance were indispensable at various stages of my research, shaping the contours of this dissertation. Their insightful advice and innovative perspectives played a pivotal role in steering this work towards its fruitful culmination.

Further, I am highly grateful to my doctoral advisory committee members, namely Prof. Sandip S. Deshmukh and Prof. Jalaiah Nandanavanam from the Department of Mechanical Engineering, for their valuable comments and constructive criticism to enhance the quality of my research. I extend my appreciation to Prof. N. Suresh Kumar Reddy (Head of the Department, Department of Mechanical Engineering), Prof. Alivelu Manga Parimi (Associate Dean, Academic Graduate Studies and Research Division), Prof. G. Sundar (Former Director, BITS Pilani, Hyderabad Campus), Prof. Soumyo Mukherji (Director, BITS Pilani, Hyderabad Campus) and Prof. V. Ramgopal Rao (Vice-Chancellor, BITS Pilani, Hyderabad Campus) for providing a creative and enriching research atmosphere.

## Acknowledgements

---

I would like to thank Marri Bhasker Reddy, Chandra Shekar, Murali N, Sreedhar, Mahendra Chary, Biswal, and all other Central workshop technicians for their excellent cooperation throughout my research work. I am also thankful to Tahsildar Yadav associated with the Heat transfer lab. I also acknowledge the institute's electrical and general maintenance divisions for their timely assistance.

I sincerely acknowledge my junior and fellow lab members, Suresh and Joshua, for their help in setting up the experimental test rig. My warm thanks to Trivedi GVN, Shivangi Joshi, and Rohit Jha for providing a joyous, comfortable, and friendly environment in BITS. I would also like to thank Dr. Ramayee, Sitaram and all other research scholars in my department for their company and assistance in various ways.

I would like to express my heartfelt regards and gratitude to my most affectionate parents, Kokkula Ramesh and Suvarna, for their trust, support, and blessings throughout my life's journey and for their great desire to see me succeed. Warm regards to my sister, Chandra Lekha, for her unconditional love and support. Finally, a special thanks to Phani Vivek, who went through hard times together, cheered me on and celebrated each accomplishment.

Above all, I am grateful to the Almighty, who gave me self-confidence, ability and strength to complete this work.

**Kokkula Monika**

## ABSTRACT

---

---

The present dissertation makes contributions in two distinct domains of battery thermal management. The first step involves an in-depth evaluation of a mini-channelled cold plate for liquid cooling integrated with a battery simulator. Subsequently, the liquid cooling approach is enhanced particularly by modifying and optimizing the cold plate designs and regulating the temperature of the battery module within the safe operating range of 25 °C to 40 °C through simulation.

Initially, an experimental test facility emulating heating conditions of a 20Ah pouch battery using cartridge heaters and an ingeniously designed rectangular mini-channelled cold plate is developed. A wide range of operating conditions such as coolant temperature, flow rate and flow direction are varied to identify the parameters affecting the effectiveness of a cold plate.

Transitioning into the computational realm, a three-dimensional conjugate heat transfer model is deployed to solve the electrochemical-thermal reactions of a pouch battery module using COMSOL Multiphysics software. Six distinct mini-channel designs, including serpentine, U-bend, straight, pumpkin, spiral, and hexagonal, are designed and compared with a constant channel volume. Their cooling ability is evaluated by considering several performance factors such as pressure drop across the cold plate,  $j/f$ , average temperature across the module and cooling performance factor for varying mass flow rates and a fixed discharge rate of 3C. Also, realistic drive cycle data US06 is utilized to assess one of the best designs i.e. hexagonal channel-based battery module performance for on-road driving conditions. However, it is imperative to develop a design that simultaneously

balances the response parameters by minimizing maximum temperature, pressure drop and enhancing heat dissipation.

Keeping this in view, an optimization technique is applied to one of the best designs i.e. hexagonal channel. The sample points are initially generated by Latin Hypercube sampling based on the upper and lower bound limit of design variables such as side length ( $L$ ), channel width ( $W_c$ ), branching angle ( $\theta$ ), mass flow rate ( $m_w$ ) and coolant temperature ( $T_{w,in}$ ). Later, COMSOL Multiphysics is utilized to compute the response parameters. Later, a systematic comparison of prediction models such as Multi Linear Regression, Response Surface approximation, Support Vector Machine and Kriging methods is conducted to find the best one. A design satisfying all the above-said criteria is obtained by applying multi-objective optimization techniques NSGA II followed by a K-means clustering algorithm. By the end, an optimized hexagonal channel design with  $L = 18.99$  mm,  $W_c = 4.99$  mm,  $\theta = 91.51^\circ$ , and  $T_{w,in} = 25.04$  °C is attained. Alongside, the SHAP technique is applied to understand the behaviour of the best prediction model i.e. Kriging by visualizing it.

In pursuit of innovation, a novel cold plate embedded with Multi Stage Tesla Valve design has been developed to provide a safer operating temperature range for pouch batteries. The cold plate performance is evaluated by thoroughly examining different design parameters, utilizing COMSOL Multiphysics software.

**Keywords:** Pouch battery; Thermal management; Liquid cooling; Mini channel; Simulation; Optimization; Multi-Stage Tesla Valve.

# TABLE OF CONTENTS

---

---

CERTIFICATE .....	II
DECLARATION.....	III
ACKNOWLEDGEMENTS.....	IV
ABSTRACT.....	VI
LIST OF TABLES.....	XIII
LIST OF FIGURES.....	XV
LIST OF ABBREVIATIONS.....	XIX
LIST OF SYMBOLS.....	XXI

## CHAPTER I: INTRODUCTION AND LITERATURE REVIEW

<b>1.1 Electrification of automobiles .....</b>	<b>1</b>
1.1.1 Working Principle of Li-ion battery .....	2
<b>1.2 Battery thermal management system.....</b>	<b>3</b>
1.2.1 Thermal issues in Li-ion batteries .....	3
1.2.2 Comparison of BTMS and challenges.....	6
1.2.3 Liquid Cooling .....	9
<b>1.3 Approach for BTMS.....</b>	<b>10</b>
1.3.1 Experimental investigation.....	10
1.3.2 Numerical investigation .....	11
<b>1.4 Comparison of different cooling channel designs .....</b>	<b>15</b>



## Table of Contents

1.5	Optimization through surrogate models and NSGA II .....	17
1.6	Introducing novel Tesla design .....	20
1.7	Research gaps .....	21
1.8	Objectives of the thesis .....	21
1.9	Organization of the thesis .....	22

### CHAPTER 2: EXPLORE THE EFFICACY OF INDIRECT LIQUID COOLING APPROACH WITH MINI CHANNEL COOL PLATES FOR POUCH CELLS

2.1	Introduction .....	24
2.2	Experimental test facility .....	25
2.2.1	System description .....	25
2.2.2	Uncertainty analysis .....	28
2.2.3	Experimental strategy .....	30
2.3	Data reduction .....	30
2.4	Results and discussions .....	31
2.4.1	Effect of varying heat load .....	32
2.4.2	Effect of varying coolant temperature .....	33
2.4.3	Effect of varying flow rate .....	36
2.4.4	Effect of varying flow direction .....	40
2.4.5	Effect of pulse load test on cooling effectiveness .....	41
2.5	Summary .....	44

### CHAPTER 3: COMPARATIVE ASSESSMENT AMONG SEVERAL CHANNEL DESIGNS WITH CONSTANT VOLUME FOR COOLING OF POUCH-TYPE BATTERY MODULE

3.1	Introduction .....	45
3.2	Methodology .....	47
3.2.1	Physical problem .....	47
3.2.2	Proposed channel configurations .....	49
3.2.3	Control equations .....	50

## Table of Contents

3.2.4	Boundary conditions .....	54
3.2.5	Numerical method.....	55
3.2.6	Grid sensitivity .....	57
3.2.7	Model validation .....	58
<b>3.3</b>	<b>Results and discussion .....</b>	<b>60</b>
3.3.1	Distribution characteristics of various channel designs.....	60
3.3.2	Influence of mass flow rate on channel configuration.....	67
3.3.3	Effect of ambient temperature on cooling effectiveness .....	73
3.3.4	Real-time performance investigation with a standard drive cycle data .....	77
<b>3.4</b>	<b>Summary .....</b>	<b>79</b>
<b>CHAPTER 4: OPTIMIZE THE SIZING AND RATING PARAMETERS OF THE IDEAL COLD PLATE THROUGH SURROGATE MODELS AND NSGA II</b>		
<b>4.1</b>	<b>Introduction.....</b>	<b>81</b>
<b>4.2</b>	<b>Problem definition .....</b>	<b>83</b>
<b>4.3</b>	<b>Optimization techniques.....</b>	<b>84</b>
4.3.1	Design variables .....	84
4.3.2	Response parameters .....	85
4.3.3	Latin hypercube sampling .....	85
4.3.4	Surrogate models.....	86
4.3.5	Hyperparameter tuning.....	89
4.3.6	Multi-objective optimization .....	89
<b>4.4</b>	<b>Results and discussion .....</b>	<b>93</b>
4.4.1	Grid convergence .....	93
4.4.2	Experimental validation of the ECT model.....	94
4.4.3	Effect of discharge rate on cooling effectiveness .....	96
4.4.4	Accuracy analysis of ML models .....	98
4.4.5	Optimization results and verification .....	100
4.4.6	Feature importance using SHAP .....	104
4.4.7	Comparative analysis .....	107
<b>4.5</b>	<b>Summary .....</b>	<b>110</b>

## Table of Contents

### CHAPTER 5: INTRODUCING AN INNOVATIVE COLD PLATE DESIGN WITH MULTI-STAGE TESLA VALVE FOR ENHANCED COOLING OF POUCH-TYPE LI-ION BATTERIES

<b>5.1</b>	<b>Introduction.....</b>	<b>112</b>
<b>5.2</b>	<b>Methodology .....</b>	<b>114</b>
5.2.1	Model and analysis.....	114
5.2.2	Boundary conditions .....	116
5.2.3	Assumptions .....	116
5.2.4	Governing equations .....	117
5.2.5	Data reduction .....	118
5.2.6	Validation of the model.....	119
5.2.7	Grid independence test .....	120
<b>5.3</b>	<b>Results and discussion .....</b>	<b>121</b>
5.3.1	Comparison of straight channel design with MSTV forward and reverse flow directions.....	121
5.3.2	Effect of channel number .....	126
5.3.3	Effect of valve-to-valve distance.....	130
5.3.4	Effect of channel width .....	132
5.3.5	Effect of outer curve radius .....	135
5.3.6	Effect of valve angle .....	140
5.3.7	Comparison of optimized hexagonal channel design with MSTV .....	141
<b>5.4</b>	<b>Summary .....</b>	<b>142</b>
<b>CHAPTER 6: CONCLUSIONS AND SCOPE OF FUTURE RESEARCH</b>		
<b>6.1</b>	<b>Conclusions.....</b>	<b>144</b>
6.1.1	Develop an experimental test facility .....	145
6.1.2	Comparison of different channel designs .....	146
6.1.3	Optimization through Surrogate Models and NSGA-II.....	146
6.1.4	Introducing a novel channel design.....	147
<b>6.2</b>	<b>Scope of Future Work .....</b>	<b>148</b>
	<b>REFERENCES.....</b>	<b>150</b>
	<b>APPENDIX A.....</b>	<b>159</b>

Table of Contents

---

**LIST OF PUBLICATIONS.....163**

**BRIEF BIOGRAPHY OF THE CANDIDATE.....166**

**BRIEF BIOGRAPHY OF THE SUPERVISOR.....167**

**BRIEF BIOGRAPHY OF THE CO-SUPERVISOR.....168**

**BRIEF BIOGRAPHY OF THE CO-SUPERVISOR.....169**

## LIST OF TABLES

---

---

Table 1.1: Li-ion battery fire incidents (information adapted from different internet websites) .....	5
Table 1.2: Summary of the available literature to design an energy-efficient BTMS .....	8
Table 1.3: List of EVs with liquid cooling .....	9
Table 1.4: Summary of available literature on different battery ECT models.....	14
Table 1.5: Summary of available literature on MOO applied to IDC approach.....	16
Table 2.1: Cold plate dimensions.....	28
Table 2.2: Specifications and accuracy of the instruments used in the present work.....	29
Table 2.3: Performance metrics of the cooling system with the variation of coolant temperature .....	36
Table 2.4: Performance metrics of the cooling system with the variation of $\dot{V}$ .....	38
Table 2.5: Performance metrics of the cooling system with the variation of flow direction .....	41
Table 3.1: Technical specifications of the pouch cell.....	48
Table 3.2: Dimensions of mini channels in the cold plate .....	50
Table 3.3: Thermal properties of coolant and cold plate (Huo <i>et al.</i> 2015).....	54
Table 3.4: Thermo-physical properties used for the present simulation (S. Panchal <i>et al.</i> 2017) .....	56
Table 3.5: Material and thermal properties.....	56
Table 3.6: Summary of mesh independence test results for a battery module integrated with different cooling channel designs at a $\dot{m}_w$ of 0.002 kg s <sup>-1</sup> .....	58
Table 3.7: Variation in $D_h$ , $Re$ and $L_{ch}$ for different designs under constant flow volume at a $\dot{m}_w$ of 0.002 kg s <sup>-1</sup> .....	60
Table 3.8: $\Delta P$ across the inlet and outlet of cooling plate with different channel designs for varying $\dot{m}_w$ .....	68
Table 4.1: Design variables and bound spaces .....	84
Table 4.2: Settings for MOGA.....	91

## List of Tables

---

Table 4.3: Grid independence results.....	94
Table 4.4: Metrics for the different ML models trained using the dataset A.....	98
Table 4.5: Comparison between numerical and Kriging-RBF predicted values for the obtained Pareto optimal solutions.....	102
Table 4.6: Evaluation of the optimal design with the initial design under a $\dot{m}_w$ of 0.003 kg s <sup>-1</sup> .....	109
Table 5.1: Cold plate parameters .....	115
Table 5.2: Comparison of numerical results with experimental results of (Gamboa <i>et al.</i> 2005).....	120
Table 5.3: Comparison of straight channel design, forward and reverse direction in MSTV at varying $Re$ .....	123
Table 5.4: Performance of reverse flow direction in MSTV for different design parameters .....	128
Table 5.5: Comparison of optimized hexagonal channel design with MSTV .....	142

# LIST OF FIGURES

---



---

Fig. 1.1: Augmentation of a Li-ion battery pack and corresponding drive-train of an EV	2
Fig. 1.2: Schematic representation of a single pouch-type LiFePO <sub>4</sub> battery cell and its cross-sectional view .....	3
Fig. 1.3: Typical fire accidents (Feng <i>et al.</i> 2018).....	5
Fig. 1.4: Schematic of various battery cooling systems (Kim <i>et al.</i> 2019).....	6
Fig. 2.1: Schematic layout of the experimental test set-up .....	26
Fig. 2.2: Pictorial view of the test facility.....	26
Fig. 2.3: Exploded view of the test section.....	27
Fig. 2.4: Dimensions of mini-channel captured using VMM .....	27
Fig. 2.5: Variation of temperature across the test module for varying heat load.....	32
Fig. 2.6: Variation of temperature across the test module for different $T_{w,in}$ .....	34
Fig. 2.7: Variation of $h_w$ across the test module for different $T_{w,in}$ .....	35
Fig. 2.8: Variation of temperature across the test module for different $\dot{V}$ .....	36
Fig. 2.9: Variation of $h_w$ across the test module for different $\dot{V}$ .....	37
Fig. 2.10: Effect of varying $\dot{V}$ on the heat transfer and pressure drop across an aluminium flat tube in cold plate.....	39
Fig. 2.11: Schematic representation of different flow arrangements across the channels	40
Fig. 2.12: Variation of temperature across the test module for different flow direction ..	41
Fig. 2.13: Sampling curve of pulse load test.....	42
Fig. 2.14: Variation of temperature and heat flux across the test module with and without cooling under pulse load test.....	43
Fig. 2.15: Thermal images of the test module captured on heating at different time intervals under pulse load test.....	43
Fig. 3.1: (a) Battery module embedded with cold plate and (b) Schematic diagram of a battery module integrated with the hexagonal channel design cold plate. ....	48
Fig. 3.2: Models of six different cooling plate designs.....	49
Fig. 3.3: Flow chart representing the simulation procedure .....	55

## List of Figures

---

Fig. 3.4: Mesh independence test results of a straight channel design .....	58
Fig. 3.5: Comparison between numerical and experimental results of a single battery ...	59
Fig. 3.6: Velocity contours at the mid-profile plane of different channel designs for a $\dot{m}_w$ of 0.002 kg s <sup>-1</sup> .....	61
Fig. 3.7: Pressure contours at the mid-profile plane of different channel designs for a $\dot{m}_w$ of 0.002 kg s <sup>-1</sup> .....	63
Fig. 3.8: Temperature profile across the surface of battery 2 with various channel designs for a $\dot{m}_w$ of 0.002 kg s <sup>-1</sup> .....	66
Fig. 3.9: Influence of $\dot{m}_w$ on $j/f$ factor for various channel designs .....	69
Fig. 3.10: Influence of $\dot{m}_w$ on $T_{avg}$ across the battery module for various channel designs.	70
Fig. 3.11: Influence of $\dot{m}_w$ on $\beta$ for various channel designs .....	72
Fig. 3.12: Influence of $\dot{m}_w$ on the cooling effectiveness of various channel designs .....	73
Fig. 3.13: Temperature profile across the surface of battery 2 ( $y = 9.25$ mm) for a $T_a$ of 35 °C along the (a, b) z-direction for different x locations, and (c, d, e) x-direction for different z locations .....	75
Fig. 3.14: Temperature distribution across the battery 2 with various channel designs for a $T_a$ of 35 °C.....	76
Fig. 3.15: (a) Current profile of US06 high way driving cycle ('+ sign' represents charging and '- sign' represents discharging) (b) Voltage distribution under US06 drive cycle .....	77
Fig. 3.16: Variation of local temperature across the surface of battery 2 integrated with hexagonal channel cold plate under US06 drive cycle. ....	78
Fig. 4.1: Optimization workflow based on simulations and NSGA-II .....	92
Fig. 4.2: Mesh model of the computational domain .....	93
Fig. 4.3: Variation in current and voltage concerning time during the cycle test.....	95
Fig. 4.4: Variation of (a) temperature at different locations and (b) heat flux at the central region of the battery .....	96
Fig. 4.5: Validation of numerical results with the experiment for varying discharge rate	96
Fig. 4.6: (a) Change in the discharge voltage and (b) average temperature for different discharge rates.....	97
Fig. 4.7: Parity plot of randomly tested data for different ML models.....	99



## List of Figures

---

Fig. 4.8: Pareto optimal (blue) and representative solutions (red) obtained using NSGA II and K-means clustering, respectively .....	101
Fig. 4.9: Temperature contours across the mid-plane of the cooling plate and battery module for the Variants A, B and C .....	103
Fig. 4.10: (a) Bees warm plot (on the top) and (b) summary bar plot (on the bottom) to determine feature impact using Kriging model output on $T_{\max}$ .....	105
Fig. 4.11: Feature impact using Kriging model output on $\Delta P$ .....	106
Fig. 4.12: Feature impact using Kriging model output on $h_w$ .....	106
Fig. 4.13: Comparison of $\Delta P$ and $h_w$ for (a, b) Variant A, (c, d) Variant B, and (e, f) Variant C with the initial design for varying $\dot{m}_w$ .....	108
Fig. 5.1: (a) A 3D cold plate with MSTV design and (d) Sectional view of cooling plate representing a reverse flow in MSTV .....	115
Fig. 5.2: Mesh model of the cold plate .....	120
Fig. 5.3: Variation of (a) $T_{\max}$ and (b) $T_{\sigma}$ across straight channel design, forward and reverse flow direction in MSTV .....	122
Fig. 5.4: Pressure, velocity and temperature contours for straight channel design, forward and reverse flow direction in MSTV for $Re$ of 4000 .....	124
Fig. 5.5: Closer view of velocity contours at $Re = 4000$ (brighter colour: high velocity, lighter colour: low velocity) encountered in (a) forward flow MSTV, and (b) reverse flow MSTV .....	125
Fig. 5.6: Comparison of (a) $T_{\max}$ and (b) $T_{\sigma}$ across reverse flow direction in MSTV for varying channel number.....	127
Fig. 5.7: Evolution of temperature contours for reverse flow direction in MSTV at $Re$ 4000 for varying channel number .....	129
Fig. 5.8: Temperature profiles in the x-direction of cooling plate at different locations for (a) 2 channels, (b) 3 channels and (c) 4 channels .....	130
Fig. 5.9: Comparison of (a) $T_{\max}$ and (b) $T_{\sigma}$ across 4-channelled cold plate with reverse flow direction in MSTV for varying $G$ .....	131
Fig. 5.10: Variation of (a) $T_{\max}$ and (b) $T_{\sigma}$ across MSTV cold plate with reverse flow for different $w_c$ and $Re$ .....	132

## List of Figures

---

Fig. 5.11: A closer view of velocity and pressure contours on the central $xy$ plane of cooling plate for varying $W_c$ at a $Re$ of 4000 .....	134
Fig. 5.12: Variation of $T_{\max}$ and $T_{\sigma}$ across MSTV cold plate with reverse flow for different $R$ and $Re$ .....	135
Fig. 5.13: A closer view of velocity and pressure contours on the central $xy$ plane of cooling plate for varying $R$ at a $Re$ of 4000 .....	136
Fig. 5.14: Temperature contours on the central $xy$ plane of cooling plate for varying $R$ at a $Re$ of 4000 .....	138
Fig. 5.15: Temperature profiles in the $x$ -direction at different locations for a $R$ of (a) 5.87 mm, (b) 7.05 mm, (c) 8.23 mm, and (d) 9.4 mm .....	139
Fig. 5.16: Variation of $T_{\max}$ and $T_{\sigma}$ across MSTV cold plate with reverse flow for different $\theta$ and $Re$ .....	140

## LIST OF ABBREVIATIONS

---

---

1D	=	One-dimensional
2D	=	Two-dimensional
3D	=	Three-dimensional
ABC	=	Artificial bee colony
ANN	=	Artificial neural networks
BBD	=	Box-benken design
BTMS	=	Battery thermal management system
CC	=	Constant charge
CCD	=	Central composite design
CFD	=	Computational fluid dynamics
C-rate	=	Discharge rate
CV	=	Constant voltage
DAQ	=	Data acquisition system
DC	=	Direct cooling
DOE	=	Design of experiments
DPT	=	Differential pressure transmitter
ECMs	=	Equivalent circuit models
ECT	=	Electro-chemical thermal
ESE	=	Evolutionary stochastic algorithms
EVs	=	Electric vehicles
GP	=	Genetic programming
GPR	=	Gaussian process regression
HEVs	=	Hybrid electric vehicles
HPT	=	Hyperparameter tuning
IDC	=	Indirect cooling
IR	=	Infra-red
LFP	=	Lithium iron phosphate
LHS	=	Latin hypercube sampling

## List of Abbreviations

---

LiFePO <sub>4</sub>	=	Lithium iron phosphate
MCDM	=	Multi-criteria decision-making methods
MCMB	=	Mesocarbon microbeads
ML	=	Machine learning
MLR	=	Multi-linear regression
MOGA	=	Multi-objective genetic algorithm
MOO	=	Multi-objective optimization
MSTV	=	Mutli-stage Tesla valve
Ni-Cad	=	Nickel cadmium
Ni-MH	=	Nickel metal hydride
NMAD	=	Normalized mean absolute deviation
NMAE	=	Normalized mean absolute error
NRSME	=	Normalized root mean square error
NSGA II	=	Non-dominated sorting genetic algorithm
NTGK	=	Neumann and Tiedmann, Gu and Kim
NVH	=	Noise vibration and harshness
PCMs	=	Phase change materials
POF	=	Pareto optimal frontier
PSO	=	Particle swarm optimization
RBF	=	Radial basis function
RH	=	Relative humidity
RSM	=	Response surface method
SA	=	Simulated annealing
SHAP	=	SHapley Additive exPlanations
STAR-CCM+	=	Computational continuum mechanics
SVM	=	Support vector machine
TR	=	Thermal runaway
VMM	=	Vision measuring machine

## LIST OF SYMBOLS

---

---

$A$	=	surface area ( $\text{m}^2$ )
$C_\mu$	=	empirical coefficient
$c_p$	=	specific heat at constant pressure ( $\text{J kg}^{-1} \text{ }^\circ\text{C}^{-1}$ )
$D_h$	=	hydraulic diameter (m)
$E$	=	open circuit voltage (V)
$E_{ij}$	=	mean deformation rate
$F$	=	Faraday constant
$f$	=	friction factor
$h$	=	heat transfer coefficient ( $\text{W m}^{-2} \text{ }^\circ\text{C}^{-1}$ )
$I$	=	current per unit volume ( $\text{A m}^{-3}$ )
$j$	=	Colburn factor
$k$	=	thermal conductivity ( $\text{W m}^{-1} \text{ }^\circ\text{C}^{-1}$ )
$L$	=	characteristic length (m)
$Nu$	=	Nusselt number
$P_{pump}$	=	pump power (W)
$P$	=	static pressure (Pa)
$P_h$	=	heat generation power (W)
$Pr$	=	Prandtl number
$R$	=	resistance ( $\Omega$ )
$Re$	=	Reynolds number
$t$	=	time (s)
$T$	=	static temperature ( $^\circ\text{C}$ )
$V$	=	operating voltage (V)
$\dot{V}$	=	volume flow rate ( $\text{m}^3 \text{ s}^{-1}$ )
$\dot{m}$	=	mass flow rate ( $\text{kg s}^{-1}$ )
$\dot{Q}$	=	heat generation rate (W)
$\bar{v}$	=	average velocity ( $\text{m s}^{-1}$ )

## List of Symbols

---

$\Delta S$	=	entropy change ( $\text{W } ^\circ\text{C}^{-1}$ )
$\Delta P$	=	pressure drop across the plate (Pa)

### Greek Letters

$\mu$	=	dynamic viscosity (Pa s)
$\varepsilon$	=	turbulent dissipation rate
$k$	=	turbulent kinetic energy
$\eta$	=	turbulent viscosity ratio
$\beta$	=	cooling performance factor
$\rho$	=	density ( $\text{kg m}^{-3}$ )
$\sigma$	=	standard deviation ( $^\circ\text{C}$ )
$\varphi$	=	Reynold's stress
$\omega$	=	velocity ( $\text{m s}^{-1}$ )
$\nabla$	=	gradient operator

### Subscripts/Superscripts

$a$	=	ambient
$avg$	=	average temperature
$b$	=	battery
$bm$	=	battery module
$ch$	=	channel
$cs$	=	cross-sectional
$ec$	=	electrochemical
$f$	=	fluid
$gen$	=	generation
$in$	=	initial
$j$	=	joule heat
$max$	=	maximum
$min$	=	minimum
$neg$	=	negative
$out$	=	outlet

## List of Symbols

---

<i>pos</i>	=	positive
<i>s</i>	=	Surface area
<i>sep</i>	=	separator
<i>w</i>	=	water
<i>w, in</i>	=	inlet temperature of coolant (°C)
<i>w, out</i>	=	outlet temperature of coolant (°C)





# Chapter 1

## Introduction and Literature Review

### Keywords

Li-ion battery;  
Liquid cooling;  
Thermal-  
management;  
Mini channel;  
Optimization;  
Tesla valve;

*This chapter provides a concise overview of thermal issues in electric vehicles as well as the need for implementing battery thermal management system. Investigations on the indirect liquid cooling approach stated in the open literature are summarized by highlighting the critical observations. Based on this, the research goals pertaining to the indirect cooling approach are identified. The objectives and their significant contributions to the thesis have also been deliberated upon.*

## 1.1 Electrification of automobiles

**G**lobally, the automotive industry is shifting towards a new paradigm, focussing on sustainable and green vehicles such as purely battery-driven electric vehicles (EVs) and hybrid electric vehicles (HEVs) (Cuma and Koroglu 2015). The primary aspect of developing a green vehicle is an energy storage unit capable of supporting rapid acceleration, deceleration, and fuel economy. Several rechargeable batteries like lead-acid, Ni-MH, Ni-Cad and Li-ion have been deployed to empower automotive drivetrains since the last two decades. Among them, the Li-ion battery acquired enormous recognition as a significant energy source unit for EVs and HEVs owing to their superior energy density (up to 750 Wh/L), power density (10,000 Wh/L), low self-discharge rate, enhanced life cycle, and environment friendliness (Zubi *et al.* 2018). These batteries come in different shapes and configurations, such as prismatic, pouch and cylindrical. Among these, the pouch type has been gaining more attention in EVs recently due to its higher capacity, design, flexibility, lightweight, compactness and capability to deliver high-load currents at any driving conditions (Fig. 1.1).

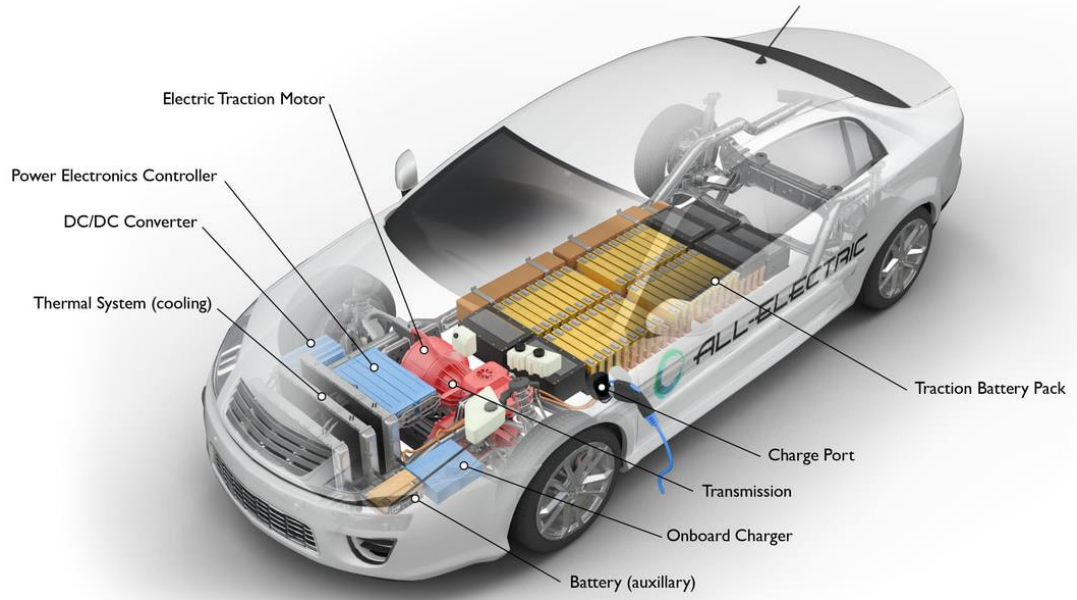
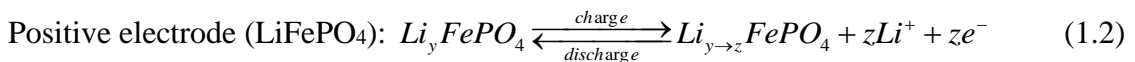
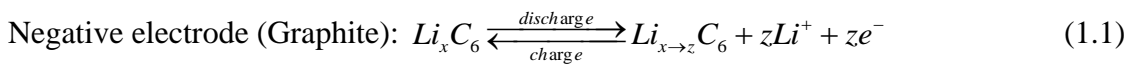


Fig. 1.1: Augmentation of a Li-ion battery pack and corresponding drive-train of an EV

### 1.1.1 Working Principle of Li-ion battery

The schematic representation of a  $\text{LiFePO}_4/\text{Graphite}$  pouch Li-ion battery mechanism is shown in Fig. 1.2. Here, a single local cell unit consists of carbonate-based electrolyte, a negative copper collector connected with the graphite electrode  $\text{Li}_x\text{C}_6$  mesocarbon microbeads (MCMB) as an anode and a positive aluminium current collector allied with the  $\text{LiFePO}_4$  (lithium iron phosphate) electrode as a cathode. Both the current collectors of the one-dimensional (1D) local cell are in parallel connection to constitute a single three-dimensional (3D) battery. The continuous electro-chemical reactions during battery charging and discharging processes allow the electrons to move through the load from cathode to anode and vice versa, while the positive ionic current passes over the electrolyte (separator) and is expressed as (Bahiraei *et al.* 2017):



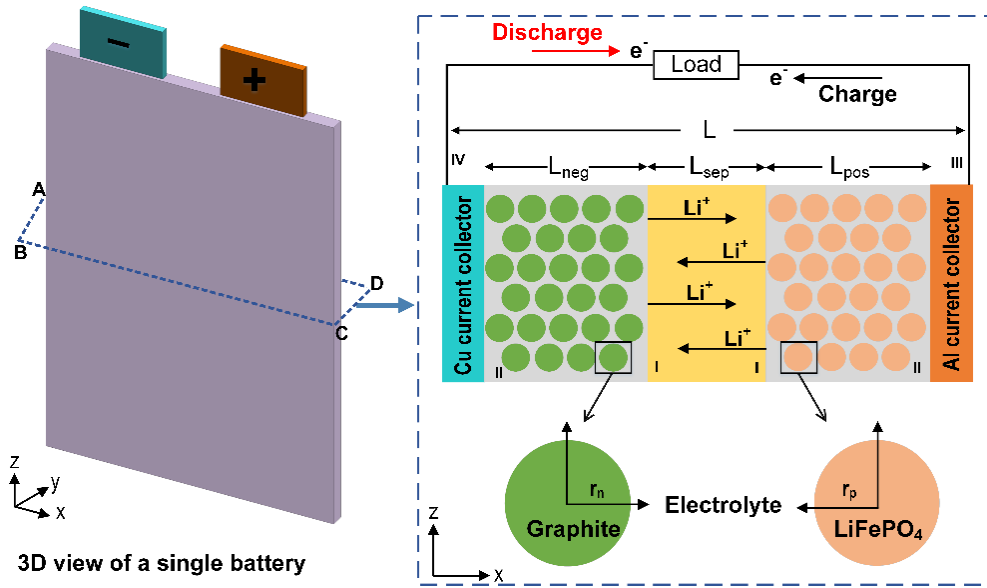


Fig. 1.2: Schematic representation of a single pouch-type LiFePO<sub>4</sub> battery cell and its cross-sectional view

## 1.2 Battery thermal management system

### 1.2.1 Thermal issues in Li-ion batteries

In an EV, hundreds of Li-ion batteries are combined to form a pack or module by arranging them in series or parallel combinations to alleviate the range anxiety. EV performance is highly dependent on the capacity of these batteries, and their core temperature has a significant role in achieving this. During on-road driving conditions at fast charging, Li-ion batteries undergo high heat generation issues, making them more vulnerable to working temperature (Yalcin *et al.* 2022). If the cell temperature in a pack is beyond 60 °C, it undergoes accelerated ageing, capacity degradation and uncontrollable heat generation, resulting in thermal runaway. At the same time, cell capacity is reduced if the temperature is below -20 °C due to increased internal resistance (Ma *et al.* 2018). However, the actual operating temperature is well below or above this range which may contribute to thermal runaway in summer, and cold start in winter. Moreover, temperature deviation within or

between the cells can seriously impact their health (Cho *et al.* 2012; Xie *et al.* 2022; Mevawalla *et al.* 2022). A higher temperature deviation leads to an electrical imbalance among the cells in a pack and reduces the overall performance. Usually, these batteries approach their end of life once there is a loss in capacity or growth in internal resistance by 20% and 30%, respectively. In the worst-case scenario, the EVs most expensive component (30%), the battery pack, may require total replacement before reaching to the claimed number of life cycles.

To date, many fire accidents have taken place due to mechanical, electrical and thermal failures in Li-ion batteries, as shown in Fig. 1.3. For instance, flames bursting out from the Porsche Panamera E-Hybrid while connected to a household charging plug-in in Thailand in March 2018 and the fire accident of Tesla Model S in Pittsburgh, February 2019. A few other significant incidents that occurred in automotive are listed in Table 1.1. Keeping aside the technical factors for collision or ineffective sealing, incidents due to battery overcharge or discharge, fault conditions, and extreme localized temperatures could be regulated through an efficient battery thermal management system (BTMS) (Lu *et al.* 2020). Although the cell replacement technique can boost the battery cycles, designing and implementing an efficient BTMS that improves EV energy competence and driving mileage while assuring battery safety and longevity is essential. As per the previous studies, a good BTMS should regulate the operating temperature of the pack within 25 °C to 40 °C while maintaining a temperature difference less than 5 °C among the cells to increase the lifespan and for effective performance (Bandhauer *et al.* 2011).

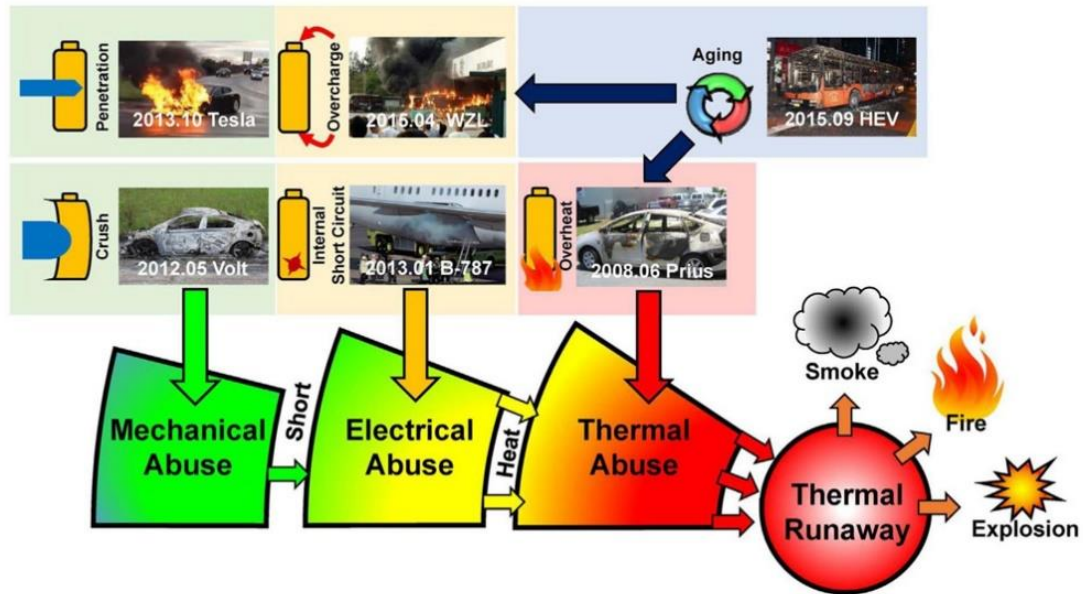
Fig. 1.3: Typical fire accidents (Feng *et al.* 2018)

Table 1.1: Li-ion battery fire incidents (information adapted from different internet websites)

Vehicle type	Place/Date	Incident summary
Tesla Model S EV	New Hampshire, 2022	Fire was caused in the battery pack as the vehicle lost control and hit a tree at high speed.
Rivian R1 S EV	Illinois, USA, 2021	Fire occurred at the manufacturing plant due to a high-voltage testing incident.
Tata Nexon EV	India, 2021	Electrical malfunction led to a short circuit
Chevrolet Bolt EV	Various locations in the US, 2020	Fire was caused due to manufacturing defects in the battery cells produced by LG Chem.
Hyundai Kona EV	Montreal, Canada, 2019	Fire started spontaneously when the car was parked in the garage, not plugged in for charging.
Audi e-Tron EV	Michigan, USA 2019	Caught fire when parked in a residential garage
Mitsubishi Outlander Plug-In HEV	Yokohama, Japan, 2013	One of the cells in a battery pack got overheated, melting the adjacent cells.
Zotye M300 EV	Hangzhou, China, 2012	Defect in the battery pack damaged the insulation between the battery cells and walls of the container, causing a short circuit.

## 1.2.2 Comparison of BTMS and challenges

In recent years, a considerable amount of research has been conducted to solve thermal issues of Li-ion batteries to develop this as a safe, reliable, and ecologically responsible power source. Based on the heat transfer media, the BTMS is broadly classified into three groups: active, passive and hybrid, the latter being a combination of the former two. Fig. 1.4 shows the schematic layout of various battery cooling approaches. An active cooling system usually involves acquiring energy from external sources such as a fan, blower or pump. Air (Fan *et al.* 2013), liquid (Qian *et al.* 2016) and thermoelectric cooling (Lyu *et al.* 2019) are the methods included in this category. In contrast, passive cooling systems can operate autonomously, require no external energy source, and exhibit reduced levels of NVH (noise, vibration, and harshness). Phase change materials (PCMs), heat spreaders and heat pipes are examples of this method.

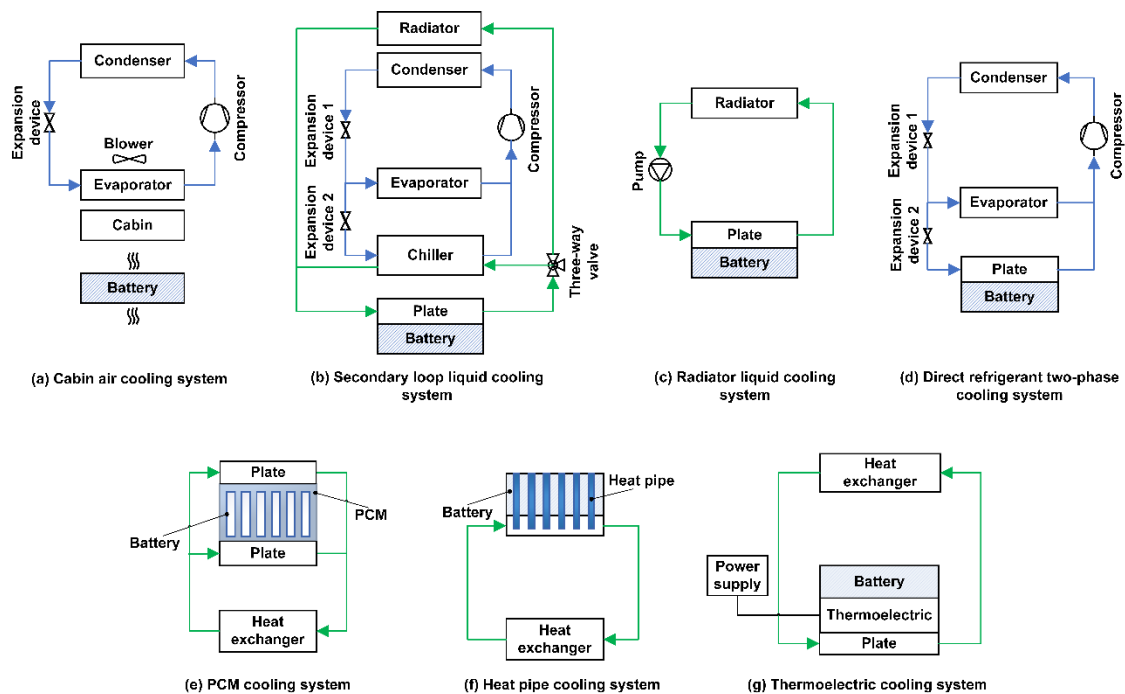


Fig. 1.4: Schematic of various battery cooling systems (Kim *et al.* 2019)

Table 1.2 summarises the literature on different cooling methods utilized for battery cooling. Although the simple air-cooling system requires less maintenance, it provides poor cooling effectiveness during high acceleration and uphill driving conditions. Moreover, an air-cooling system typically focuses on the arrangement of the battery cells depending on their type (cylindrical or prismatic) and the duct shape. This requires meticulous design in constructing the battery pack to augment the heat transfer. It is mainly employed in EVs such as Nissan Leaf, Volkswagen e-Golf and MG ZS with smaller cooling loads due to its lower heat transfer coefficient.

PCMs are the best storage methods due to their high latent heat capability. However, their usage is limited to a few energy applications due to their relatively low thermal conductivity, low heat transfer capacity and operating out of usable latent heat (Qu *et al.* 2019). Also, when using PCM, it's necessary to pay careful attention to ensuring the tightness of the battery pack, given the fluidic nature of PCM in its solid-liquid transition state. If not, the increased PCM density could make the battery pack unwieldy and hardly meet the lightweight design criteria. Heat pipe cooling (Rao *et al.* 2014) is another excellent technique to offer good temperature uniformity and efficient heat conduction. Yet, they are mainly used as a secondary unit in hybrid cooling systems since the passive method cannot handle the high heat generation rates alone in an EV. Comparatively, liquid cooling is prominent as an effective BTMS in EVs due to its exceptional advantages of thermal exchangeability, flexibility, and compact structure (De Vita *et al.* 2017; Wu *et al.* 2019). According to a US National Renewable Energy laboratory survey on BTMS, liquid cooling is an ideal choice for the EV market (Keyser *et al.* 2017). Table 1.3 provides the list of EVs employing liquid cooling.

Table 1.2: Summary of the available literature to design an energy-efficient BTMS

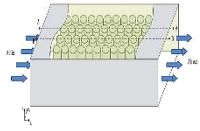
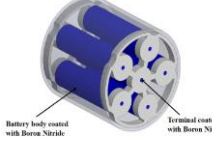

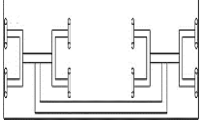
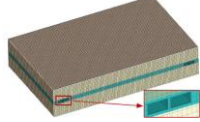
Reference	Battery type	No. of batteries	Cooling type	Figure	Nature of work	Variables	Observations and Remarks
Tong <i>et al.</i> (2016)	Prismatic	22	Air cooling		Simulation	air velocity, cell arrangement, cell-to-cell distance and a reversal airflow	<ul style="list-style-type: none"> <li>• Combination of 1D electro-thermal model with 2D conjugate heat transfer model</li> <li>• Reduction in the maximum temperature with an increase in air velocity or decrease in a cell-to-cell distance</li> </ul>
Saw <i>et al.</i> (2018)	Cylindrical	6	Dry/Mist air cooling		Experiment/ Simulation	Mass flow rate	<ul style="list-style-type: none"> <li>• Mist cooling gives better results compared to dry air cooling</li> <li>• Maximum battery temperature is below 40°C with a lower mist loading fraction at a particular flow rate and discharge rate</li> <li>• Power consumption is reduced and thermal performance is enhanced</li> </ul>
Li <i>et al.</i> (2014)	Prismatic	9	Copper foam-paraffin composite PCM		Experiment	foam porosity, pore density	<ul style="list-style-type: none"> <li>• Comparison between foam-paraffin composite PCM with pure PCM and air cooling</li> <li>• Air cooling overdone the maximum permissible temperature limit</li> <li>• A drastic reduction of the surface temperature with pure PCM</li> <li>• Further temperature reduction with better uniformity for composite PCM</li> </ul>
Xu <i>et al.</i> (2019)	Prismatic	15	Liquid cooling (T-shape)		Simulation	flow rate, coolant inlet temperature	<ul style="list-style-type: none"> <li>• Excellent temperature distribution and lower maximum temperature</li> <li>• Reduction in pressure drop with the simplified cold plate structure</li> </ul>
Sheng <i>et al.</i> (2019)	Prismatic	2	Liquid cooling (serpentine)		Experiment/ Simulation	channel design, flow rate, channel width, C-rate	<ul style="list-style-type: none"> <li>• Double inlets and outlets within the cooling plate</li> <li>• Reduction in the maximum cell temperature with an increase of mass flow rate</li> <li>• An enhanced power consumption and least impact on temperature variation with the increase of channel width</li> </ul>



Table 1.3: List of EVs with liquid cooling

<b>EV Model</b>	<b>Battery Capacity (kWh)</b>
Tesla Model S	Up to 100
Nissan Leaf	62 (Leaf e+)
Chevrolet Bolt EV	66
Audi e-Tron	71 (e-Tron 50) or 95 (e-Tron 55)
Jaguar I-PACE	90
Hyundai Kona Electric	39.2 (Standard) or 64 (Long Range)
Ford Mustang Mach-E	Up to 98.8
Porsche Taycan	Up to 93.4
Kia Soul EV	64
Tata Nexon EV	30.2
MG ZS EV	44.5

### 1.2.3 Liquid Cooling

Based on the fluid contact type, liquid cooling is mainly categorized into direct cooling (DC) and indirect cooling system (IDC). In the DC approach, batteries are immersed in a non-conductive liquid such as silicone oil, mineral oil, and deionized water. Although the DC cooling technique shows the potential for technically exceptional performance, it is still in the research phase and is not widely accepted by the automotive industries. The main impracticability of this method is that the battery pack submerged in the liquid must be leak proof, and the outer material on the battery should not corrode (Y. Deng *et al.* 2018), increasing the capital cost and maintenance of the BTMS. Most studies suggest that the IDC approach with a liquid cooling plate deployed on the battery surface effectively improves the heat transfer performance in BTMS. Coolants like water, thermal oil, glycol solution, refrigerant, etc., are allowed to pass through the cooling plate for better heat transfer performance. For instance, the Chevrolet Bolt EV uses a thin metallic structure cold plate and places them between two consecutive batteries of a T-shaped pouch battery pack (Qu *et al.* 2014). Whereas, Tesla designs a thin metal tube with a semi-circular flow channel, arranging it tightly on each cylindrical battery column's wall surface to cool a sizeable cylindrical battery pack (Berdichevsky *et al.* 2009). To date, a substantial amount

of research has been conducted on the profile of mini channel cold plates as it shows an immense effect on the efficacy of the overall cooling system. Henceforth, the thermal management of a pouch-type Li-ion battery module with IDC approach comprising a cold plate has become the point of attention for the present dissertation. The methods followed to attain efficient BTMS are discussed in the following sections.

## **1.3 Approach for BTMS**

The operating temperature of the Li-ion battery module and the variation of temperature between the individual batteries significantly impact the battery's functioning in terms of its life cycle, usable limit, and safety. Although there are several alternate choices, experimental and numerical investigations are the most predominant approaches. The following subsections provide an in-depth discussion of these methods.

### **1.3.1 Experimental investigation**

An experimental approach is critical in developing numerous battery models since it generates the data for construction and calibration. However, it has a few limitations. To begin with, since each experiment only investigates one condition, analysing the battery's diverse behaviour across various ambient or charge and discharge test conditions requires excessive time and can be arduous. In addition, utilizing surface temperature data as an indicator does not accurately represent the battery's maximum temperature, as there exists a discrepancy between the surface and core temperatures. Finally, using a real battery in the experiments has one of the significant disadvantages since it acts unpredictably in extreme operation conditions and may lead to thermal runaway.

Instead, most studies employ a cartridge heater and battery simulator to model the heat generation process on a large scale. Using a heater, the power supply can be varied to generate the required heat without any safety concerns with the help of a voltage regulator. (Lyu *et al.* 2019; Smith *et al.* 2018; Gou and Liu 2019; Chen *et al.* 2022), followed the analogous methodology. Besides this, there is limited research report available on the experimental investigation of IDC approach for a specific battery type. Keeping this in view, preliminary studies are conducted in the present dissertation with heating rods in an aluminium block (similar to the dimensions of a pouch battery) to examine the performance of a mini-channelled cooling plate under different operating conditions.

Numerical approaches, on the contrary, provide significantly greater flexibility, allowing the model parameters to be adjusted to any given scenario. Moreover, it enables the researchers to determine the thermal characteristics of every single component by a visual representation within the battery model. In addition, it limits the quantity of prototyping and experiments to be conducted, especially during the design phase. Therefore, researchers frequently rely on numerical methodologies despite a few real discrepancies. However, the first simulation stage requires developing a battery thermal model that explains the heat generation process, which is thoroughly discussed in the following subsection.

### **1.3.2 Numerical investigation**

To address the detrimental impact of temperature on the battery, it is imperative to understand the mechanisms causing heat generation and map out heat distribution within the battery (Al Hallaj *et al.* 2000). Real-time prediction of battery core temperature and terminal voltage is crucial in attaining effective solutions for BTMS. Therefore, a profound

understanding of a large-capacity battery's electro-chemical and thermal characteristics is required (Mistry *et al.* 2019). Researchers have made significant efforts over the last few decades to develop thermal models for Li-ion batteries. Broadly speaking, battery models are classified into three categories: (i) empirical equivalent circuit models (ECMs), (ii) Newman, Tiedemann, Gu, and Kim (NTGK) (Newman and Tiedemann 1993; Gu 1983; Kim *et al.* 2008), and (ii) physics-based. These models are further integrated into computational platforms such as ANSYS Fluent or COMSOL Multiphysics or STAR CCM+ for 2D or 3D thermal modelling of Li-ion cell/module/pack.

ECMs (Chang *et al.* 2020) offer a valuable understanding of cell behaviour by constructing equivalent circuits with the help of simple electrical components like capacitors, resistors and voltage sources. Thevenin and impedance-based are the most commonly used ECMs (Seaman *et al.* 2014). Although the ECMs are simple and robust, they do not consider the fundamental characteristics of the cell. The NTGK establishes a relation between the volumetric current transfer rate and the potential difference between the two electrodes (positive and negative). This relationship is defined by an empirical function with two polynomial parameters that vary with the depth of discharge and are derived through the fitting of experimental polarization curves. Even though this model is extensively adopted, one disadvantage is its reliance on empirical curve fitting, which may limit its accuracy and applicability in various battery types or operating conditions.

Electro-thermal (Vertiz *et al.* 2014), electro-chemical thermal (ECT) (Lai *et al.* 2015a) and thermal runaway (TR) (Feng *et al.* 2016) models fall under the category of physics-based models. As demonstrated by (Wei *et al.* 2014), the electro-thermal model can accurately represent heat generation and variations in voltage and current exhibited by the batteries.

In contrast, the ECT models employ different combinations of electro-chemical (single particle, equivalent circuit, pseudo-2D, pseudo-3D, etc.) and thermal (2D and 3D) models, solving them simultaneously. They consider various sources of heat generation, such as electro-chemical reactions, ohmic losses and active polarization. TR models are constructed based on energy equations and can be integrated with either electro-thermal or ECT models. In addition, there are simple and computationally efficient lumped parameter models (Lin *et al.* 2014), that cannot provide details of power/capacity loss of batteries under different operating conditions. For this, higher fidelity models like ECT are essential. Table 1.4 compares the available literature on different battery ECT models.

Based on the above literature and Table 1.4, the following observations are made:

- Despite their complexity and high computation cost, the researchers widely adopt ECT models as they can accurately predict the battery thermal behaviour, which plays a significant role in designing BTMS.
- However, most studies are limited to a single smaller capacity cell or battery thermal models that do not consider the underlying physical phenomena.
- Despite the substantial number of studies on the module/pack with IDC approach using ECT modelling, temperature inhomogeneity still exists, indicating the need to pursue further research in determining suitable strategies for temperature control of batteries.

Therefore, a fully coupled model, i.e. 1D electro-chemical model and 3D thermal model, is established in the present dissertation to solve the heat transfer associated with the cell as well as the temperature distribution of battery module with IDC method using a commercial software COMSOL Multiphysics 5.4.

Table 1.4: Summary of available literature on different battery ECT models

Author	Battery type	Study type	No. of batteries	Electro-chemical model	Thermal model	Cooling method	Observations
<i>Lt al.</i> (2015a)	10Ah Pouch	Experiment/Simulation	1	Pseudo-2D	3D	-	<ul style="list-style-type: none"> <li>Investigated the heat generation and thermal characteristics of battery under high discharge rates</li> <li>Good agreement between simulation and experimental results</li> <li>Heat generated by current collectors and separators show less effect on temperature rise</li> <li>Temperature exceeds 50 °C for a discharge rate of 5C</li> </ul>
Chiew <i>et al.</i> (2019)	2.5Ah Cylindrical	Experiment Simulation	1	Pseudo-2D	Lumped	-	<ul style="list-style-type: none"> <li>Validated model at different discharge rates and operating conditions</li> <li>Utilized regression models to measure thermal behaviour at various DOD for different discharge currents</li> </ul>
Jiang <i>et al.</i> (2020)	50Ah Prismatic	Simulation	1	1D	3D	Forced air	<ul style="list-style-type: none"> <li>Explored the effect of varying heat transfer coefficient on different battery surfaces</li> <li>Investigated the impact of operating temperature on battery capacity fading</li> </ul>
Suresh Patil <i>et al.</i> (2021)	20Ah Pouch	Experiment/Simulation	14	NTGK	3D	Dielectric-Single phase	<ul style="list-style-type: none"> <li>Maximum temperature maintained &lt; 40°C for 3C discharge rate</li> <li>Dielectric cooling proved to be effective than IDC. Effects of boiling are not considered</li> <li>Thermal runaway prevention applies for the pack, except for the affected cell under abusive conditions</li> </ul>
Li <i>et al.</i> (2019)	20Ah Prismatic	Simulation	14	ECM	3D	Liquid-Mini channel cold plate	<ul style="list-style-type: none"> <li>Conducted simulations under fast discharge and abuse conditions</li> <li>Careful design of coolant flow rate could maintain the temperature within the safe limits and prevent hot spots</li> </ul>
Bahiraei <i>et al.</i> (2017)	4Ah Pouch	Simulation	6	1D	3D	Liquid-Single pass/Dual pass inlet	<ul style="list-style-type: none"> <li>Two IDC approaches are evaluated under FUDC driving cycle</li> <li>Cooling plate thickness and Reynolds number showed a significant impact on temperature reduction and uniformity</li> </ul>
Siruvuri and Budarapu (2020)	1.5Ah Prismatic	Simulation	5	1D	3D	Liquid-Serpentine channel	<ul style="list-style-type: none"> <li>Liquid coolant effectively maintains peak temperature</li> <li>Recommended flow reversal for efficient heat transfer</li> </ul>

## 1.4 Comparison of different cooling channel designs

In designing a liquid cooling system, several sizing and rating parameters such as size, expense, weight, contact resistance between plate and battery, variation in temperature between the batteries, leakage, overall module efficiency, and pumping power are to be considered (Wu *et al.* 2019). Different mini or microchannel cold plates (Naquiuddin *et al.* 2018) are generally sandwiched between two consecutive batteries or placed at the sides or bottom of the battery module. The cold plate technology is anticipated to offer structural reinforcement for cells and seamlessly integrate into the battery cabinet to address safety concerns and optimize space utilization in EVs.

Based on the literature, it is understood that the most explored cold plate designs for BTMS are serpentine, straight, and U-bend. Due to the restriction of size and volume in the cooling system, the augmenting path would be to focus on modifying the channel configuration for better heat transfer capability. Given this, several modifications have been made to the internal structure of channels to attain efficient cooling of Li-ion batteries. Oblique fins are designed across a straight-channelled cold plate, enabling improved heat transfer competence and uniformity compared to a straight fin design (Jin *et al.* 2014). Streamlined shapes are introduced as a replacement for straight channels, lowering the frictional resistance (Huang *et al.* 2019). Besides this, the recent design improvements include the use of wedge-shape (Rao and Xuan Zhang 2019), dendritic (Fan *et al.* 2021), leaf type (Deng, Ran, Zhang and Yin 2019), tree type (Liu *et al.* 2019), grooved channels (Rhodes and Thompson 2020), etc.

Table 1.5: Summary of available literature on MOO applied to IDC approach

Author	Channel type	Design cases		Variables	Surrogate model	Optimization technique	Objectives		
		No.	Method				Output 1	Output 2	Output 3
Deng <i>et al.</i> (2020)	Bifurcation	35	LHS	$D_1$ (mm), $\omega$ , $\gamma$ , $d_c$ (mm), $q_m$ (g s <sup>-1</sup> )	RSM	NSGA II	$h = 0.329$ W °C <sup>-1</sup>	$f = 2283.17$ m <sup>2</sup>	-
Deng <i>et al.</i> (2019)	Bifurcation	40	LHS	$\alpha$ , $\beta_1$ , $\beta_2$ , $d_c$ (mm)	RSM	Weight distribution method	$T_{max} = 38.39$ °C	$T_{\sigma} = 1.93$ °C	$\Delta P = 2121$
E. Jiaqiang <i>et al.</i> (2018)	Straight	16	Orthogonal	$L$ (mm), $H$ (mm), $V$ (m s <sup>-1</sup> ), $M$	Orthogonal analysis	Weight distribution method	$T_{avg} = 37.28$ °C	$\Delta T = 7.91$ °C	-
Dong <i>et al.</i> (2021)	Double helix structure	15	LHS	$P$ (mm), $D$ (mm), $M$ (kg s <sup>-1</sup> )	Kriging	NSGA II	$T_{max} = 32.41$ °C	$\Delta T = 6.98$ °C	$\Delta P = 47.2$ Pa
Suman <i>et al.</i> (2021)	U-shaped	200	LHS	$t_1$ (mm), $t_2$ (mm), $T_c$ (°C), $v$ (m s <sup>-1</sup> )	Genetic Programming	Genetic Programming search	TD = 7.69 °C	TSD = 2.54 °C	PD = 436.43 Pa
Xu <i>et al.</i> (2021)	Serpentine	36	MRS	$m_1$ (mm), $m_2$ (mm), $T$ (°C), $v$ (m s <sup>-1</sup> )	Kriging- RBF	PSO	MTD = 3.74 °C	$T_{max} = 28.45$ °C	-
Fan <i>et al.</i> (2021)	Double layered dendrite	80	LHS	$m$ , $\alpha_m$ , $\beta_v$ , $\gamma$	RBF	NSGA-II	$T_{max} = 40.5$ °C	$\Delta T = 1.9$ °C	$\Delta P = 138.06$ Pa
Tang <i>et al.</i> (2021)	-	150	-	$V_{comp}$ , $T_o$ , $V_{air}$	SVR-RBF	PSO	COP = 2.36	$C_{cool} = 5.12$	-
Wu <i>et al.</i> (2020)	Straight	25	CCD	$x_1$ , $x_2$ , $x_3$ , $x_4$ (mm)	RSM	Two-step method	$T_{max} = 46.52$ °C	$\Delta T = 4.28$ °C	Sqrt ( $\Delta P$ ) = 63.40 Pa
Li <i>et al.</i> (2021)	U-shaped	100	LHS	$t_1$ (mm), $t_2$ (mm), $T$ (°C), $v$ (m s <sup>-1</sup> )	RSM/RBF/GP	NSGA-II	TD = 3.93 °C	TSD = 1.43 °C	PD = 327.11 Pa
Wang <i>et al.</i> (2021)	Serpentine	150	LHS	$b$ (mm), $a$ (mm), $c$ (mm), $l$ (mm), $e$ (mm), $v$ (m s <sup>-1</sup> )	Kriging/RSM/ RBF	MOGA	$T_{max} = 35.45$ °C	$P_{max} = 502.05$ Pa	$T_{avg} = 32.85$ °C



Considering the aforementioned research works, the following observations are made:

- Most of the literature focuses on improving the existing channel layout, modifying the design features, or incorporating fins. However, none have made a conclusive decision by comparing several designs under same conditions.
- A holistic channel design which can offer energy-efficient cooling of a particular power battery is rarely addressed in the literature.

Keeping this in view, the present dissertation compares six different channel designs while maintaining a constant flow volume, focussing on a 20Ah pouch battery module for a higher discharge current.

## **1.5 Optimization through surrogate models and NSGA II**

Based on the works mentioned above, it is understandable that several factors influence the performance of BTMS. Moreover, the relation between input (design/operating) variables and response parameters (maximum temperature, temperature deviation and pressure drop) is rather complex. Therefore, a single-factor analysis is conducted by most of the previous studies to investigate the thermal behaviour of the cell/module/pack. However, an optimized channel design that could keep the battery's maximum temperature and temperature deviation within safe limits, and minimize energy consumption is more beneficial in real-world applications. Balancing all these functions is critical in achieving cost-effectiveness and optimal thermal performance. Thus, a multi-objective optimization (MOO) is to be performed to compromise this conflict.

To date, considerable research has been carried out on the MOO of indirect liquid cooling approach in which different geometric parameters of the cooling plate and the structure of the battery pack are optimized using different optimization techniques (Table 1.4). Besides this, in the domain of BTMS, direct optimization using high-fidelity Computational Fluid Dynamics (CFD) models and experiments is notably time-consuming. Therefore, surrogate models, a widespread technique in machine learning (ML), have been employed to represent essential objectives as functions of the input variables.

A typical optimization workflow combines ML models with multi-objective genetic algorithms (MOGA). Initially, the factors influencing the coolant plate and the response parameters to be minimized or maximized are to be defined. This includes the structural parameters, operating parameters such as mass flow rate and coolant temperature, and dimensionless parameters. Based on this, a design space is to be generated with the help of design of experiment (DOE) techniques such as Latin hypercube sampling (LHS), central composite design (CCD), box-benken design (BBD), orthogonal sampling and etc. Either simulation or experimental findings are then used to calculate the response parameters.

Since experimentation is expensive and consumes a lot of time and resources, most researchers are directed towards simulations. Later, a surrogate model is used to build the relation between input variables and response parameters. These models can predict accurately by appropriately providing the train and test data ratio. The most popular surrogate models include Kriging/Gaussian process regression (GPR) and response surface method (RSM). RSM (Myers *et al.* 2018) is a method of fitting polynomial functions to discrete responses based on numerical results. In general, a second-order polynomial function is employed as the response function. In comparison, Kriging is a spatial

correlation technique that often predicts value based on sampled data. Apart from these, Support vector machine (SVM), Radial basis function (RBF), Artificial neural networks (ANN), and Ensemble methods are also utilized. Adequate data support is required for accurate estimation of these models, which mainly relies on sample size, choice of algorithm, and the range of prediction.

Once the best surrogate model is determined, the MOO is performed either with constraints or without constraints for the different range of input variables. To date, different MOGA methods are employed, such as Non-dominated sorting genetic algorithm (NSGA-II), particle swarm optimization (PSO), artificial bee colony (ABC), cuckoo search, simulated annealing (SA) and etc. Among these, NSGA II is one of the most potent algorithms due to its ease of tuning, diverse non-dominated solutions and robustness. Finally, the non-inferior set of solutions (i.e. Pareto optimal solutions) are obtained. Further, the best compromise solutions from the Pareto front are attained using techniques like K-means clustering, weight distribution method, multi-criteria decision-making methods (MCDM), etc.

Table 1.5 summarizes the available literature on MOO methods applied to the indirect liquid cooling approach. The critical observations are as follows:

- Despite the considerable progress, most of the literature often utilized simple surrogate models like RSM and orthogonal analysis, potentially failing to capture the intricate relationship between input variables and response parameters.
- Researchers have rarely considered the combination of structural factors and operating parameters, evaluating their effect on the thermal behaviour of battery modules/packs.

- In the existing literature, using the SHapley Additive exPlanations (SHAP) technique for the surrogate model in BTMS remains unexplored, limiting our understanding of how individual features impact the model's predictions.

Based on the above observations, the present work applies optimization techniques to one of the best designs obtained from comparing the six designs. Alongside, SHAP technique is utilized to visualize the behaviour of prediction model.

## 1.6 Introducing novel Tesla design

Although traditional cooling designs are extensively researched, novel technologies to control temperature and enhance battery safety are gaining wide popularity. Based on Nikola Tesla's ideas, the Tesla valve concept has become prominent in microfluidics, micro-pumps, micro-electronics, fuel cells, and heat pipe systems (Bardell and Microsciences 2017; Wahidi *et al.* 2020). A standard Tesla valve acts as a fluidic diode, allowing the fluid to flow forward and reverse, inflicting a direction-dependent pressure drop. However, the current Tesla valve literature focuses on fluid dynamics and flow control; as such, there is a limited exploration of its potential in BTMS.

Hence, the present dissertation aims to better understand the Tesla valve's functioning as a cooling plate design for the BTMS application by varying design variables. As a result, the present study attempts to close the existing gap in the literature by extending the scope of cooling strategies. Concurrently, this helps bridge futuristic possibilities in the field with the current knowledge, contributing to the disclosure of novel cooling methods.

## 1.7 Research gaps

Based on the above discussions on the literature available, the major research gaps identified are as follows:

- Limited research is conducted on the experimental investigation of pouch batteries with indirect liquid cooling approach comprising cold plates and corresponding heat transfer analysis.
- Despite the widespread studies on indirect liquid cooling, there is not much insightful information available in literature on how the profile of various channel designs under a constant volume would impact the cooling effectiveness or evaluating them against each other for a given battery type in cooling purposes.
- Researchers often utilized simple surrogate models and have rarely considered the effect of both design variables and operating parameters on the performance of cold plate.
- The potential of a Tesla valve which is widely popular in micro-fluidic applications is unexplored as a cold plate design for cooling the pouch batteries in the literature.

## 1.8 Objectives of the thesis

The following objectives have been formulated in the present dissertation to address the above-mentioned research gaps:

- Develop an experimental facility to emulate battery heating with heaters integrated into aluminium blocks and assess the performance of the indirect liquid cooling approach using a mini-channelled cooling plate.

- Comparative assessment among several cold plates with channel designs under constant volume for cooling of pouch-type Li-ion battery module.
- Optimizing the sizing/rating parameters of the best channel design obtained from the previous objective utilizing surrogate models and NSGA-II.
- Introduce a novel multi-stage Tesla valve (MSTV) towards the cold plate design for cooling the pouch batteries and investigate the effect of corresponding design parameters.

## 1.9 Organization of the thesis

The thesis comprises six chapters, the contents of which are described below:

### **Chapter 1: Introduction and literature review**

This chapter initiates the study by providing an extensive literature review, elucidating the research goals and the organization of the thesis.

### **Chapter 2: Develop an experimental test facility**

Establish an experimental set up to emulate battery heating using heaters. This facility is employed to evaluate the performance of an indirect liquid cooling approach comprising a cold plate with water as coolant for varying operating conditions such as coolant temperature, flow rate and flow direction. In addition, a pulse test with varying heating loads is also utilized.

### **Chapter 3: Comparison of different channel designs**

Conducts a comparative analysis of six distinct channel designs such as straight, serpentine, U-bend, pumpkin, spiral and hexagonal, with a constant volume to cool the pouch battery module using COMSOL Multiphysics

software considering several performance factors for a higher discharge rate. Alongside, the performance of channel designs is evaluated for varying ambient temperature. Finally, one of the optimal channel designs attained is tested under a realistic drive cycle condition.

#### **Chapter 4: Optimization through surrogate models and NSGA-II**

The superior cooling channel design identified in Chapter 3 is optimized through surrogate models and NSGA-II. The K-means clustering algorithm determines the best compromise solutions. Alongside, the SHAP technique is utilised to understand the best prediction model's behaviour by visualizing it.

#### **Chapter 5: Introducing a novel channel design**

Explores the influence of different design variables of a MSTV design embedded in a cold plate numerically using COMSOL Multiphysics software. This investigation helps in assessing the performance of MSTV as a cold plate in battery cooling applications.

#### **Chapter 6: Conclusions**

This chapter summarizes the research findings and presents insightful conclusions and recommendations for future work.

Also, an appendix reporting the sample points generated by LHS of Chapter 4.

# Chapter 2

## Explore the Efficacy of Indirect Liquid Cooling Approach with Mini Channel Cold Plates for Pouch Cells

### Keywords

Li-ion battery;  
Mini-channel;  
Liquid cooling;  
Thermal  
management;  
Heat transfer

*A battery simulator integrated with an ingeniously designed mini-channelled liquid cold plate is developed, and its thermal performance is experimentally evaluated. Different factors, such as coolant temperature, flow rate, and flow direction, are varied to keep the temperature of batteries within a safe range. A detailed thermodynamic analysis is conducted to evaluate the heat transfer performance of the proposed cold plate.*

## 2.1 Introduction

An energy-efficient thermal control system for maintaining temperature homogeneity among the batteries in a module or pack is required, as safety is of supreme importance while using Li-ion batteries in automobiles. Based on the previous studies (Table 1.2), an indirect liquid cooling approach comprising a cold plate effectively maintains the temperature of batteries in a safe range. To date, different micro or mini-channel cold plates (Naquiuddin *et al.* 2018) and fin plates (Chen *et al.* 2016) have been utilized to enhance the thermal performance of batteries.

Although the indirect liquid cooling approach is extensively studied through numerical methods (Table 1.2 and 1.5), thermal inhomogeneity remains, implying the need to conduct more research in determining suitable strategies for temperature control of pouch-type Li-ion battery modules. Hence, exploring a cold plate with simpler geometry for minimum pressure drop and battery module temperature within 25 to 40 °C is essential. The primary



role of a cold plate is to control undesirable temperature distribution across the module when operating under higher currents and temperatures. Moreover, limited experimental investigations are available to analyze the thermal performance of pouch battery modules integrated with cold plates for various operating conditions (Lyu *et al.* 2019; Smith *et al.* 2018; Gou and Liu 2019; Chen *et al.* 2022). Additionally, a detailed understanding of fluid flow and heat transfer characteristics is essential in effectively designing cold plates.

With the aforementioned motivation, a comprehensive research activity that involves the utilization of a pouch battery simulator in conjunction with a straight/parallel mini-channelled liquid cold plate is planned. In contrast to the conventional cold plate designs, the idea to put forward exhibit's simplicity, lesser weight, lower fabrication costs and flexible arrangement. The effect of different operating parameters such as coolant temperature, flow rate, and flow direction are explored to evaluate effectiveness of cold plate using the rating parameters such as average temperature, overall heat transfer coefficient, pressure drop, pumping power and cooling performance factor. Besides this, the local Nusselt number, local heat transfer coefficient,  $j/f$  factor and pressure drop are computed for a single aluminium flat tube of the cold plate using appropriate correlations for varying flow rates. In addition, a self-designed pulse load test with a duration of 5 hours is utilized to evaluate the performance of the cold plate.

## **2.2 Experimental test facility**

### **2.2.1 System description**

The schematic layout of the experimental set-up is shown in Fig.'s 2.1 and 2.2. The test bench includes a test section comprising aluminium block integrated with two cartridge

heaters mimicking the battery and a cold plate embedded with mini channels, a voltage regulator (Variac), heating/cooling circulator, peristaltic pump, differential pressure transmitter (DPT) to monitor pressure drop, an environmental chamber with temperature and relative humidity (RH) regulator and a data acquisition system (DAQ).

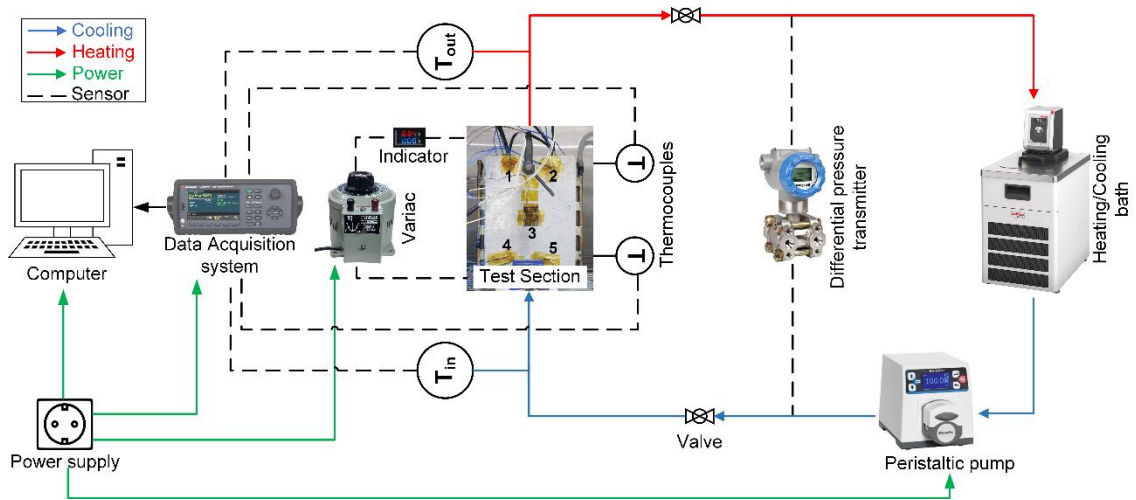


Fig. 2.1: Schematic layout of the experimental test set-up

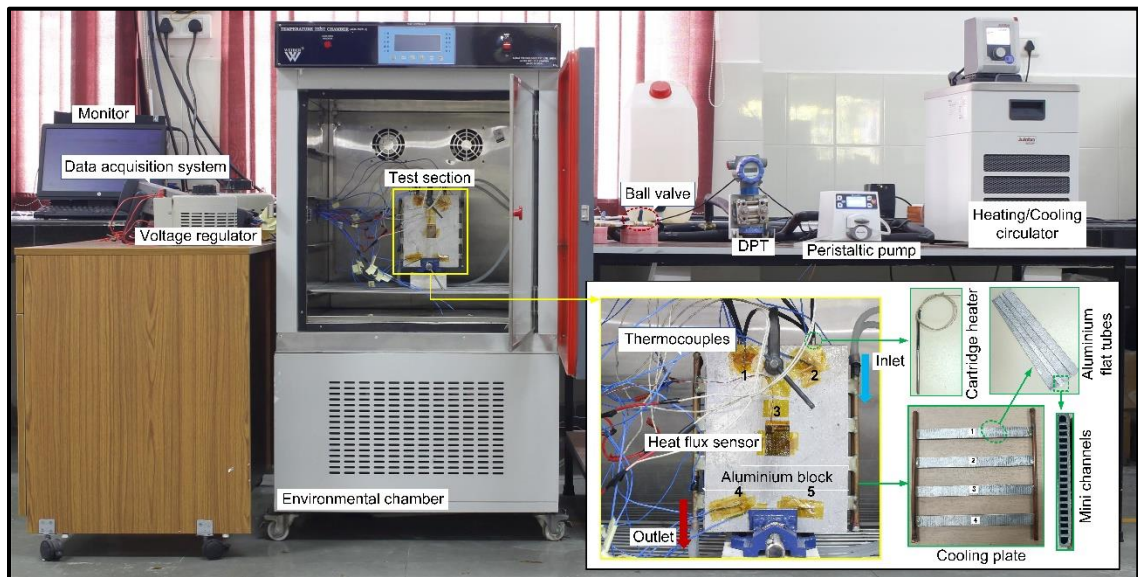


Fig. 2.2: Pictorial view of the test facility

A cold plate is fabricated with 4 aluminium flat tubes comprising 19 number of mini channels connected with a single header at both the terminals. Such type of cold plates are

sandwiched between two consecutive aluminium blocks. The test section comprises 3 aluminium blocks and 2 cold plates. A detailed view of the test section is shown in Fig. 2.3. The outer dimensions (length and width) of the aluminium block  $160 \times 227 \times 10$  mm is maintained same as that of the 20Ah and 3.3 V LiFePO<sub>4</sub>/Graphite pouch battery, i.e.  $160 \times 227 \times 7.25$  mm. The details of the pouch cell are provided in Section 1.1.1. The size of a single aluminium flat tube is  $180(L) \times 15(W) \times 2(t)$  mm, while the dimension of each mini channel is  $180(L) \times 0.52(w1) \times 0.91(t1)$  mm. The detailed dimensions of mini channel measured with the help of a vision measuring machine (VMM) are reported in Fig. 2.4 and Table 2.1.

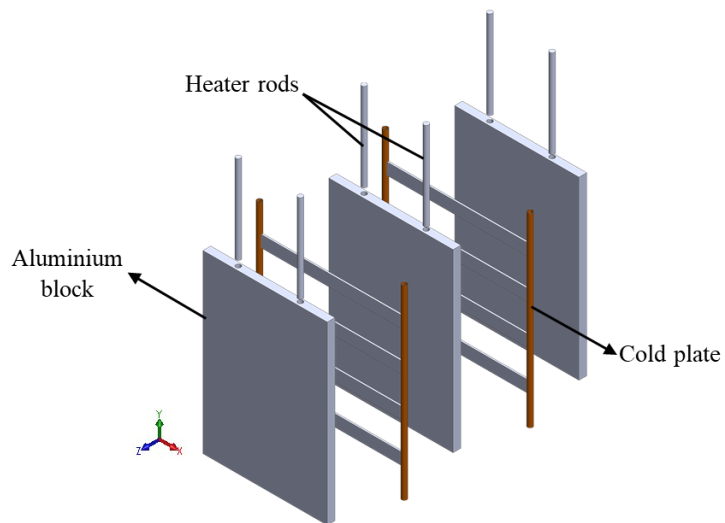


Fig. 2.3: Exploded view of the test section

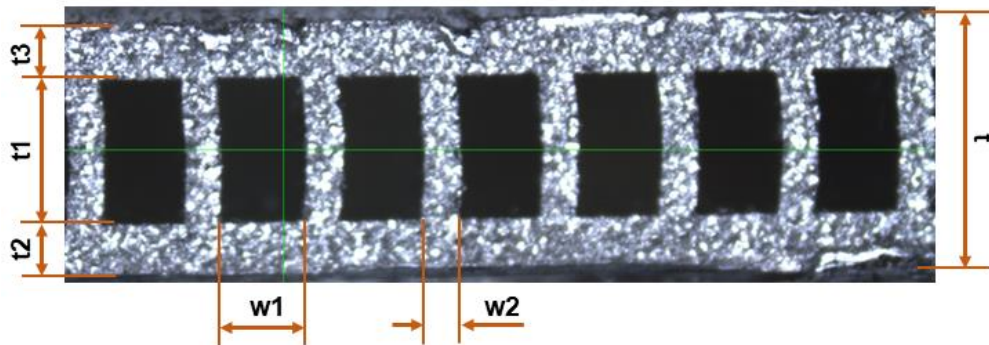


Fig. 2.4: Dimensions of mini-channel captured using VMM

Table 2.1: Cold plate dimensions

Parameter	$t$	$w1$	$w2$	$t1$	$t2$	$t3$
Value (mm)	2	0.52	0.22	0.91	0.545	0.545

The heat input to the blocks is supplied using two cartridge heaters connected in series, powered by a voltage regulator ranging from 0-240V and 0-8A. Each heater has a length of 80 mm and a diameter of 6.35 mm. Two 6.5 mm diameter holes are drilled on the top of the block to house the heaters. The selection of heater type and its position in the block are mainly based on the real battery thermal characteristics. Thermal grease is applied between the aluminium block and cooling plate to reduce contact resistance. The distilled water from the cooling bath passes through the fluid loop using a peristaltic pump to the cooling channels at a required flow rate. The coolant temperature at the inlet and outlet of the cold plate is measured by two T-type thermocouples. Five thermocouples are placed at different locations of the aluminium block to measure the surface temperature (Fig 2.2).

Among these, two thermocouples are in the top region of the block, one is at the centre and the other two are at the bottom region. A Kapton tape is used to attach the thermocouple to the block surface. Besides this, a heat flux sensor (Omega Engineering, Inc., USA) is placed at the centre of the block to measure the heat generation rate. To maintain the temperature, the single-phase coolant exiting cold plates is passed through an external heating/cooling circulator bath of Julabo 600F. The DAQ from Keysight 970A is used to collect the data from thermocouples.

## 2.2.2 Uncertainty analysis

The uncertainties associated with the performance parameters obtained from the sensors are estimated using the principle of propagation of error as suggested by Moffat (1988) and are represented as follows:

$$\delta U = \sqrt{\sum_{i=1}^n \left( \frac{\partial U}{\partial X_i} \delta X_i \right)^2} \quad (2.1)$$

where,  $U = U(X_1, X_2, X_3, \dots, X_n)$   $X_i$  and  $\delta X_i$  are the individual measurement and associated error, respectively.

Table 2.2: Specifications and accuracy of the instruments used in the present work

Instruments	Type	Location	Range	Accuracy
Heating/cooling circulator	Julabo 600F	-	-35 °C to 150 °C	±0.01 °C
Flow rate	Peristaltic pump (Master flex)	-	0 to 350 mL min <sup>-1</sup>	±0.5%
Pressure drop	Differential pressure transmitter (Honey well)	Between coolant inlet and outlet pipeline	0 to 4 kPa	Up to 0.025%
Heat supply	Cartridge heaters	Top of the aluminium block	175W, 230V	±0.5 W
Environmental chamber	Heating-cooling and humidity control	-	T: -5 °C to 70 °C; RH: 40% to 85%	T: ±2 °C; RH: ±5%
Temperature (°C)	T- type thermocouples	Across aluminium block	-250 °C to 350 °C	±0.5 °C or ±0.4%
Heat flux (kW/m <sup>2</sup> )	Differential-Temperature thermopile (Omega Engineering, Inc, USA)	Battery central region	T: -50 °C to 120 °C; q: ±150 kW/m <sup>2</sup>	5%

The details of the components used in the experimental test set-up are provided in Table 2.2. A leak test is carried out before the test set-up is assembled to ensure no fluid loss. The heat lost to the ambient is estimated to be less than 1% of the total heat input. Therefore, the heat losses are assumed to be negligible. T-type thermocouples are calibrated at different temperatures by placing them in a cooling bath with a standard resistance temperature detector (RTD) sensor. The observed temperature discrepancy between the measured and actual values is at ±0.5 °C. Additionally, the repeatability of results is monitored frequently for each varying parameter.

### 2.2.3 Experimental strategy

Four operating parameters are varied, including heat supplied to the blocks, coolant temperature, flow rate and flow direction. Initially, the test module is preheated till it reaches an average temperature of 60 °C. Cooling is initiated once the desired condition is achieved, and experiments are conducted for varying operating parameters. Three different schemes of experiments are planned. Firstly, five different values of coolant temperature ranging from 15 °C to 35 °C are selected with a 5 °C difference while keeping the coolant flow rate constant. At each condition, cyclic tests (three times) are performed. Considering the results, the next set of experiments are executed for a flow rate ranging from 150 to 350 mL min<sup>-1</sup> with corresponding Reynolds number,  $Re$  of 449 to 1047.85, to explore their significance on the cooling efficiency of the test module at a specific coolant temperature. Lastly, the coolant flow direction is varied for an optimal coolant temperature and flow rate obtained from the above test results. In addition, the performance of the mini-channelled cold plate is evaluated for a unique pulse load test designed with varying heat supply for 5 hours.

## 2.3 Data reduction

The Reynolds number,  $Re$ , is calculated as a function of flow rate (mL min<sup>-1</sup>),  $\dot{V}$  and dynamic viscosity (Pa. s),  $\mu$ . For a  $\dot{V} = 350$  mL min<sup>-1</sup>, the maximum achievable  $Re$  is 1047.85, signifying a laminar flow.

$$Re = \dot{V}_w D_h / \mu \quad (2.2)$$

where,  $D_h = 4A_{cs}/P$ ;  $A_{cs}$  ( $m^2$ ) and  $P$  (m) are the cross-sectional area and perimeter of the channel, respectively.  $\mu$  represents the dynamic viscosity of a fluid (Pa s).

The average heat transfer coefficient ( $W.m^{-2}. ^\circ C^{-1}$ ) of the proposed cold plate as a function of the cooling capacity ( $W$ ) is estimated as:

$$\dot{Q}_w = \dot{m}_w c_{p,w} (T_{w,out} - T_{w,in}) \quad (2.3)$$

$$h_w = \frac{\dot{Q}_w}{A_s [T_b - (T_{w,out} + T_{w,in})/2]} \quad (2.4)$$

The pumping power ( $P_{pump}$ ) required to circulate coolant through the mini-channelled cold plate is estimated in Watt as

$$P_{pump} = \Delta P \cdot \dot{V}_w \quad (2.5)$$

here,  $\Delta P$  represents the measured pressure drop value.

A cooling performance factor,  $\beta$ , is estimated as the ratio of cooling capacity and the required pumping power (Xun *et al.* 2013). A high  $\beta$  value agrees with additional active cooling and suggests greater energy efficacy.

$$\text{here, } \beta = \frac{\dot{Q}_w (W)}{P_{pump} (W)} \quad (2.6)$$

## 2.4 Results and discussions

The following subsection provides an in-depth evaluation of experiments conducted to identify the parameters influencing the efficacy of mini-channelled cold plates. Each subsection describes the experimental test procedure, followed by a comprehensive analysis of the results.

### 2.4.1 Effect of varying heat load

Before analyzing the effect of functioning parameters, experiments are conducted for varying heat loads to observe the maximum temperature reached by the test module for a continuous operation of 5 hours without any active cooling. A series of experiments are conducted by varying the voltage supply to the test module from 10V to 40V with a difference of 5V. The system reached steady state as the difference in time-averaged temperature between thermocouples is less than 0.5 °C.

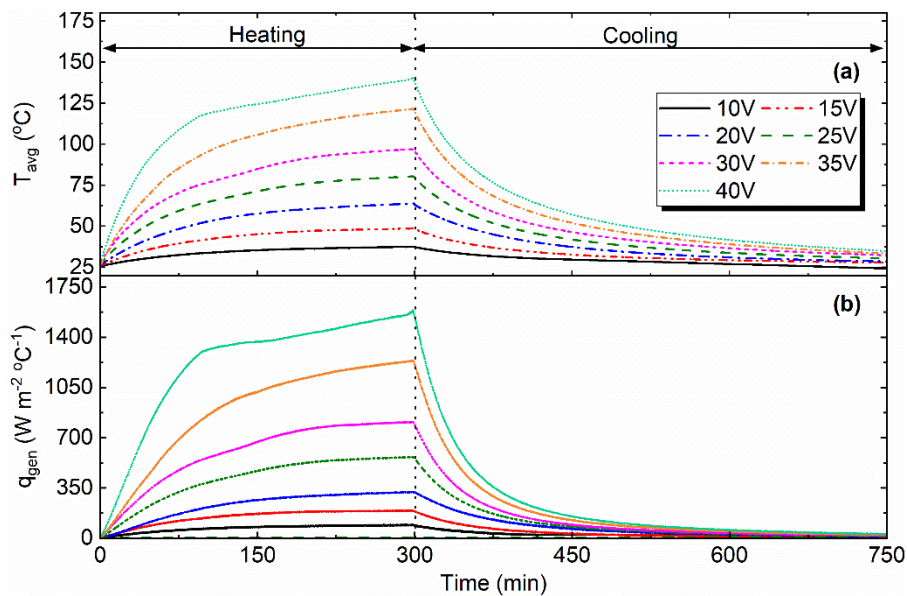


Fig. 2.5: Variation of temperature across the test module for varying heat load

Fig. 2.5 compares temperature and heat generation profiles across the test module for varying heat loads. It can be inferred that the temperature and heat generation rose fast in the first 90 min and then gradually remained steady by the end of heating. However, the module temperature with the increase of voltage supply gradually increases. Higher the voltage, higher is the temperature attained. For instance, the average temperature,  $T_{avg}$  and  $q_{gen}$  of the test module reaches a maximum of 137.7 °C and 1541.7 W m<sup>-2</sup> °C<sup>-1</sup>, as the



voltage is increased from 10V to 40V. For a lower voltage of 10V and 15V, the  $T_{avg}$  reaches to 37.33 °C and 48.24 °C while  $q_{gen}$  is 87.35 W m<sup>-2</sup> °C<sup>-1</sup> and 186 W m<sup>-2</sup> °C<sup>-1</sup>. The temperature reaches a greater extent, i.e. beyond 60 °C, as the voltage exceeds 20V. Considering the first 30 min of heating as set point, it can be seen that module temperature is in the range of 55 °C to 60 °C with a voltage of 35V. Hence, it can be asserted that an increase in voltage invariably results in a rapid fluctuation in temperature and an elevated module temperature. Therefore, 35V is identified as the maximum voltage supply to each block and is chosen for further experiments. Once the set point temperature, i.e., 60 °C is attained, cooling is initiated, and the system is allowed to attain the steady state.

## 2.4.2 Effect of varying coolant temperature

The coolant temperature considerably influences the temperature uniformity and heat transfer performance across the module. Hence, to explore the effectiveness of mini channelled cold plate at a temperature varying from the ambient conditions, the coolant temperature,  $T_{w,in}$  is altered from 15 °C to 35 °C with an increment of 5 °C for a flow rate fixed at 300 mL min<sup>-1</sup>, as exhibited in Fig. 2.6.

As the coolant temperature increases from 15 °C to 35 °C,  $T_{avg}$  increases by 19.92°C. The difference in temperature between cycles 1 to 3 is observed to be within 0.2 °C to 0.5 °C for all the cases. With water inlet temperature lower than the ambient temperature, like 15 °C and 20 °C, for cycle 1, the module  $T_{avg}$  reaches 13.80 °C and 25.58 °C, respectively. Whereas, for  $T_{w,in}$  of 30 °C, the  $T_{avg}$  of module reaches to 34.94 °C. For a  $T_{w,in}$  of 35 °C, the  $T_{avg}$  of the test module lies slightly beyond the desired working temperature range of

batteries (25 °C–40 °C) for a certain period. Lower the  $T_{w,in}$  is, quicker the  $T_{avg}$  achieves a stable value. Thus, it is established that the water temperature is directly proportional to the average surface temperature of the test module.

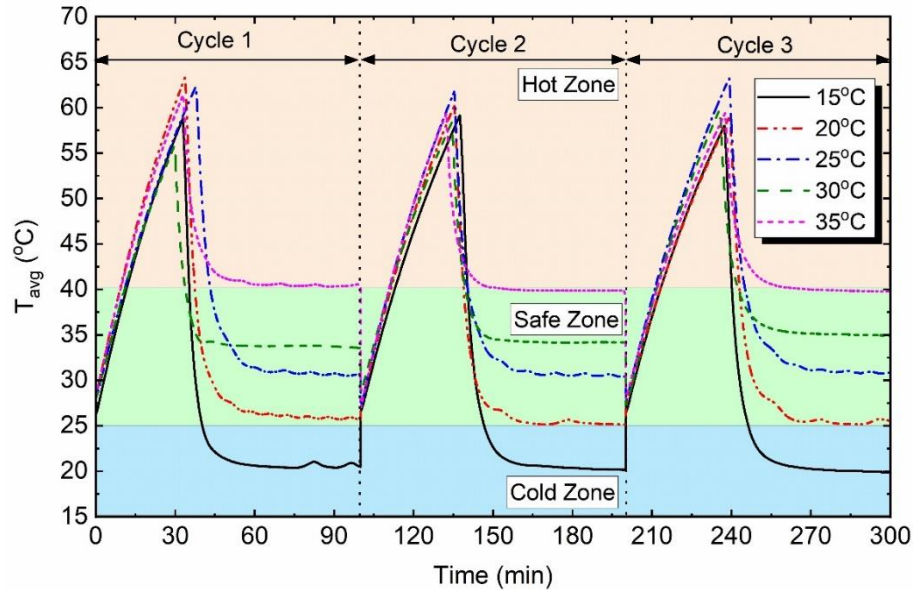


Fig. 2.6: Variation of temperature across the test module for different  $T_{w,in}$

Whereas a reverse trend is seen in  $h_w$  with an increase in  $T_{w,in}$  for the three cycles (Fig. 2.7). The  $h_w$  is seen to be higher with the lower  $T_{w,in}$ , indicating an effective heat transfer performance. For instance, in the case of cycle 1 and  $T_{w,in}$  of 15 °C, the  $h_w$  is 417.73 W m<sup>-2</sup> °C<sup>-1</sup> as the module reaches a steady state. At the same time, the  $h_w$  is as low as 42.22 W m<sup>-2</sup> °C<sup>-1</sup> with an increase in  $T_{w,in}$  to 35 °C. It is also noticed that at the beginning of the cooling process up to  $t = 10$  min, the  $h_w$  is very low, since the channels are not entirely filled with the liquid. It reaches a maximum value after  $t = 30$  min as the coolant flows along the channels; simultaneously, the contact surface between the coolant and channels increases. Eventually, the  $h_w$  of the liquid attains an equilibrium value along the module

surface. Besides this, minor oscillation in the  $h_w$  are seen in a few cases during cooling such as 20 °C, 25 °C and 35 °C. This is mainly caused by a variation in the coolant inlet temperature entering the cold plate since there always exists a temperature difference between the coolant leaving and the circulator bath, making it challenging to control the inlet temperature within the stipulated time period. Besides this, the  $\Delta P$  and  $P_{pump}$  are seen to reduce with the change in coolant temperature from 15 °C to 35 °C up to 33% (Table 2.3). In contrast, the  $\beta$  is seen to decrease due to a reduction in heat transfer compared to pump power with the rise of  $T_{w,in}$ .

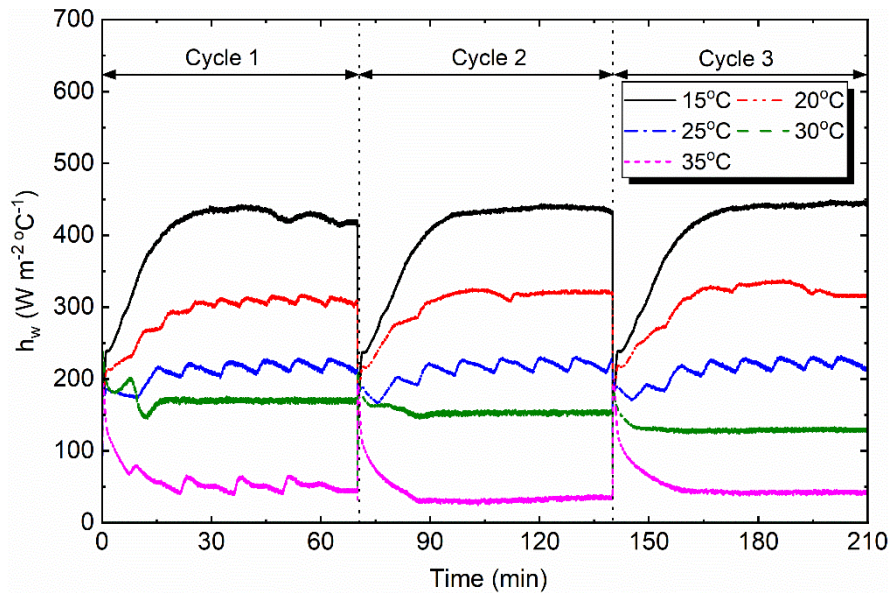


Fig. 2.7: Variation of  $h_w$  across the test module for different  $T_{w,in}$

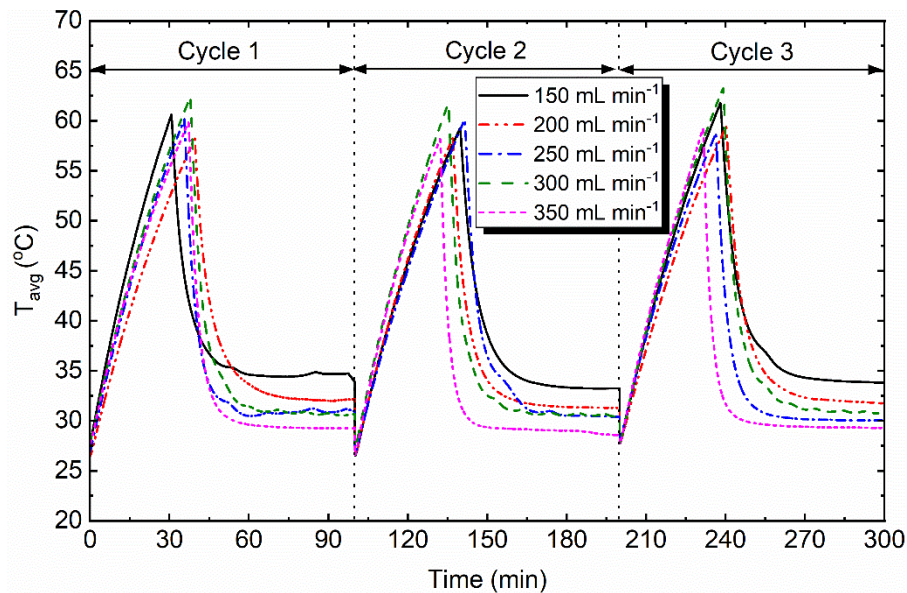
Based on the results, it can be suggested that a trade-off between  $\beta$  and  $T_{w,in}$ , is essential to optimize the battery performance. To achieve too low  $T_{w,in}$ , is a challenging task for an automobile. Similarly, beyond 30 °C of  $T_{w,in}$ , cannot provide adequate cooling of battery module. Hence,  $T_{w,in}$  between 20 °C to 25 °C is observed ideal to excel the life cycle of battery module.

Table 2.3: Performance metrics of the cooling system with the variation of coolant temperature

Parameter	$T_{w,in}$ (°C)				
	15	20	25	30	35
$\Delta P$ (kPa)	3.544	3.295	2.942	2.647	2.389
$P_{pump}$ (kW)	$1.77 \times 10^{-5}$	$1.65 \times 10^{-5}$	$1.47 \times 10^{-5}$	$1.32 \times 10^{-5}$	$1.19 \times 10^{-5}$
$\beta$ ( $\times 10^3$ )	3.08	3.03	2.34	1.92	1.02

### 2.4.3 Effect of varying flow rate

A suitable flow rate is necessary to operate the module under desired temperature range to meet the safety requirements. Therefore, flow rate,  $\dot{V}$  is varied from  $150 \text{ mL min}^{-1}$  to  $350 \text{ mL min}^{-1}$  to determine the cooling efficiency of the mini-channelled cold plate and the corresponding results are reported in Fig.'s 2.8 and 2.9. The coolant flow is maintained to be under the laminar regime. The  $T_{w,in}$  is maintained at  $25 \text{ }^\circ\text{C}$ , and experiments are performed under ambient conditions.

Fig. 2.8: Variation of temperature across the test module for different  $\dot{V}$ 

A linear relationship between the coolant flow rate and corresponding heat transfer across the module shows a continuous decrease of  $T_{avg}$ , and an increase in  $h_w$  with the rise of  $\dot{V}$

. After reaching the steady state (Cycle 1), for a  $\dot{V}$  of  $150 \text{ mL min}^{-1}$ , the  $T_{avg}$  is seen to be maximum with  $34.73 \text{ }^\circ\text{C}$  while maintaining a minimum  $h_w$  of  $109.99 \text{ W m}^{-2} \text{ }^\circ\text{C}^{-1}$ . With a rise of  $\dot{V}$  to  $350 \text{ mL min}^{-1}$ ,  $T_{avg}$  reduces to  $29.53 \text{ }^\circ\text{C}$  with an enhancement in  $h_w$  to  $276.77 \text{ W m}^{-2} \text{ }^\circ\text{C}^{-1}$ . In contrast, a sharp escalation of pressure drop and  $P_{pump}$  is seen with the increase of  $\dot{V}$  for the proposed cooling system (Table 2.4). At the same time, the performance factor  $\beta$  varies inversely with the  $\dot{V}$  and decreases by 64.67%, implying an increase in operational cost. Therefore, a trade-off between pressure drop and operational cost is essential to identify an optimized  $\dot{V}$ .

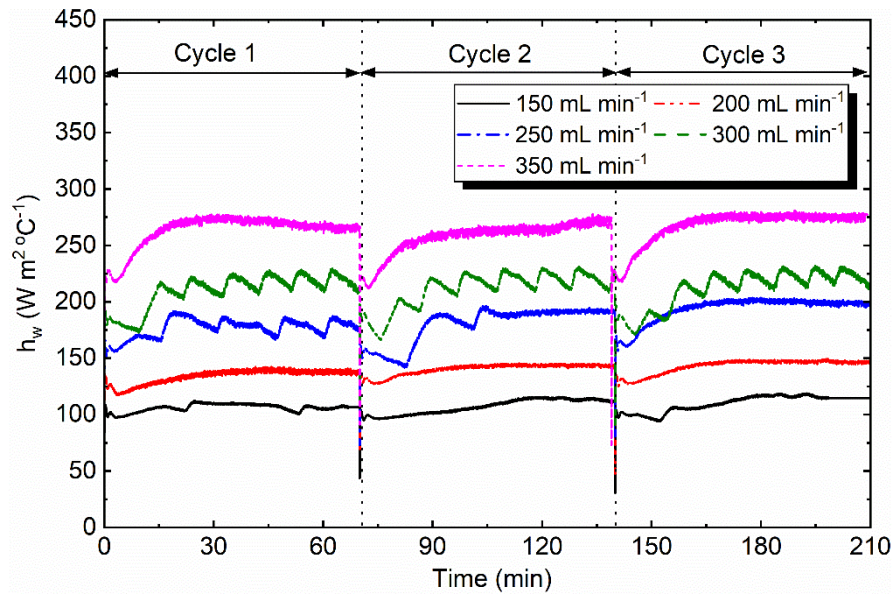


Fig. 2.9: Variation of  $h_w$  across the test module for different  $\dot{V}$

It may be noted that the change in  $T_{avg}$  as the  $\dot{V}$  exceeds from  $250 \text{ mL min}^{-1}$  to  $350 \text{ mL min}^{-1}$  is seen to be minimal, i.e. 4.2%. Therefore, a flow rate of  $250 \text{ mL min}^{-1}$  and a corresponding  $Re$  of 748.48 is found to be adequate and advantageous in maintaining a proper temperature distribution despite increased power and pumping costs. Hence, it is considered as the optimal choice for further experiments. However, an appropriate flow

rate has to be maintained to reduce the  $\Delta P$  and to enhance the  $h_w$  for better cooling of batteries in actual operating conditions.

Table 2.4: Performance metrics of the cooling system with the variation of  $\dot{V}$

Parameter	$\dot{V}$ (mL min <sup>-1</sup> )				
	150	200	250	300	350
$\Delta P$ (kPa)	2.029	2.683	2.865	2.942	3.096
$P_{pump}$ (kW)	$5.07 \times 10^{-6}$	$8.94 \times 10^{-6}$	$1.19 \times 10^{-5}$	$1.47 \times 10^{-5}$	$1.81 \times 10^{-5}$
$\beta$ ( $\times 10^3$ )	6.03	3.31	2.62	2.34	2.13

In addition to the above results, the efficacy of an aluminium flat tube (Fig. 2.10) in a cold plate resembling a compact heat exchanger is assessed for different flow rate conditions considering a non-dimensional factor  $j/f$  as an evaluation index.

$$j = Nu / Re \cdot Pr^{1/3} \quad (2.7)$$

The Prandtl number,  $Pr$ , is assumed as 6.22 for water at 25°C. The local Nusselt number,  $Nu$  is calculated using the correlation proposed by (Jung and Kwak 2008) as:

$$Nu = 0.000972 \cdot Re^{1.17} \cdot Pr^{0.3} \quad (2.8)$$

The local heat transfer coefficient,  $h_{w,local}$  (W m<sup>-2</sup> °C<sup>-1</sup>) is calculated as:

$$h_{w,local} = Nu \cdot k / D_h \quad (2.9)$$

here,  $k$  represents the thermal conductivity of the fluid (W m<sup>-1</sup> °C<sup>-1</sup>). A resistance coefficient,  $f$ , defined as the frictional potency between fluid flow and channel surface and is computed using the correlations proposed by Jiang et al. (Jiang *et al.* 2001) as:

$$f = 1639 / Re^{1.48} \quad Re < 600 \quad (2.10)$$

$$f = 5.45 / Re^{0.55} \quad 600 < Re < 2800 \quad (2.11)$$

The pressure drop,  $\Delta P$ , across the inlet and outlet of a channel (Pa), is estimated as:

$$\Delta P = 4fL\rho_w v_w^2 / 2D_h \quad (2.12)$$

here,  $L$  is the channel length (m),  $\rho_w$  signifies the density ( $\text{kg m}^{-3}$ ) and  $v_w$  indicates the velocity of coolant ( $\text{m s}^{-1}$ ).

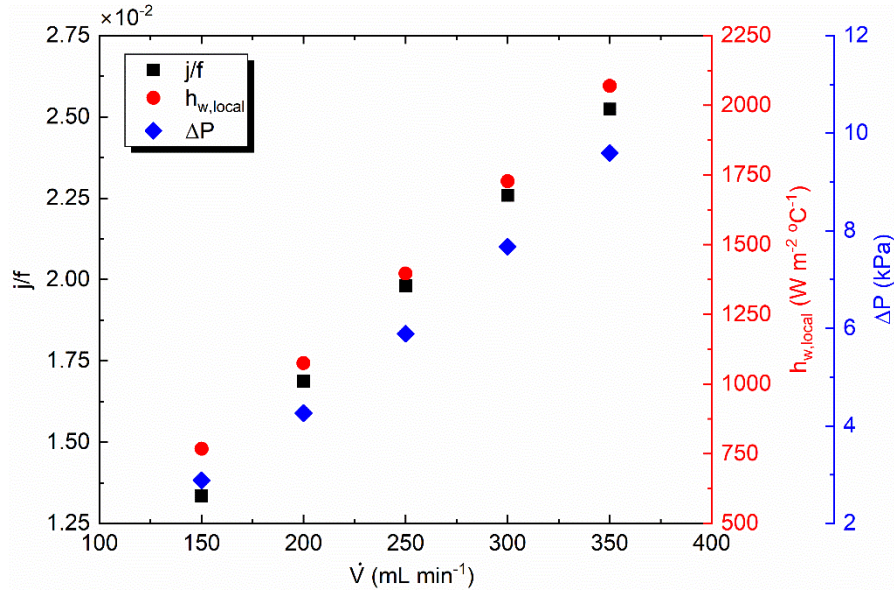


Fig. 2.10: Effect of varying  $\dot{V}$  on the heat transfer and pressure drop across an aluminium flat tube in cold plate

The energy consumption across the inlet and outlet of flow domain is mainly contributed by pressure drop which is again dependent on the frictional losses. It can be seen from Fig. 2.9 that with lower flow rate, the pressure losses are seen to be small, at the expense of poor heat transfer performance. However, with a rise in  $\dot{V}$  from 150 to 350  $\text{mL min}^{-1}$ , the  $h_{w,local}$  increases by 2.9 times, while the pressure drop is 3.32 times higher. Whereas its effect on the  $j/f$  factor is seen to be marginal. Despite a lower friction factor,  $j/f$  factor is seen to be increasing with flow rate due to a rise in convective heat transfer. These results specify that a careful consideration of cooling plate design is required to attain effective cooling.

### 2.4.4 Effect of varying flow direction

As the proposed channel works with the principle of a heat exchanger, the flow directions of the coolant have some evident consequences on the system's overall heat transfer performance. Hence, four different flow arrangements of parallel and counter flow directions with reverse entry points (Fig. 2.11) are considered with  $250 \text{ mL min}^{-1}$  and  $25^\circ\text{C}$  as the flow rate and coolant temperature, respectively and a cyclic test is performed (Fig. 2.12).

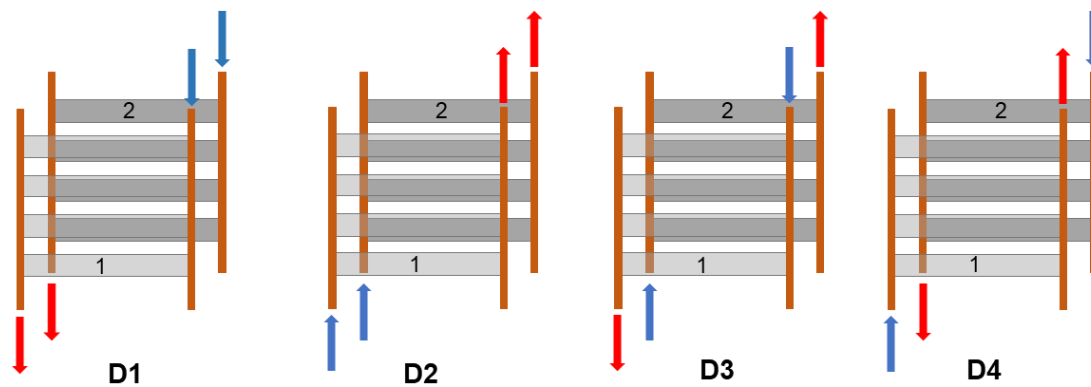


Fig. 2.11: Schematic representation of different flow arrangements across the channels

For a fixed cold plate arrangement and continuous heating process, the counter flow arrangements show better temperature reduction over the parallel flow arrangements for the test module. For instance, in the case of cycle 3, the difference in  $T_{avg}$  between D1 with the other directions D2, D3 and D4 is noticed to be  $1.66^\circ\text{C}$ ,  $1.55^\circ\text{C}$  and  $3.23^\circ\text{C}$ , respectively. However, the change in the direction of flow arrangement in cold plate (D2 and D3) showed a reduction in the overall heat transfer performance,  $h_w$  of the module (Table 2.5). An analogous behaviour is seen with the  $\beta$ . Moreover, the  $\Delta P$  and  $P_{pump}$  are seen to increase with directions D2, D3 and D4 when compared with D1 by 15.07%, 30.15% and 28.69%, respectively. Despite a slight increase in temperature, the direction



D1, indicating parallel flow arrangement, is chosen for further investigation, considering the overall cooling performance.

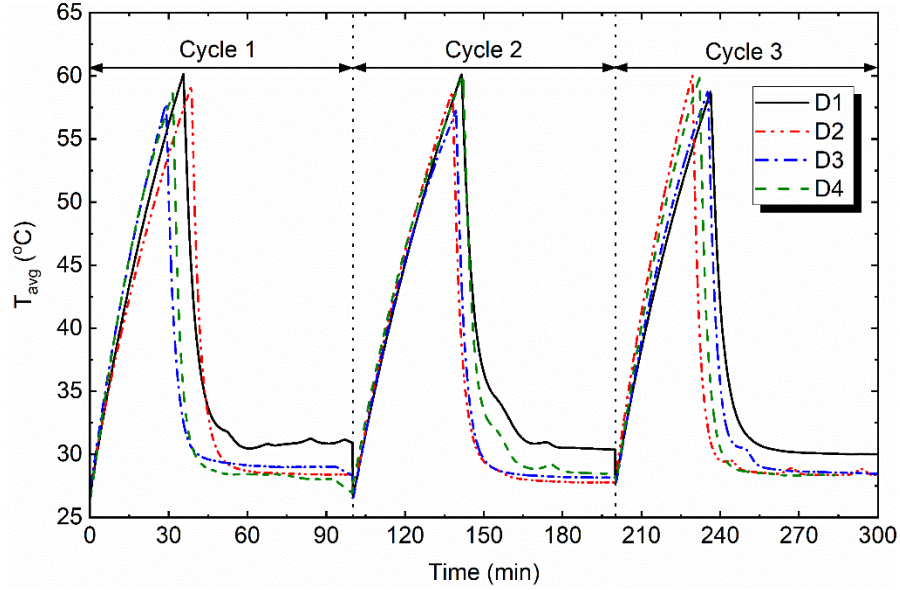


Fig. 2.12: Variation of temperature across the test module for different flow direction

Table 2.5: Performance metrics of the cooling system with the variation of flow direction

Parameter	Direction			
	D1	D2	D3	D4
$h_w$ ( $\text{W m}^{-2} \text{ }^\circ\text{C}^{-1}$ )	185.59	141.49	157.19	195.91
$\Delta P$ (kPa)	2.865	3.297	3.729	3.687
$P_{\text{pump}}$ (kW)	$1.19 \times 10^{-5}$	$1.37 \times 10^{-5}$	$1.55 \times 10^{-5}$	$1.54 \times 10^{-5}$
$\beta$ ( $\times 10^3$ )	2.62	1.12	1.30	1.17

### 2.4.5 Effect of pulse load test on cooling effectiveness

A pulse test is performed with heat loads varying from 10V to 40V, which exists for about 5 hours with a rest period in between to analyze the temporal behaviour of the module, as shown in Fig. 2.13. The temperature and heat flux change in response to the load applied are reported in Fig. 2.14. The corresponding thermal images captured using an infrared camera (IR) are displayed in Fig 2.15.

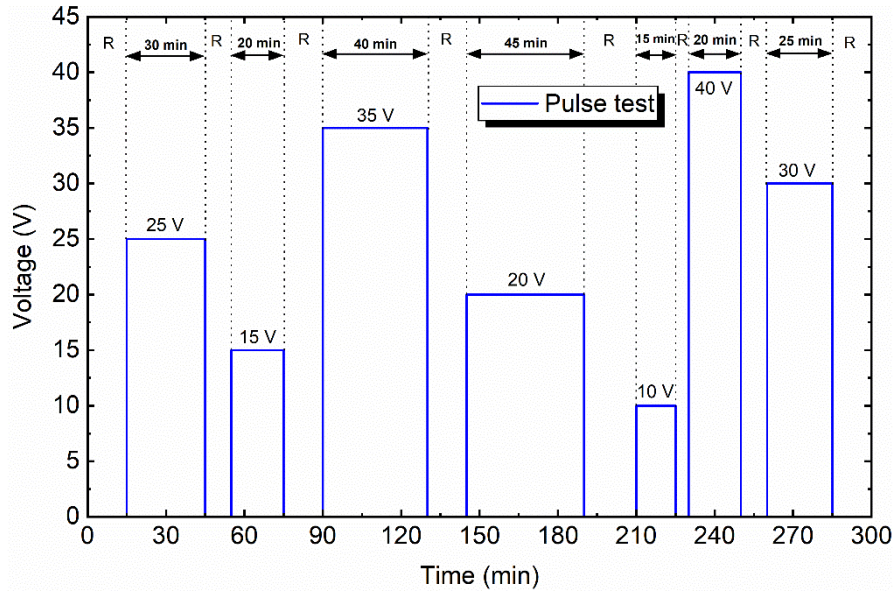


Fig. 2.13: Sampling curve of pulse load test

During the initial stages of heating, i.e., with voltages such as 25V, 15V and 35V, the  $T_{avg}$  of module reaches 44.53 °C, 42.21 °C and 72.39 °C, respectively. At the same time, the corresponding heat flux values are 197.64 W m<sup>-2</sup> °C<sup>-1</sup>, 165.72 W m<sup>-2</sup> °C<sup>-1</sup>, and 529.72 W m<sup>-2</sup> °C<sup>-1</sup>. In the later part of the cycle, when some residual heat exists in the module, with the change in voltage to 40V and 30V, the  $T_{avg}$  reaches a maximum of 70.91 °C and 71.6 °C with an increase in heat flux to 634.425 W m<sup>-2</sup> °C<sup>-1</sup> and 658.30 W m<sup>-2</sup> °C<sup>-1</sup>, respectively. Besides this, the deviation between the measured and thermal images is less than 2 °C, which is agreeable. This can be attributed to block emissivity and the distance from which the image is captured. For instance, at  $t = 70$  min, Points 1, 2 and 4 show a maximum difference of 0.78 °C, while it is 1.5 °C with Point 5 (Fig. 2.15). A similar phenomenon is seen in other cases. The cooling is initiated (red dotted line) as the  $T_{avg}$  of module attains 45 °C while maintaining the flow rate and coolant temperature at 250 mL min<sup>-1</sup> and 25 °C, respectively. It can be noted that even at high heating rates like 35V, the proposed cooling

arrangement could maintain the module's temperature below 30 °C. After a certain time period, with the progress in cooling, the temperature distribution across the module and corresponding heat flux stabilized, implying a heat balance. These results specify that the mini-channelled cold plate could maintain the temperature distribution across the module even under dynamic conditions within a safe range.

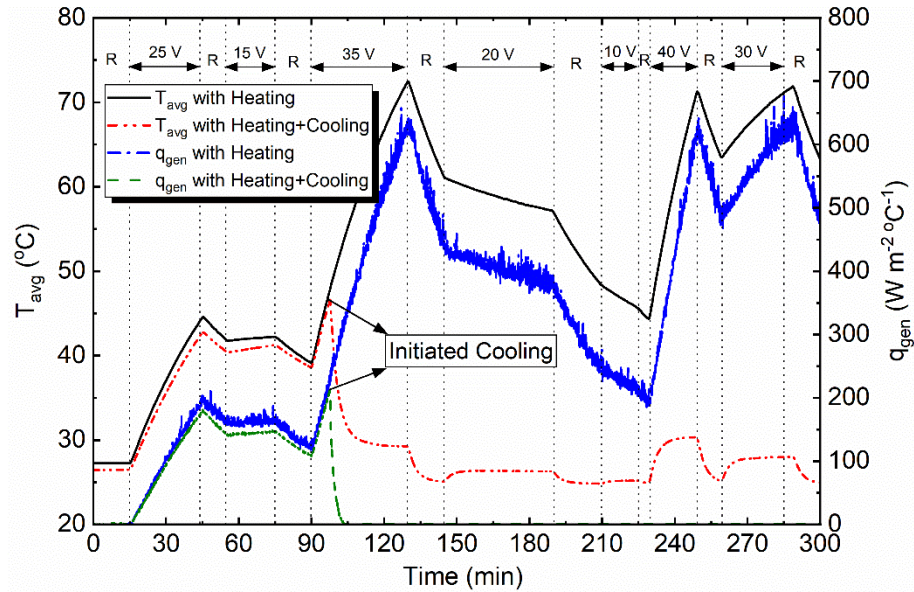


Fig. 2.14: Variation of temperature and heat flux across the test module with and without cooling under pulse load test

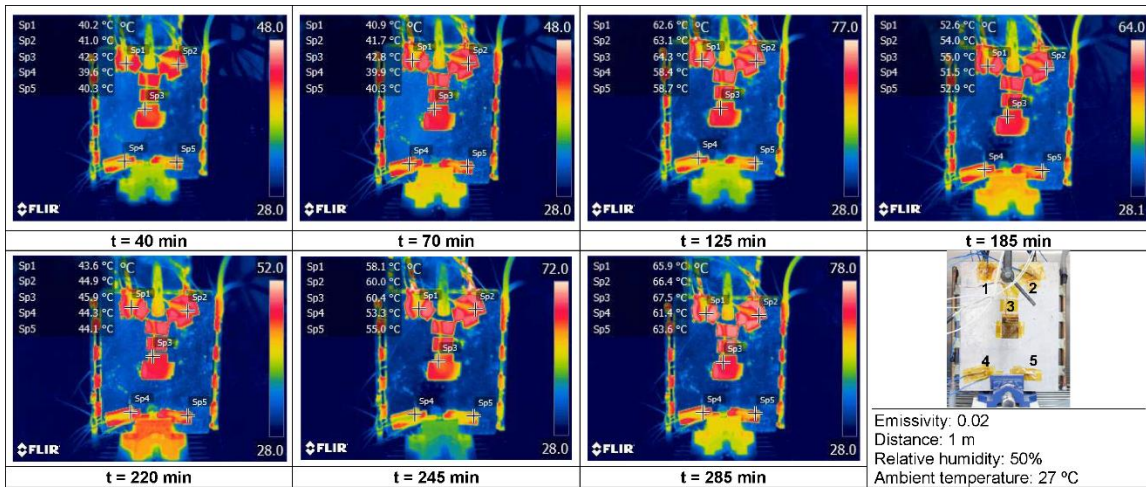


Fig. 2.15: Thermal images of the test module captured on heating at different time intervals under pulse load test

## 2.5 Summary

A thermal management strategy of a 20Ah pouch type battery module for EV or HEV application is experimentally evaluated by using a battery simulator integrated with an indigenously designed mini-channel cold plate for a wide variation of operating characteristics. The critical insights based on the present investigation are as follows:

- A coolant temperature range of 20 °C to 25 °C is observed to be ideal for upholding the test module within the desired range of 25 °C-40 °C for a coolant flow rate of 300 mL min<sup>-1</sup>.
- A coolant flow rate of 250 mL min<sup>-1</sup> and the corresponding  $Re = 748.48$  provides a balance between pressure drop (2.86 kPa) and heat transfer capability ( $h_w = 176.71$  W m<sup>-2</sup> °C<sup>-1</sup>).
- A parallel flow arrangement with a coolant inlet port near to the heating region is found to be the best choice with  $h_w = 185.59$  W m<sup>-2</sup> °C<sup>-1</sup> and  $\beta = 2.17$ , despite a slight increase in temperature.

Based on the results, it can be concluded that the temperature of the test module retained within the optimal range, justifying the use of a cold plate comprising rectangular mini channels in ensuring better thermal management. However, there are some other channel geometries reported by few researchers which cannot be fully ignored. Therefore, it is essential to compare the thermal-hydraulic performance of existing channel designs used for BTMS.

# Chapter 3

## Comparative Assessment among Several Channel Designs with Constant Volume for Cooling of Pouch-type Battery Module

### Keywords

Lithium-ion battery;  
Thermal management;  
Channel profile;  
Temperature  
uniformity;  
Drive cycle

*A three-dimensional numerical method is utilised to explore the laminar flow of liquid coolant in six distinct mini channel designs with a constant channel volume. This includes serpentine, U-bend, straight, pumpkin, spiral, and hexagonal designs. Their cooling ability is evaluated in terms of pressure drop, a non-dimensional  $j/f$  factor, average temperature, and cooling performance factor for varying mass flow rate and a fixed discharge rate of 3C. Also, a realistic drive cycle data US06 is utilised to assess the performance of optimal design obtained from the above results for on-road driving conditions.*

### 3.1 Introduction

Liquid cooling has proven to be a promising and preferable cooling solution owing to its superior cooling ability and technical feasibility (Tong *et al.* 2015; Rao *et al.* 2017). As established in Chapter 2, a cold plate with coolant flowing inside the micro/mini channels offers effective heat transfer performance. To date, a substantial amount of research has been conducted on the profile of mini-channel cold plates as they show an immense effect on the efficacy of the overall cooling system. Besides this, a simple way to achieve homogenous temperature distribution across the batteries is by raising the coolant flow rate. However, the rising flow rate upsurges the parasitic power supplied and thus can adversely affect the entire cooling system's performance. As an alternative method, numerous cooling channel designs have been proposed such as straight (Qian *et al.* 2016;

Monika *et al.* 2021), serpentine (T. Deng *et al.* 2018; Sheng *et al.* 2019; Jarrett and Kim 2011), U-bend (Patil *et al.* 2020; S Panchal *et al.* 2017), diverse mini-channels (Huang *et al.* 2019; An *et al.* 2019), and bifurcation (Deng *et al.* 2019), etc. In line with these, Rao and Xuan Zhang (2019) numerically analysed the impact of flow rate, branching structure, and cooling area on the thermal dissipation efficiency of a lithium-ion battery module embedded with a wedge-shaped microchannel cold plate. Xu *et al.* (2019) reported the influence of operating and climatic conditions by placing a cover plate with a T-shape bifurcation structure on either side of a large-capacity battery module. The authors conclude that multiple cold plates are essential for the proper coolant distribution with enhanced temperature uniformity.

Despite the widespread research on the fluid flow characteristics and heat transfer efficacy of different cooling channel designs, no conclusive decision with global standards has been made. Also, to the best of the author's understanding, there is not much insightful information available in previous studies on how the profile of various channel designs under a constant volume would impact the cooling effectiveness or evaluate them against each other for a given battery type in cooling purposes, and this has emboldened the present study.

From this perspective, the present study compares various channel configurations with different complexities aimed at a particular battery module. The primary objective of this work is to analyse, as a proof of concept, the ability of six different channel designs under a constant channel volume. This includes conventional cooling plate designs such as serpentine (Sheng *et al.* 2019), U-bend (S. Panchal *et al.* 2017), straight/rectangular (Qian *et al.* 2016), and pumpkin (Huang *et al.* 2019) for cooling pouch battery modules at a higher

discharge rate (3C-60A). Along with these, a hexagonal design inspired by Yang *et al.* (2019) and a spiral design adopted from the labyrinth concept are also considered for the first time in battery cooling applications. A numerical method is employed to analyse and compare the impact of different cooling plate designs on battery thermal performance by altering the coolant mass flow rate.

Furthermore, the cooling proficiency of different channel designs is assessed quantitatively based on exclusive factors such as fluid flow distribution characteristics, local temperature variation across the mid-battery surface,  $j/f$  factor, average temperature and cooling performance factor. In addition to this, simulations are performed with all the considered designs for ambient temperature ranging from 25 °C to 45 °C. Later, the cooling effectiveness of the optimal design attained based on the above comprehensive analysis is evaluated using realistic drive cycle data. The design that has enhanced cooling ability for a constant volume, resulting in homogeneous temperature distribution across the battery module, is considered better.

## 3.2 Methodology

### 3.2.1 Physical problem

In general, a Li-ion battery pack of an EV has several modules connected in a specific pattern. Each module consists of thousands of cells arranged in series or parallel combinations based on the design requirement of an EV. Each module is composed of several cold plates to regulate the thermal distribution. If the batteries are rectangular, the cold plates can be placed between the successive battery's gap. The module's inner temperature is examined and regulated by adjusting the liquid flow rate and temperature.

Fig. 3.1 represents a battery module constructed by stacking up to five pouch-type cells in series, each with a nominal capacity of 20Ah and a size of 160×227×7.25 mm. The technical details of a single 20Ah pouch cell are reported in Table 3.1. A cold plate with a thickness of 2 mm is placed between two consecutive batteries. The heat generated from a battery is transferred by conduction to the cold plate, followed by that heat being carried away through convection with a coolant flowing along the mini channels. Half of the domain is considered to curb computational time by taking advantage of the battery module's symmetric nature. The battery is assumed to be a solid model with anisotropic thermal conductivity and uniform heat generation for simplifying the three-dimensional (3D) model, whereas the coolant is presumed to be steady, incompressible, and laminar.

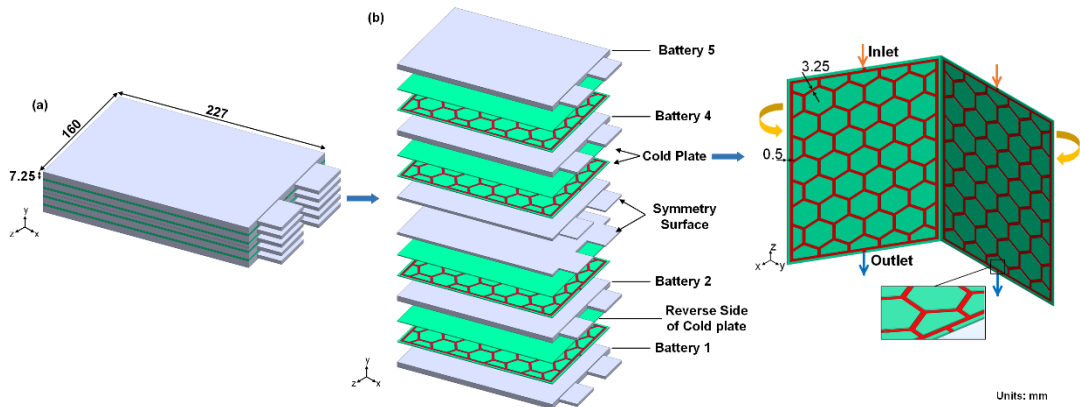


Fig. 3.1: (a) Battery module embedded with cold plate and (b) Schematic diagram of a battery module integrated with the hexagonal channel design cold plate.

Table 3.1: Technical specifications of the pouch cell

Parameter	Value
Type	Lithium iron phosphate
Cathode	LiFePO <sub>4</sub>
Anode	Graphite
Electrolyte	Carbonate based
Volume (mm <sup>3</sup> )	160 (w) × 227 (h) × 7.25 (t)
Nominal capacity (Ah)	20
Maximum voltage (V)	4.0
Minimum voltage (V)	2.1
Maximum charge/discharge current (A)	20 (1C), 60 (3C)



### 3.2.2 Proposed channel configurations

The performance of cold plates with six different mini-channel designs is compared, considering a pouch battery module without hindering their total channel volume. The channel profiles range from straight, serpentine, U-bend, and pumpkin to complex structures like a spiral and hexagonal (Fig. 3.2). The coolant is assumed to flow at a constant mass flow rate from each mini channel's inlet to the outlet. The geometric details of different channel configurations are reported in Table 3.2. Furthermore, to guarantee fidelity in comparing the cooling performance of each channel design, the channel width and number of channels in the cold plate are varied to maintain a constant volume for a channel height fixed at 1 mm.

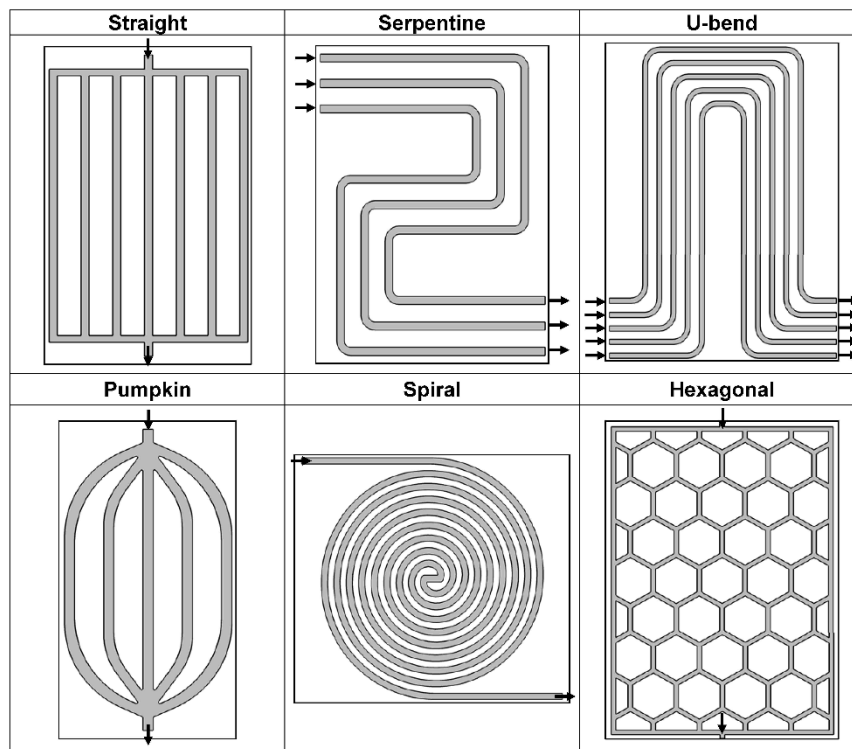


Fig. 3.2: Models of six different cooling plate designs

The overall difference in several retrofitted channel volumes relative to straight channel design is less than 5% (Table 3.2). As the present work corresponds only to laminar flow, an accurate numerical solution is sufficient for a close-reality. The present work focuses on identifying channel profiles that offer superior cooling for pouch battery modules under high discharging conditions. In this context, rigorous 3D numerical simulations are conducted for all the considered designs for a discharge rate of 3C using COMSOL Multiphysics software. The assumptions made and the corresponding governing equations are described in detail in the forthcoming subsection.

Table 3.2: Dimensions of mini channels in the cold plate

Parameter	Straight	Serpentine	U-bend	Pumpkin	Spiral	Hexagonal
$W_c$ (mm)	5	5.44	3.46	7.1	3.8	3.25
No. of channels	7	3	5	5	4(turns)	Multi
$V_f$ (mm <sup>3</sup> )	8238	8232	8233	8238	8236	8633
Relative Error (w.r.t. straight) (%)	NA	0.07	0.06	0	0.02	4.79

### 3.2.3 Control equations

In the following section, the evolution of the 1D model in conjunction with the energy balance equation, which is used to regulate the temperature change during the charging or discharging cycle of a cell, is provided.

#### *ECT model equations*

For battery modelling in COMSOL, the 1D electrochemical (ECM) model summarized by the leading equations of the electrodes and separator, comprising the variation of salt concentration in electrodes and separator, are used. Additional details of parameters and the reaction kinetics utilized for the present Li-ion cell model study are provided in the literature. The equations relating the liquid phase of the composite electrode are expressed as:

$$\varepsilon \frac{\partial c}{\partial t} = \nabla \cdot (D \nabla c) - \frac{i_2 \cdot \nabla t_{\pm}^0}{F} + a j_n (1 + t_{\pm}^0) \quad (3.1)$$

where,  $\varepsilon$  represents the volume fraction,  $c$  defines the salt concentration,  $D$  indicates the salt diffusion coefficient,  $a$  signifies the specific interfacial area, and the subscript  $\pm$  denotes to the positive electrode.  $i_2$  and  $a j_n$  are estimated by using the following equations:

$$i_2 = -k \nabla \phi_2 + \frac{2kRT}{F} + \left( 1 + \frac{\partial \ln f_{\pm}}{\partial \ln c} \right) (1 - t_{\pm}^0) \nabla \ln c \quad (3.2)$$

$$a j_n = \frac{1}{F} \nabla \cdot i_2 \quad (\text{Note: for separator } j_n=0) \quad (3.3)$$

The equations relating the solid phase of the composite electrodes are represented as:

$$i_1 = -\sigma \nabla \phi_1 \quad (3.4)$$

$$\frac{\partial c_s}{\partial t} = D_s \left[ \frac{\partial^2 c_s}{\partial r^2} + \frac{2 \partial c_s}{r \partial r} \right] \quad (3.5)$$

where  $\sigma$  signifies the solid matrix electronic conductivity,  $c_s$  indicates the concentration of lithium ions in the solid, and  $D_s$  represents the diffusion coefficient of Li-ion in the solid electrode.

The Butler-Volmer equation relates both the phases of composite electrodes as:

$$D_s \frac{\partial c}{\partial r} = -j_n \quad (3.6)$$

$$j_n = k (c)^{0.5} (c_i - c_s)^{0.5} (c_s)^{0.5} \left\{ \exp \left( \frac{F}{2RT} (\eta - U) \right) - \exp \left( -\frac{F}{2RT} (\eta - U) \right) \right\} \quad (3.7)$$

where,  $\eta$  is the electrode potential and is given by:

$$\eta = \phi_1 - \phi_2 \quad (3.8)$$

here,  $\phi_1$  represents the solid phase potential, and  $\phi_2$  is the electrolyte phase potential. The equation that relates  $k$  and  $i_0$  is presented as follows:

$$i_0 = Fk(c)^{0.5}(c_i - c_s)^{0.5}(c_s)^{0.5} \quad (3.9)$$

where,  $i_0$  is the current exchange density,  $F$  is Faraday constant, and  $c_s$  is the Li-ion concentration on the surface of active particles.

### ***Heat transfer model***

The mathematical model consists of three sub-domains: a battery, a cold plate (solid domain) of aluminium, and water (fluid domain) as the coolant, which concedes for a conjugate heat transfer between the battery and channel wall. The energy conservation equation regulating the battery operation is expressed as:

$$\frac{\partial}{\partial t}(\rho_b c_{p,b} T_b) = \nabla \cdot (K_b \nabla T_b) + Q_{gen} \quad (3.10)$$

The battery's heat generation rate substantially contributes to 3D temperature distribution within the battery. The heat generation in a battery cell can be attributed to two primary sources (i) entropy change due to electrochemical reactions within the cell and (ii) joule or ohmic heating (Ruan *et al.* 2021). Based on this, the empirical formula abridged by Bernardi *et al.* (1985) for estimating heat generation rate is as follows:

$$\dot{Q}_{gen} = Q_{irr} + Q_{rev} = I(E_{OCV} - E) - IT_b \left( \frac{\partial E_{OCV}}{\partial T_b} \right) \quad (3.11)$$

here,  $Q_{irr}$  and  $Q_{rev}$  represent irreversible (Joule heat) and reversible heat (reaction heat);  $I$ ,  $E$ , and  $T_b$  signify discharge current, load voltage and battery temperature, respectively.  $E_{OCV}$  is the open-circuit voltage, a function of  $T_b$  and the state of charge (SOC) as  $E_{OCV} = f(T_b, SOC)$ . The term  $IT(\partial E_{OCV}/\partial T_b)$  signifies the reversible reaction heat generation and can be neglected. The simplified heat generation rate reformulated by Fathabadi (2014) is as follows:

$$\dot{Q}_{gen} = -T_b \Delta S \frac{1}{nF} + I^2 R \quad (3.12)$$

here,  $I$  is current;  $\Delta S$  is the entropy change;  $F$  is Faraday constant;  $n$  is the number of electrons related to the electrochemical reactions;  $R$  is the resistance.

The heat generated by the battery is presumed to be uniform. However, the thermal conductivity is considered to be anisotropic. Moreover, a convective boundary condition prevails on the exterior surfaces of the battery module. The amount of heat rejected from the module to the atmosphere can be obtained using Newton's law of cooling.

$$q_a = h_a (T_b - T_a) \quad (3.13)$$

Where,  $h_a$  is the heat transfer coefficient of air assumed as  $5 \text{ W m}^2 \text{ }^\circ\text{C}^{-1}$ . The cold plate is made of aluminium with isotropic properties. Water is used as the cooling fluid inside the mini-channel cold plate.

The physical properties of the coolant are assumed to be constant (Table 3.3), and a steady-state assumption is followed. Moreover, considering the flow efficiency, the flow is anticipated as laminar to lower the pressure loss. The governing equations for Newtonian, laminar and incompressible flow of fluid through the mini channels of a cold plate are expressed as (Huo *et al.* 2015):

$$\text{Energy: } \rho_f c_f \frac{\partial T_w}{\partial t} + \nabla \cdot (\rho_f c_f \vec{v} T_f) = \nabla \cdot (K_f \nabla T_f) \quad (3.14)$$

$$\text{Continuity: } \nabla \cdot \vec{v} = 0 \quad (3.15)$$

$$\text{Momentum: } \rho_f \left[ \frac{\partial \vec{v}}{\partial t} + (\vec{v} \cdot \nabla) \vec{v} \right] = -\nabla P + \mu \nabla^2 \vec{v} \quad (3.16)$$

Table 3.3: Thermal properties of coolant and cold plate (Huo *et al.* 2015)

Parameter	$\rho$ (kg m <sup>-3</sup> )	$c_p$ (J kg °C <sup>-1</sup> )	$k$ (W m <sup>-1</sup> °C <sup>-1</sup> )	$\mu$ (Pa s)
Water	998.2	4128	0.6	1.003×10 <sup>-3</sup>
Aluminium	2719	871	202.4	-

### 3.2.4 Boundary conditions

The following boundary conditions are used in the present study:

- a) Mass flow rate is given at the channel inlet

$$\dot{m}_w = \dot{m}_in, T = T_in \quad (3.17)$$

Where  $\dot{m}_w$  is varied from 0.001 kg s<sup>-1</sup> to 0.005 kg s<sup>-1</sup>,  $T$  is the reference temperature, and

$T_in$  is the initial temperature of the battery and cold plate.

- b) The pressure is specified at the outlet

$$p = p_{out} = 0 \text{ Pa} \quad (3.18)$$

- c) Symmetry is applied, and half of the module is considered

$$-n \cdot q = 0 \quad (3.19)$$

- d) Convective boundary condition is applied at the exterior walls of the battery module and cold plate

$$-n \cdot q = h(T_a - T) \quad (3.20)$$

- e) No-slip condition is applied inside the flow channel walls

$$u = 0 \quad (3.21)$$

f) Thermal resistance between the battery and the cold plate is negligible

$$R_{th} = 0 \quad (3.22)$$

### 3.2.5 Numerical method

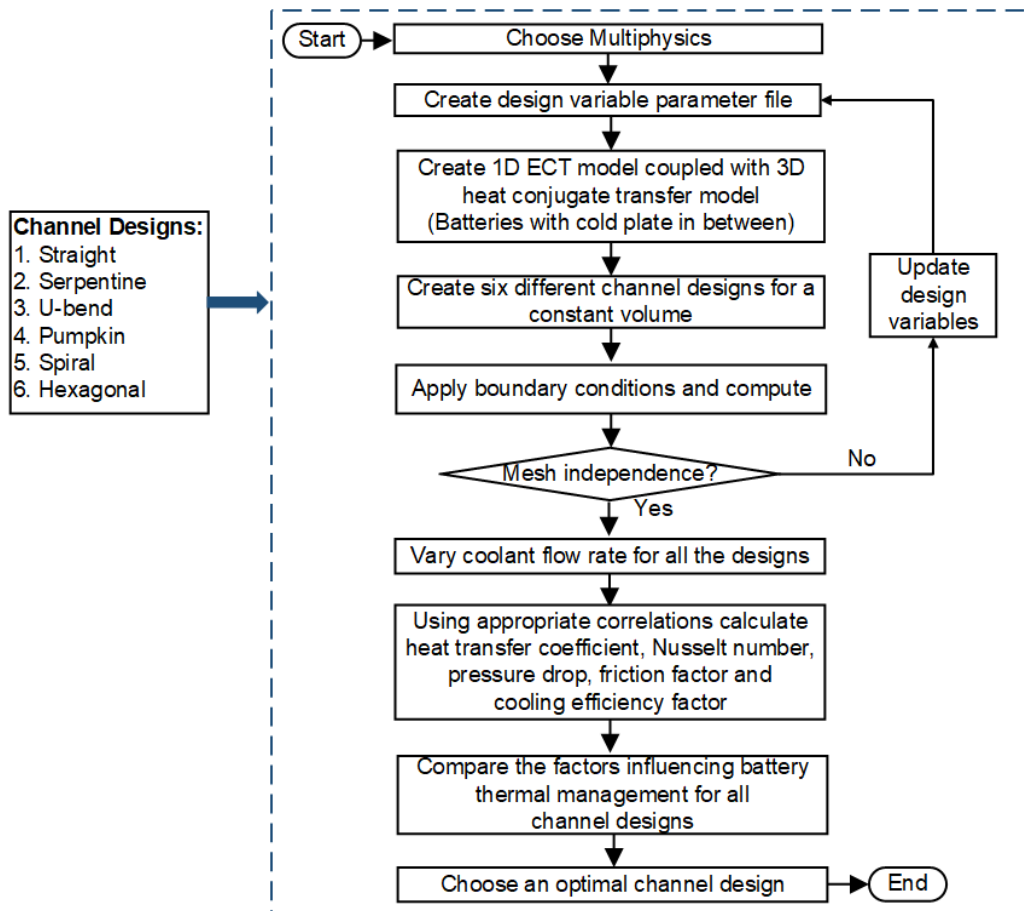


Fig. 3.3: Flow chart representing the simulation procedure

A finite element-based software, COMSOL Multiphysics 5.4, is utilised to solve the proposed BTMS. Meanwhile, CATIA V5 is used to design and develop the 3D geometric models of all the considered channel designs. Once the geometric modelling is completed, the respective solid models are imported into COMSOL for mesh generation and analysis. Simulations on the battery electro-thermal model (ECT) and cooling structure are performed by integrating two models. Initially, the transient 1D isothermal electrochemical

model estimates the electrochemical reactions inside the cell over the discharging course, resulting in electric current and heat generation. Later, the generated heat is utilised to predict the temperature distribution by combining it with the 3D conjugate heat transfer model. The detailed simulation scheme is explained in Fig. 3.3. The parameters used in solving the ECT model are listed in Tables 3.4 and 3.5. The thermo-physical properties of a battery, such as thermal conductivity, specific heat, and density, are volume averaged in the heat transfer section.

Table 3.4: Thermo-physical properties used for the present simulation (S. Panchal *et al.* 2017)

Parameter	Anode	Separator	Cathode
Thickness, $L$ ( $\mu\text{m}$ )	100	52	183
Initial electrolyte $\text{Li}^+$ concentration, $C_0$ ( $\text{mol m}^{-3}$ )	2000	2000	2000
Particle radius, $r_s$ ( $\mu\text{m}$ )	12.5	-	8
Maximum solid $\text{Li}^+$ concentration, $C_{s, \max}$ ( $\text{mol m}^{-3}$ )	31370	-	22806
Reference rate constant, $k$ ( $\text{mol m}^{-2} \text{s}^{-1} (\text{mol}^{-1} \text{m}^{-3})^{-1.5}$ )	2.072818e-11	-	2.072818e-11
Initial solid $\text{Li}^+$ concentration, $C_0$ ( $\text{mol m}^{-3}$ )	14870.6	-	3886.2
Volume fraction, $\epsilon$	0.357	1	0.444
Filler fraction, $\epsilon_f$	0.172	-	0.259
Conductivity, $\sigma$ ( $\text{S m}^{-1}$ )	100	-	3.8
Reference diffusivity, $D_s$ ( $\text{m}^2 \text{s}^{-1}$ )	3.9e-14	-	1e-13
Activation energy, $E_d$	2e4	-	8.6e4
Time acceleration factor, $t^+$	-	0.363	-
Bruggeman, $\beta$	1.5	1.5	1.5
Reference Temperature, $T$ ( $^\circ\text{C}$ )		25	-
Faraday constant, $F$ ( $\text{C mol}^{-1}$ )		96,485	
Minimum Voltage, $V_{\min}$ (V)		2.0	
Maximum Voltage, $V_{\max}$ (V)		4.1	

Table 3.5: Material and thermal properties

Parameter	$\rho$ ( $\text{kg m}^{-3}$ )	$c_p$ ( $\text{J kg}^{-1} \text{ }^\circ\text{C}^{-1}$ )	$k$ ( $\text{W m}^{-1} \text{ }^\circ\text{C}^{-1}$ )
Positive tab	2719	871	202
Negative tab	8978	381	387.6
Active battery material	2092	678	18.2

In simulations, the 1D model and 3D conjugate model integrated through a variable heat generation is specified by:

$$\dot{Q}_g = nojac \left[ \text{comp1.aveop1}(\text{comp1.liion}.Q_g) \right] \times (L_{neg} + L_{sep} + L_{pos}) / L_{batt} \quad (3.23)$$



here,  $\dot{Q}_g$  indicates heat generated per unit volume in the 1D model (comp1.liion) by coupling cathode, anode, and separator components (aveop.1). The  $L_{neg}$ ,  $L_{pos}$ ,  $L_{sep}$ ,  $L_{batt}$  signifies the lengths of anode, cathode, separator, and battery, respectively. Modules like 'heat transfer in solids and fluids' and 'laminar flow' are unified by Multiphysics 'non-isothermal flow'. The Paradiso time-dependent solver with a fixed tolerance limit of 0.001 is employed to solve the transient conjugate heat transfer model.

### 3.2.6 Grid sensitivity

A series of mesh independence tests are conducted for all the designs to attain an optimal number of nodes that is accurate and efficient without compromising mesh quality (Table 3.5). Regarding this, a free tetrahedral mesh with different size constraints is generated by discretizing the computational domain. A direct solver is employed for time-dependent study, and the relative tolerance is set to  $10^{-3}$ . The time step is set to 1s, and the temperature field progresses effectively. Also, the simulation can be much faster than solving coupled flow and heat equations.

The results of the grid sensitivity test performed for a straight channel design are depicted in Fig. 3.4. For this, the  $\dot{m}_w$  is set as  $0.002 \text{ kg s}^{-1}$ , whereas the coolant  $T_{w,in}$  and ambient temperature  $T_a$  are maintained at  $25 \text{ }^\circ\text{C}$ . The tests examined the dependency of calculated  $\Delta P$ , and average temperature  $T_{avg}$  on the number of discretized cells. Fig. 3.4 reveals that the factors  $\Delta P$  and  $T_{avg}$  turn out to be less dependent when the number of nodes exceeds  $1.93 \times 10^6$ . Hence, the finalized number of nodes for the straight channel design is perceived to be  $1.93 \times 10^6$ . For other channel designs, distinct number of nodes are ascertained to be optimal (Table 3.6). It is noticed that a grid number of more than  $3 \times 10^6$  is required to

simulate the serpentine, U-bend, and spiral designs accurately. On the contrary, a grid number of about  $1.9 \times 10^6$  is used to simulate the straight and hexagonal designs. This happens because designs with corner regions entail higher grid density due to complicated flow structures, whereas straight or parallel regions need lower grid density.

Table 3.6: Summary of mesh independence test results for a battery module integrated with different cooling channel designs at a  $\dot{m}_w$  of  $0.002 \text{ kg s}^{-1}$

Channel design	Number of nodes ( $\times 10^6$ )	$T_{avg}$ ( $^{\circ}\text{C}$ )	$\Delta P$ (Pa)
Straight	1.93	29.86	265.71
Serpentine	3.48	29.62	448.93
U-bend	3.34	29.87	433.83
Pumpkin	2.12	29.94	150.76
Spiral	4.79	30.66	10599
Hexagonal	1.96	29.68	534.23

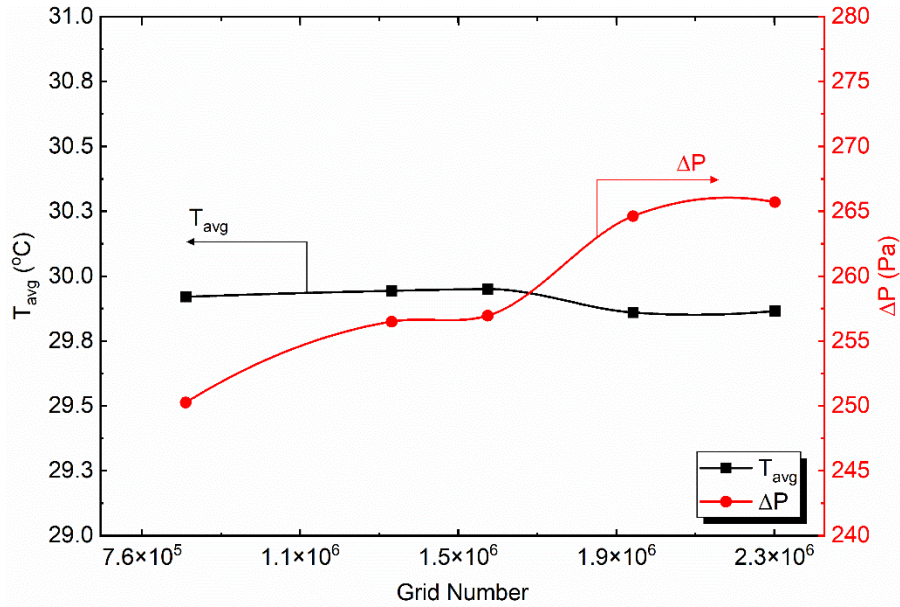


Fig. 3.4: Mesh independence test results of a straight channel design

### 3.2.7 Model validation

It is wise to validate the numerical observations with experimental results before proceeding. However, experimental observations with such a unique pouch-type battery module design for thermal management are not available in the existing literature.

Therefore, to mimic the experimental observations of S. Panchal *et al.* (2017), a single pouch type 20 Ah Li-ion battery deprived of any cold plate is numerically simulated and the mean temperature distribution of the LiFePO<sub>4</sub> battery at a discharge rate of 2C, 3C and 4C are estimated while the initial temperature for both the cases is fixed at 22 °C. The transient temperature variation of the pouch cell at various discharging rates and its 3D tetrahedron mesh structure denser at the electrodes for a better demonstration of the excess heat generated due to ECT reactions are reported in Fig. 3.5.

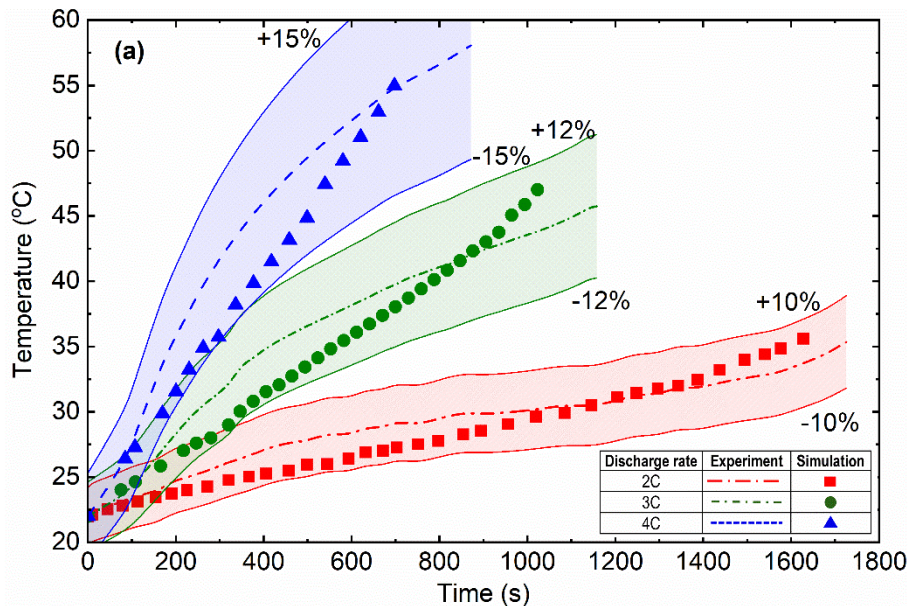


Fig. 3.5: Comparison between numerical and experimental results of a single battery

The results indicate that with the rise of the discharging rate, the average temperature of the pouch cell increases. However, the deviation between the experiment and simulation increases from 10% to 15% for an increase in discharge rate from 2C to 4C. This disparity is mainly because (a) the majority of the thermo-physical properties selected from the existing literature may differ from the aspects of the experimental system, (b) the usual lifecycle of a battery deteriorates with the duration of operation, and (c) the contact

resistance for the discharge process assumed to be constant for simulation leading to certain deviation from the experimental battery.

### 3.3 Results and discussion

#### 3.3.1 Distribution characteristics of various channel designs

One critical aspect that estimates the cooling effect is channel configuration since it directly influences the hydrodynamic and thermal performance of mini channels within the cold plate. In general, a higher  $\dot{m}_w$  improves heat transfer performance, thereby enhancing the temperature distribution across the battery surface within safe limits.

Table 3.7: Variation in  $D_h$ ,  $Re$  and  $L_{ch}$  for different designs under constant flow volume at a  $\dot{m}_w$  of 0.002

Channel design	kg s <sup>-1</sup>			
	$D_h$ (m)	$Re$	$L_{ch}$ (m)	Flow type
Straight	0.00166	664.67	3.24	laminar
Serpentine	0.00169	619.26	3.06	laminar
U-bend	0.00155	893.18	4.79	laminar
Pumpkin	0.00175	492.35	4.27	laminar
Spiral	0.00158	807.35	4.34	laminar
Hexagonal	0.00153	938.36	5.15	laminar

The velocity contours across the mid-profile plane of the cooling plate with different channel designs for a  $\dot{m}_w$  of 0.002 kg s<sup>-1</sup> are shown in Fig. 3.6. Even though channels have the same flow volume, the hydraulic diameter,  $D_h$ ,  $Re$  and channel length,  $L_{ch}$ , are seen to be varying due to their distinct profile (Table 3.7). As seen,  $L_{ch}$  is relatively longer in the case of hexagonal, serpentine, and U-bend designs when compared to straight, pumpkin, and spiral designs. Besides this, the flow type is maintained to be in a laminar regime for all considered designs.

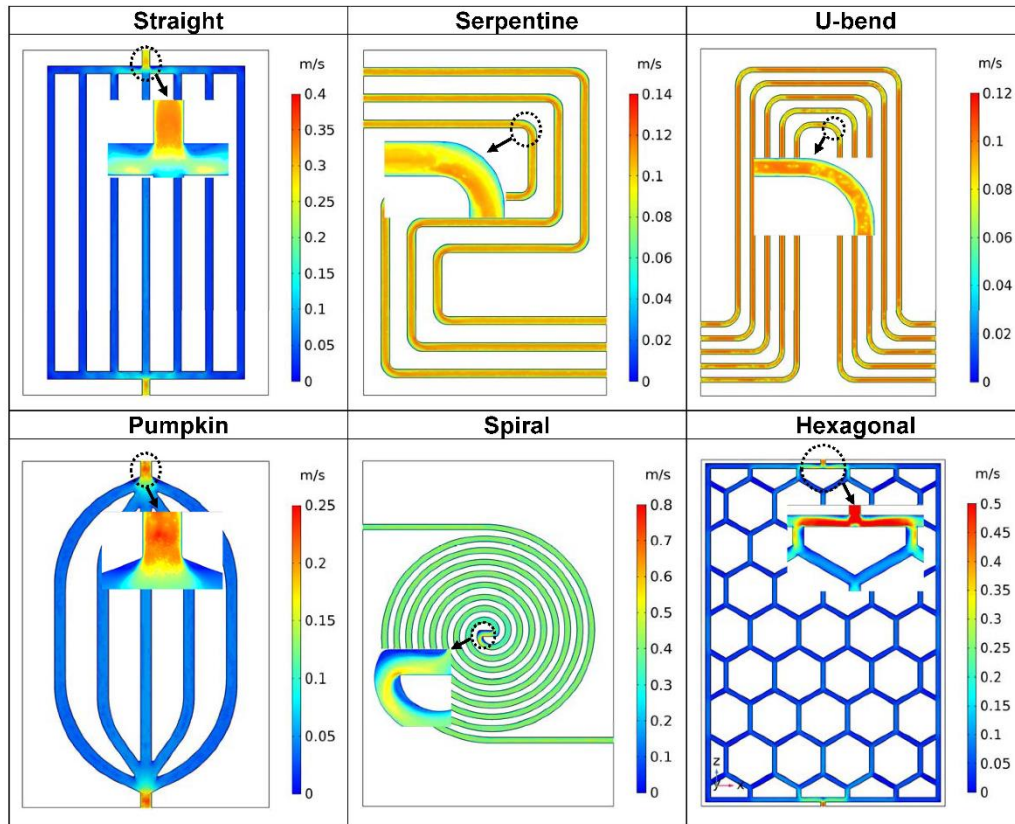


Fig. 3.6: Velocity contours at the mid-profile plane of different channel designs for a  $\dot{m}_w$  of  $0.002 \text{ kg s}^{-1}$

The velocity contours show that the flow pattern varies significantly with each design based on its profile. It is apparent from Fig. 3.6 that the serpentine, U-bend, and pumpkin channel designs show more uniform velocity distribution across the cold plate when compared to straight, spiral, and hexagonal designs. This is because, in the case of a simple straight or rectangular channel design, a difference in the velocity of the fluid is noticed between the mid-channel and remaining channels. A considerable amount of fluid is transferred away by the middle channel for a given flow rate, resulting in an insufficient distribution along with the cold plate width. Besides this, as the fluid diverts along the sharp corners, flow resistance increases, reducing velocity (Qian *et al.* 2016; Huo *et al.* 2015). This can be avoided with the adaption of the pumpkin model, which has smooth bends and wide fluid

passages (Huang *et al.* 2019). The maximum velocity obtained with the serpentine ( $0.14 \text{ m s}^{-1}$ ) and U-bend designs ( $0.12 \text{ m s}^{-1}$ ) is almost similar. In both these cases, a momentum transfer occurs at the outer walls of curved bends. Consequently, fluid rotation along the bulk flow axis leads to the growth of vortices around the bent shape. As a result, flow separation occurs, and velocity reduces in that particular region. For the spiral design, a disparity in velocity distribution is noticed throughout the flow path. This can be attributed to two reasons— a) When the fluid travels along a curved path, centrifugal forces generate a secondary flow. As an effect, velocity is no longer maximum at the center, but at some point, intermediate between center and wall surface, resulting in vortices formation; b) Also, a higher velocity variation is seen at the central region of a spiral design, as the fluid changes its direction from the inlet to outlet turn. While an interesting flow field is seen in a hexagonal design, the fluid entering through the main inlet is halved into the bifurcation channels, reducing its average velocity. The velocity of fluid upsurges abruptly as it passes through the tapering channels. This leads to an increase in turbulence and shear stress, which raises  $\Delta P$  and impedes heat transfer. Later, fluid mixes as the diverted fluids meet and enter the main channel with an increased velocity. However, the fluid is not mixed thoroughly due to the inertial forces, and the high-speed fluid is distributed on both sides of the main channel. Along the flow direction, bifurcations continuously interrupt the thermal boundary layer, which enhances the fluid mixing and, thereby, heat transfer (Yang *et al.* 2019; Alfaryjat *et al.* 2014).

Fig. 3.7 shows the pressure contours across the mid-plane of cold plates with different channel designs at a constant  $\dot{m}_w$  of  $0.002 \text{ kg s}^{-1}$ . When no coolant is supplied to the cold plate, the pressure in all channels equals the pressure at the outlet. During the initial phases,

the coolant flows into the cold plate but does not instantly flow through all the channels. Subsequently, the entrance pressure rises dramatically while the exit pressure remains constant, considerably increasing the  $\Delta P$ . As a result of the coolant's extension of the flow path, the contact area between the coolant and the channel surface increases, contributing to lower flow resistance. Due to this, the  $\Delta P$  reduction is rapid. Eventually, the  $\Delta P$  is stable once all the channels are filled with coolant.

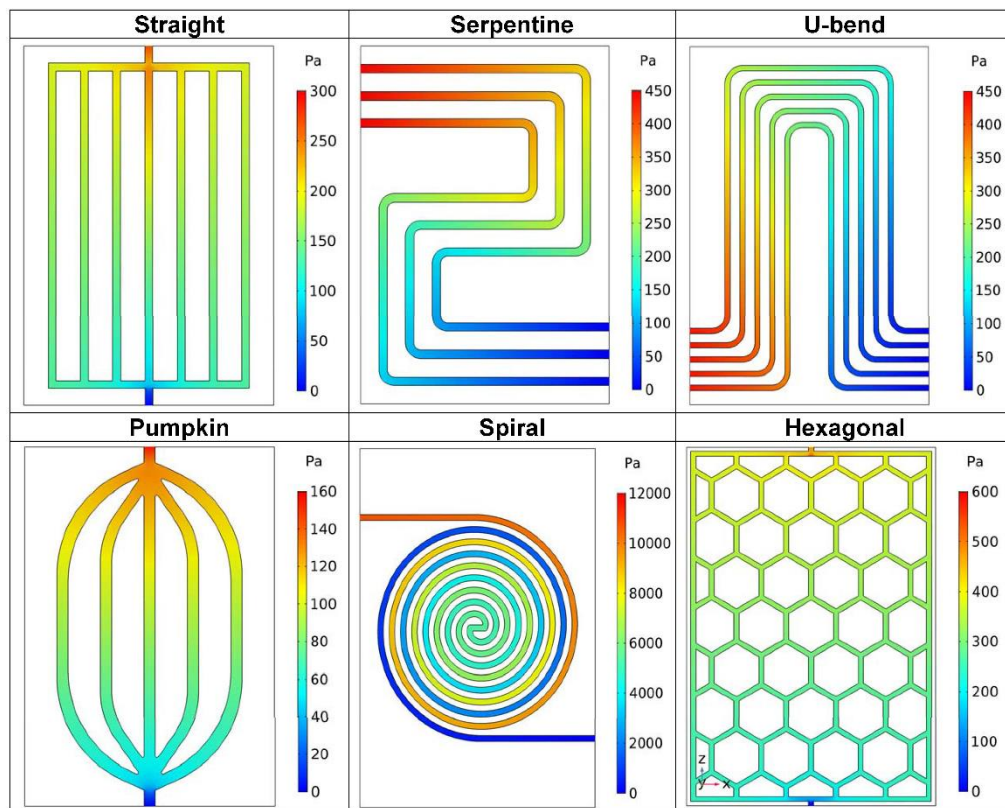


Fig. 3.7: Pressure contours at the mid-profile plane of different channel designs for a  $\dot{m}_w$  of  $0.002 \text{ kg s}^{-1}$

For a constant flow volume, the  $\Delta P$  in pumpkin design is lower, ranging  $150.76 \text{ Pa}$  when compared to all other models due to the presence of broader channels and smooth bends. In serpentine and U-bend models, pressurization of the fluid takes place at the outer side after entering the curved region. Due to this pressure difference, the velocity of the low-speed fluid in the boundary layer may converge to zero or even to negative. Consequently,

this portion of fluid flows in the opposite direction, contributing to a boundary layer separation and vortices formation, which leads to a loss in pressure (Yang *et al.* 2005). Alongside, there is an excess loss in pressure due to the secondary swirl flow caused by the centrifugal effect of a bent-shaped pipe (E Jiaqiang *et al.* 2018). Due to these resemblances in fluid flow characteristics, serpentine and U-bend designs exhibit nearly identical  $\Delta P$  values of 448.93 Pa and 433.83 Pa, respectively. Compared to all other designs, the  $\Delta P$  spiral channel design is noticed to be higher up to 10599 Pa. This is because of the following factors— a) it is a single curved tube to form a spiral shape, unlike other designs which have multiple channel structures; b) at the central region of spiral design, the fluid changes its direction to outlet turn, a pressure difference occurs as a consequence of energy loss due to friction. This results in immense pressure loss along the flow path.

On the other hand, in a hexagonal design, bifurcated channels increase the flow resistance, resulting in a rise of  $\Delta P$  to about 534.23 Pa (Mishra and Gupta 1979). Whereas for straight channel design, high-pressure regions are observed after the entry point and along the central channel, lower pressure regions increase along with the coolant flow and width directions. As the number of channels in straight design is more,  $\Delta P$  rises to about 265.71 Pa despite an enhancement in surface area. This phenomenon occurs due to the uneven distribution of fluid among the channels. Besides this, when the fluid takes a diversion around sharp corners, there is an excess loss in pressure due to flow resistance (Qian *et al.* 2016). However, it is noticed that  $\Delta P$  in pumpkin and straight channel designs, it is 1.6 to 2.9 times lower than that of serpentine and U-bend models due to the absence of secondary flows.



Five different points are selected to evaluate the change in local temperature across the mid-battery surface for different channel profiles (Fig. 3.8). The coolant velocity directly impacts cooling effectiveness. As inferred from Fig. 3.8, a trend in which battery surface temperature varies following the cooling plate design. The region of the battery near the location of the channel inlet experiences lower temperatures. In contrast, higher temperatures are seen near the outlet area for all considered designs. This occurs as the coolant continuously absorbs the heat produced by the battery in the direction of flow throughout the discharge process. This raises the temperature and thereby decreases the cooling capability of the coolant as it reaches the outlet region.

Comparatively, the spiral design exhibits more inhomogeneous distribution with a maximum temperature deviation across the battery surface. Point 3, near the central zone, experiences  $T_{\max}$  of 30.76 °C. At the same time, high heat regions are observed at points 2, 4, and 5 with  $T_{\max}$  of 30.69 °C, 31.81 °C, and 31.52 °C, respectively, due to a shortage of cooling in those particular locations. Besides this, in a spiral design, as the inlet and outlet turns are adjacent, coolant repeatedly comes into contact with the same heat generation area. Hence, the coolant temperature increases along the flow direction, gaining additional heat. Despite cooling the battery, this design adds extra heat to the battery module, reducing overall performance. For the aforementioned reasons, a significant portion of the battery module's surface area is experiencing hot spots. On the contrary, multi-channelled and single inlet and outlet designs have constant heat propagation across the channel length and width. However, it can be noted that inhomogeneous distribution and hot spots with  $T_{\max}$  of 31.81 °C can be a downside of this design.

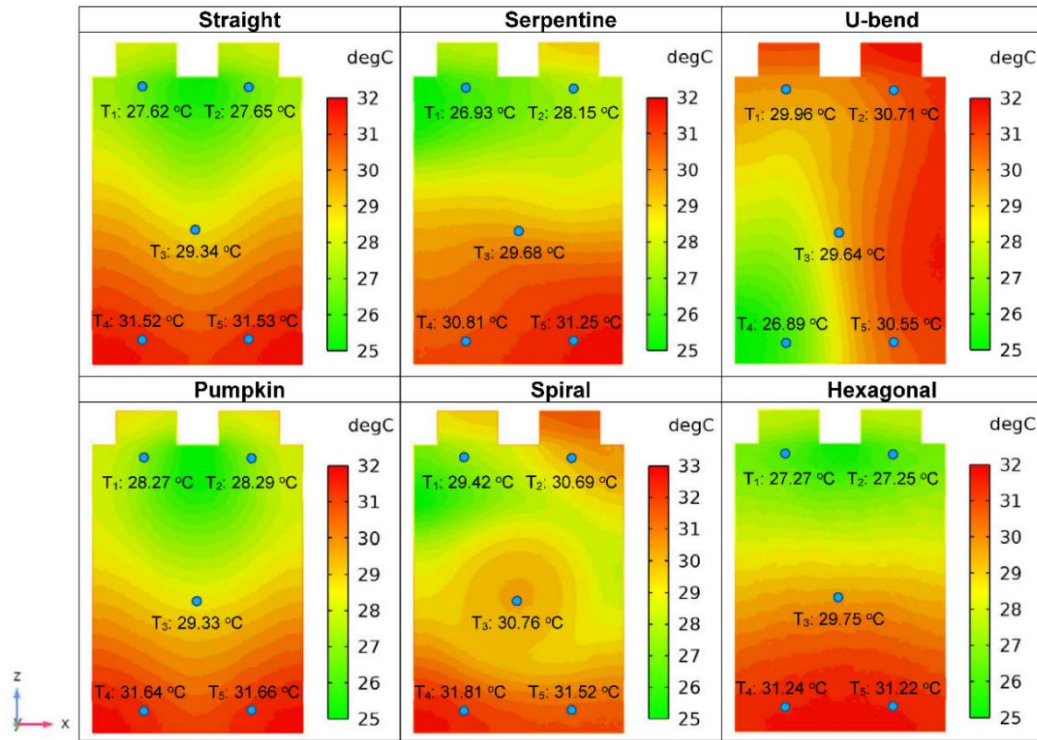


Fig. 3.8: Temperature profile across the surface of battery 2 with various channel designs for a  $\dot{m}_w$  of 0.002 kg s<sup>-1</sup>

For the U-bend design, hot spots are seen at points 2 and 5 of the battery surfaces, and the corresponding  $T_{\max}$  is 30.71 °C and 30.55 °C, respectively. The hotspots are observed to increase along channel length as the fluid velocity reduces in the flowing direction along the short radius curved bends by the end of the discharge process. The straight design reports a  $T_{\max}$  of 31.53 °C at point 6, which is nearer to the outlet region. Similarly,  $T_{\max}$  is found 31.66 °C at point 6 for the pumpkin design. On closer inspection, it is clear from Fig. 3.8 that the serpentine and hexagonal-shaped designs experience relatively fewer hot spots when compared to other designs with  $T_{\max}$  of 31.25 °C and 31.22 °C at point 6, respectively. Therefore, these results indicate that serpentine and hexagonal designs are suitable for maintaining better temperature uniformity for a  $\dot{m}_w$  maintained at 0.002 kg s<sup>-1</sup>. However, the above results may vary with the increase of  $\dot{m}_w$ . Hence,  $\dot{m}_w$  has become a further point

of attention in the present study as it directly impacts the convective heat transfer and energy consumption. In the forthcoming sections,  $\dot{m}_w$  is varied to study the influence of different channel designs on the battery module's thermal behaviour considering several performance indices.

### 3.3.2 Influence of mass flow rate on channel configuration

#### *Pressure Drop*

The present study explores the effect of five different  $\dot{m}_w$  such as 0.001, 0.002, 0.003, 0.004, and 0.005 kg s<sup>-1</sup>. Table 3.8 reveals the quantitative values for pressure drop,  $\Delta P$  across each channel design and are seen to vary proportionally with an increase of  $\dot{m}_w$ . However, a non-linear correlation exists between  $\Delta P$  and  $\dot{m}_w$  in serpentine, U-bend and spiral flow fields which can be attributed to the secondary losses caused by their curved bends. Comparatively, the cold plate with pumpkin structure has the lowest  $\Delta P$  penalty for the same  $\dot{m}_w$ , owing to a broader channel and smooth curve bends of large radius. This phenomenon can also be visualized in the pressure distribution diagram (Fig. 3.7), which shows the impact of flow on different channel profiles.

For a constant  $\dot{m}_w$  of 0.005 kg s<sup>-1</sup>, the  $\Delta P$  in the pumpkin model is noticed to be 441.4 Pa. In the case of the straight channel,  $\Delta P$  increases by 952.1 Pa as the  $\dot{m}_w$  varies from 0.001 kg s<sup>-1</sup> to 0.005 kg s<sup>-1</sup>. This is mainly due to the inverse relation of channel length and  $\dot{m}_w$  with the number of parallel flow paths. The  $\Delta P$  in hexagonal structure is found to be 1872.72 Pa more than the pumpkin design for a  $\dot{m}_w$  of 0.005 kg s<sup>-1</sup>. Whereas for serpentine and U-bend designs,  $\Delta P$  increases with  $\dot{m}_w$  due to the formation of vortices around their

short radius curved bends contributing to secondary flows (Yang *et al.* 2005). Among all, the spiral design requires a high  $\Delta P$  of 31999.99 Pa at a  $\dot{m}_w$  of 0.005 kg s<sup>-1</sup> to propel the flow. This can be attributed to the dominance of centrifugal forces with an increase in  $\dot{m}_w$ . Thus, the influence of both the viscous and centrifugal forces on inertial forces should be attenuated, resulting in a colossal pressure loss along the flow path of the curved region. Upon overall comparison,  $\Delta P$  is found to be lower with pumpkin design followed by serpentine, straight, U-bend, hexagonal, and spiral channels. One important observation that can be built from the above conclusion is that the  $\Delta P$  is much higher with single bent tube design compared to flow separating channels since the coolant is required to flow through longer passages.

Table 3.8:  $\Delta P$  across the inlet and outlet of cooling plate with different channel designs for varying  $\dot{m}_w$

$\dot{m}_w$ (kg s <sup>-1</sup> )	$\Delta P$ (Pa)					
	Straight	Serpentine	U-bend	Pumpkin	Spiral	Hexagonal
0.001	117.4	215.9	207.9	69.0	4829.9	201.1
0.002	265.7	448.9	433.8	150.8	10599.9	534.2
0.003	434.9	690.9	668.8	241.4	17099.9	999.4
0.004	635.6	942.8	909.7	338.9	23999.9	1578
0.005	876.1	1200	1160	441.4	31999.9	2314

Keeping the  $\Delta P$  at a minimum interest in reducing the operational cost of BTMS, further analysis is conducted to identify a good channel design that can maintain a low-temperature difference and uniform distribution.

### *j/f factor*

A non-dimensional *j/f* factor is essential for determining the cooling effectiveness by considering the average Nusselt number (*Nu*) and flow resistance (*f*). A higher *j/f* value indicates a large frontal area relative to the heat transfer and  $\Delta P$ .

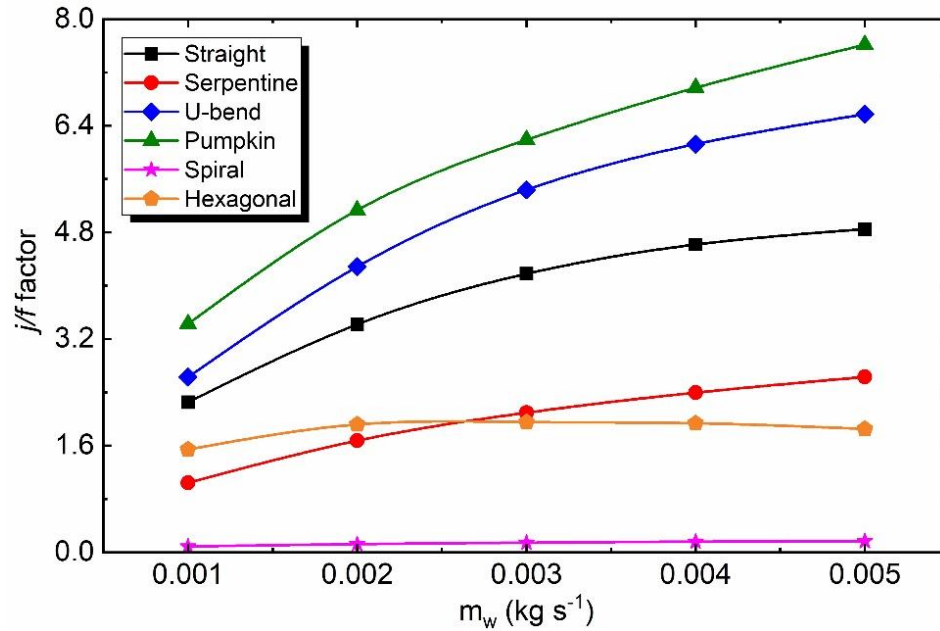


Fig. 3.9: Influence of  $\dot{m}_w$  on  $j/f$  factor for various channel designs.

For the same conditions and a constant flow volume, the pumpkin design shows a significantly higher  $j/f$  factor since it has a broader channel width of 7.1 mm and smooth bends (Fig. 3.9). Whereas the spiral design shows a lower  $j/f$  factor, indicating its lower cooling efficiency. It can be understood from the findings that the change in velocity direction along the flow path across the large curved bends of spiral design tends to a significant increase in  $f$  value. Also, due to a sudden change in the direction of flow at the central region of a spiral design, vortices are induced, leading to a sudden rise in  $f$  value. Compared to the U-bend design, the serpentine model shows a 2.5 times lower  $j/f$  factor for a  $\dot{m}_w$  fixed to 0.005 kg s<sup>-1</sup>, despite vortices along the flow path through the curved bends in both the structures. Besides this, the straight and hexagonal designs exhibit 1.6- and 4-times lower  $j/f$  factor than the pumpkin design, respectively. This can be ascribed to the following factors (i) flow diversion along sharp corners induces  $f$  in case of straight channel design (Qian *et al.* 2016), (ii) whereas, for hexagonal design, the  $f$  value increases

due to the obstruction of flow movement caused by bifurcations in the flowing direction (Yang *et al.* 2019). Hence, it can be affirmed that a 5-channelled cold plate with a pumpkin design can control flow resistance effectively and provide a higher  $j/f$  value when compared to all other typical plate models.

### *Average surface temperature across the battery module*

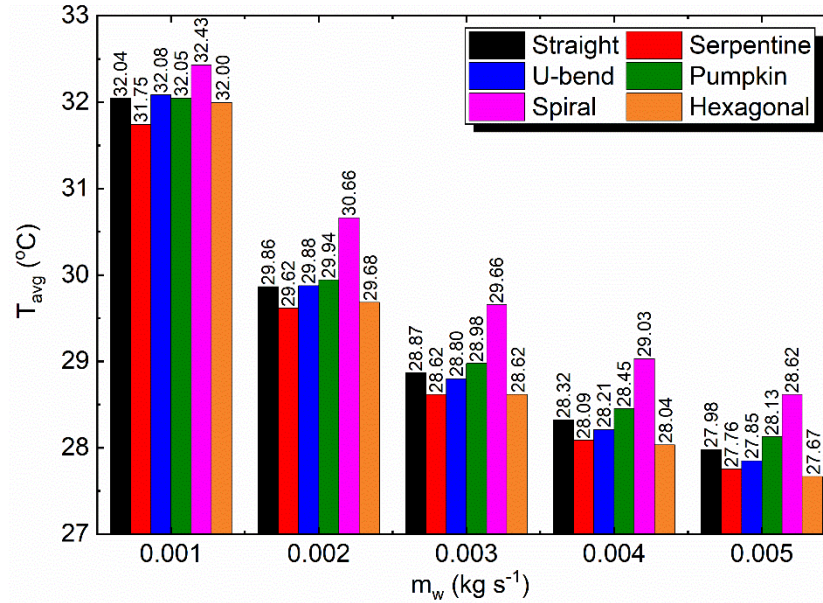


Fig. 3.10: Influence of  $\dot{m}_w$  on  $T_{avg}$  across the battery module for various channel designs.

Fig. 3.10 exhibits that an increase in the  $\dot{m}_w$  reduces the average temperature of the battery module,  $T_{avg}$  significantly for all channel designs, as anticipated. Interestingly, few channel designs perform differently at lower and higher  $\dot{m}_w$ . The hexagonal structure shows a slightly higher  $T_{avg}$  of 0.25 °C than the serpentine design for a lower  $\dot{m}_w$  of 0.001 kg s<sup>-1</sup>. However, with the increase in  $\dot{m}_w$  to 0.005 kg s<sup>-1</sup>, serpentine and hexagonal designs exhibit a similar  $T_{avg}$  of 27.75 °C and 27.66 °C, respectively. Analogous to the above two models, straight channel design reduces  $T_{avg}$  to 28.32 °C and 27.98 °C for a  $\dot{m}_w$  of 0.004 kg s<sup>-1</sup> and 0.005 kg s<sup>-1</sup>, respectively. This indicates that a straight-channelled cold plate can also

provide effective cooling at higher  $\dot{m}_w$ . At a  $\dot{m}_w$  of  $0.005 \text{ kg s}^{-1}$ , the  $T_{avg}$  attained by serpentine and hexagonal design is  $0.46^\circ\text{C}$  and  $0.37^\circ\text{C}$  lower than pumpkin channel design, respectively. Comparatively, the spiral design shows a maximum rise in  $T_{avg}$  for all  $\dot{m}_w$ . For instance, at a  $\dot{m}_w$  of  $0.005 \text{ kg s}^{-1}$ , the  $T_{avg}$  achieved by spiral design is  $0.86^\circ\text{C}$  and  $0.95^\circ\text{C}$  higher than serpentine and hexagonal designs, respectively. These results specify that the serpentine and hexagonal designs can effectively reduce  $T_{avg}$  across the module.

### ***Cooling performance factor***

To further assess the effectiveness of heat transfer per unit pumping power of all typical plate models, a cooling performance factor,  $\beta$ , is considered. A greater  $\beta$  value indicates that the cooling performance is more energy-effective. Fig. 3.11 exhibits the variation in  $\beta$  value for varying  $\dot{m}_w$  of all designs. At lower  $\dot{m}_w$ , the difference in  $\beta$  value with different cooling channel designs is as high as  $10^5$ , whereas at higher  $\dot{m}_w$ , for instance, at  $0.005 \text{ kg s}^{-1}$ , the  $\beta$  value reaches around 441.7 in the case of spiral design. On the other hand, the  $\beta$  value is reasonably large enough for all other considered designs.

It can also be noticed that  $\beta$  value decreases with an increase in  $\dot{m}_w$  for all the designs (Fig. 3.11). These results indicate that the cooling efficiency decreases to a greater extent on a further increase of coolant  $\dot{m}_w$ , which may not be preferable in real-time applications. On the contrary, results show that better efficiency can be achieved even at a lower  $\dot{m}_w$  range, indicating that the cooling effect can still be considered. For all  $\dot{m}_w$ , the spiral design exhibits a lower  $\beta$  value, implying a lower cooling efficiency. This is due to its higher  $\Delta P$  leading to a significant  $P_{pump}$  requirement. On the other hand, the serpentine, hexagonal,

and U-bend designs achieve a higher  $\beta$  value at all flow rates compared to the spiral design. For all  $\dot{m}_w$ , it is noticed that the cooling plate with pumpkin channel design achieves the highest  $\beta$  value. For instance, at a  $\dot{m}_w$  of  $0.005 \text{ kg s}^{-1}$ , the pumpkin design shows significant cooling followed by hexagonal (83.2%), serpentine (66.5%), U-bend (66.2%), and straight (46.4%) channel designs for the same input conditions. Hence, it can be deduced that the pumpkin design is more effective to use for battery cooling as it has low pumping power. However, on a comparative scale, this particular design offers slightly lower temperature uniformity than other flow fields at high  $\dot{m}_w$  conditions.

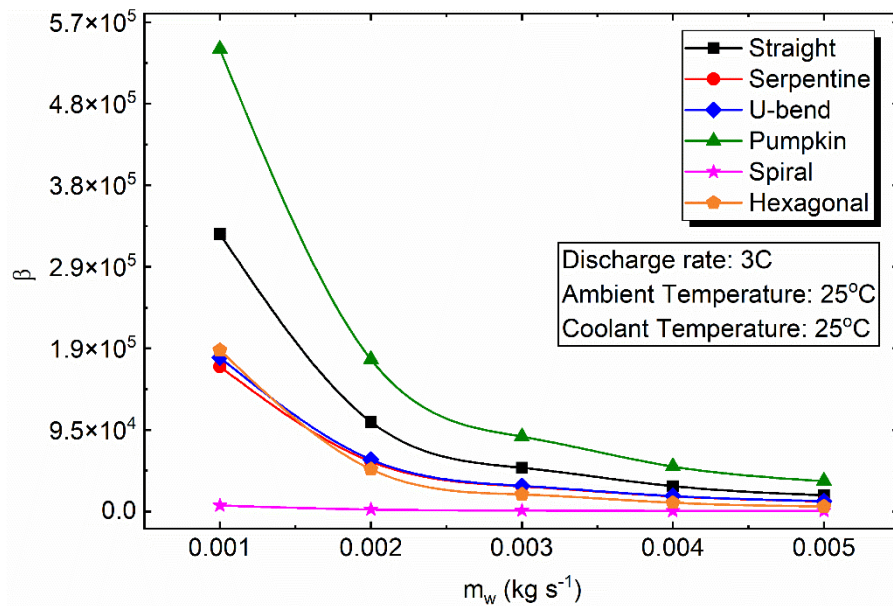


Fig. 3.11: Influence of  $\dot{m}_w$  on  $\beta$  for various channel designs

Hence, while designing a cold plate, a trade-off must be maintained between temperature reduction and  $\Delta P$  for higher  $\dot{m}_w$  applications. If thermal performance is of profound interest and energy consumption is not an issue, e.g., for automotive applications, in that case, one can consider serpentine and hexagonal designs for the cold plate after further design



modification. However, if  $\Delta P$  and  $P_{pump}$  are the significant constraints, the pumpkin channel design can be employed as a cold plate.

### 3.3.3 Effect of ambient temperature on cooling effectiveness

In real-time, batteries working under higher operating conditions are sensitive to temperature. A slight difference in temperature for a shorter period may cause faster exothermic reactions and heat accumulation in a cell (Kim *et al.* 2019). Hence, to analyze the cooling proficiency of different channel designs more comprehensively the ambient temperature,  $T_a$ , is varied from 25 °C to 45 °C at a constant  $\dot{m}_w$  of 0.003 kg s<sup>-1</sup> and the results are shown in Fig. 3.12. For this, the  $T_{w,in}$  is maintained at 25 °C, and discharge rate is fixed to 3C.

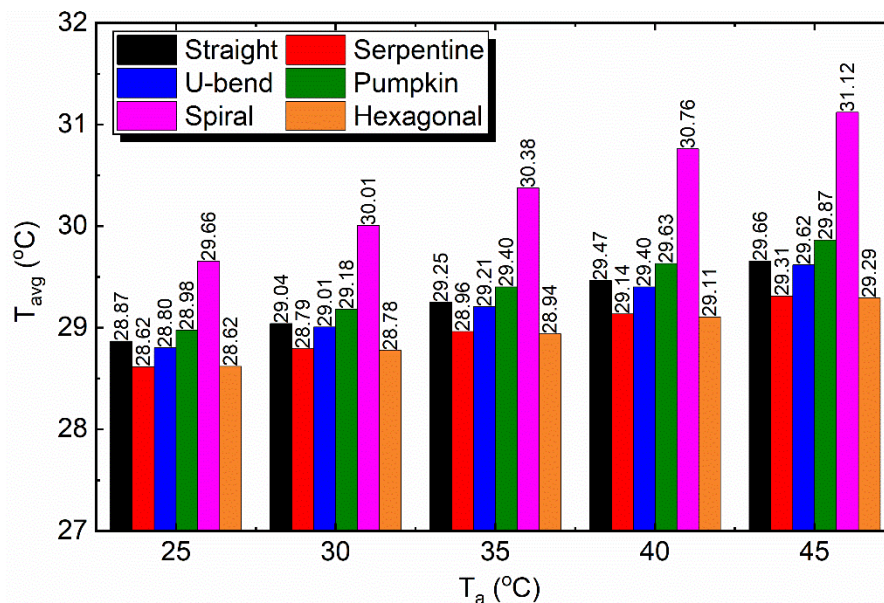


Fig. 3.12: Influence of  $\dot{m}_w$  on the cooling effectiveness of various channel designs

It is apparent from Fig. 3.12 that a difference in temperature rise is seen with each design depending on its fluid flow arrangement. As the  $T_a$  increases from 25 °C to 45 °C, serpentine and hexagonal designs show a lower rise in  $T_{avg}$  by a value of 0.69 °C and 0.67 °C, respectively. At the same time, a significant change in  $T_{avg}$  is seen with spiral design as the  $T_a$  rises. For instance, at  $T_a$  of 25 °C, the spiral design achieves a  $T_{avg}$  of 29.66 °C, with an increase of  $T_a$  to 45 °C, the  $T_{avg}$  reaches to around 31.12 °C. This phenomenon is mainly due to the heat transfer between warm and fresh fluid passages that are adjacent to each other. Although the pumpkin design shows a more significant cooling performance factor  $\beta$ , it is evident that the  $T_{avg}$  is considerably higher than other channel profiles except for spiral design. For a  $T_a$  of 45 °C, the  $T_{avg}$  achieved by pumpkin design is 0.55 °C and 0.57 °C higher than that of serpentine and hexagonal designs, respectively. Similarly, the straight channel design shows a  $T_{avg}$  of 0.34 °C and 0.36 °C more than the serpentine and hexagonal designs, respectively. However, the U-bend design shows notably lower  $T_{avg}$  than the pumpkin and straight channel designs for  $T_a$  ranging from 25 °C to 45 °C.

It can be noticed from Fig. 3.14 that the temperature distribution of battery 2 is seen to vary with the profile of each cooling channel design for all the locations along the z- and x- directions. On the other hand, as seen in Fig. 3.13, regardless of cooling design, the temperature is inhomogeneous through the cell thickness direction. The variation along battery 1 is not considered as it is exposed to heat flux conditions and is enclosed by a single cold plate, experiencing a higher temperature gradient and more non-uniformity, unlike battery 2, surrounded by two cold plates. Generally, the battery part near the cold

plate inlet experiences a lower temperature than the part near the outlet, which varies with the channel design, as shown in Fig. 3.14. The temperature profile results from variations in coolant temperature over the discharge phase (Fig. 3.13). In most cases of Fig. 3.14, the hot spots on the battery emerge at regions near the positive and negative tabs.

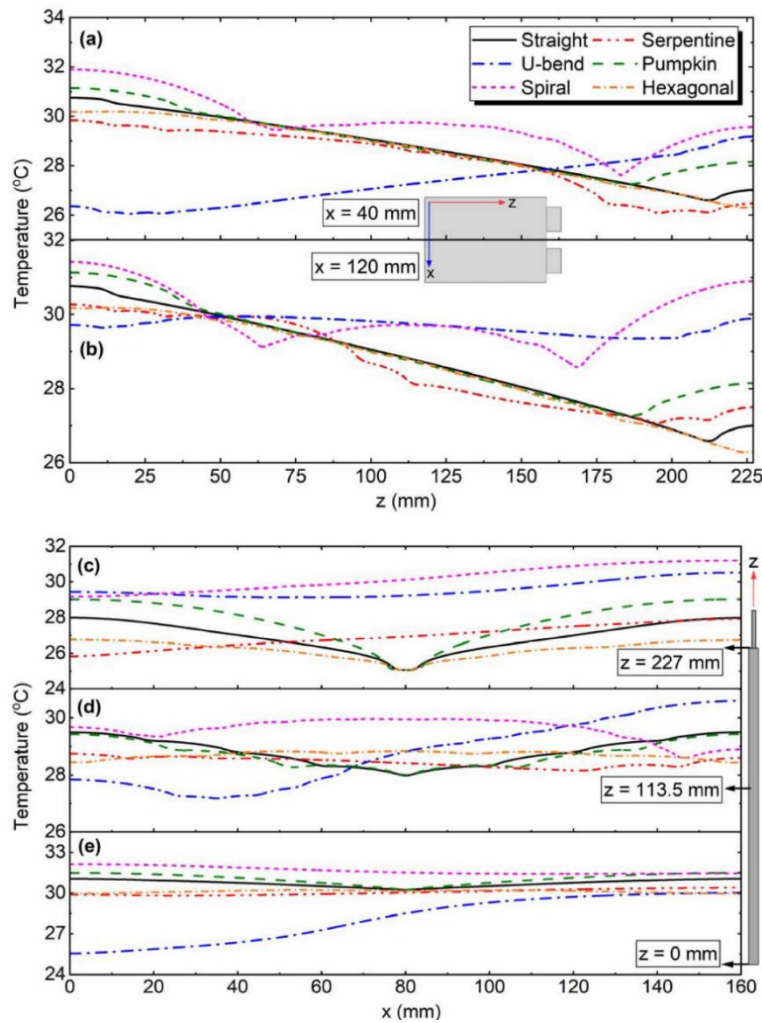


Fig. 3.13: Temperature profile across the surface of battery 2 ( $y = 9.25$  mm) for a  $T_a$  of  $35$  °C along the (a, b)  $z$ -direction for different  $x$  locations, and (c, d, e)  $x$ -direction for different  $z$  locations

In parallel, the temperature rise can be seen in Fig. 3.13 (a, b) at  $z = 0$  to  $25$  mm and (c) at  $x = 0$  to  $20$  mm and  $140$  to  $160$  mm locations. Also, at the bottom region, as seen in Fig. 3.14 (a, b) at  $z = 175$  to  $225$  mm and (e) at  $x = 0$  to  $40$  mm locations along the  $z$ - and  $x$ -directions, respectively. This can be attributed to the combined effect of heat generation

and coolant flowing sequence over the cold plate, as shown in Fig. 3.14. For instance, in the case of the pumpkin channel design, the battery experiences lesser temperature near the tab region as it is close to the cold plate inlet, whereas hot spots are seen on the lower part of the battery near the cold plate's downstream side. On the other hand, in the U-bend design, hot spots are near the upper right corner and tab region of the battery. In contrast, the cooling effect is more on the battery region at the lower left corner as the inlet is positioned on that side (Fig. 3.14). The same effect can be seen reflected in the results of Fig. 3.13. Based on the results, it can be said that hexagonal and serpentine designs effectively cool and reduce the hot spots across the battery module.

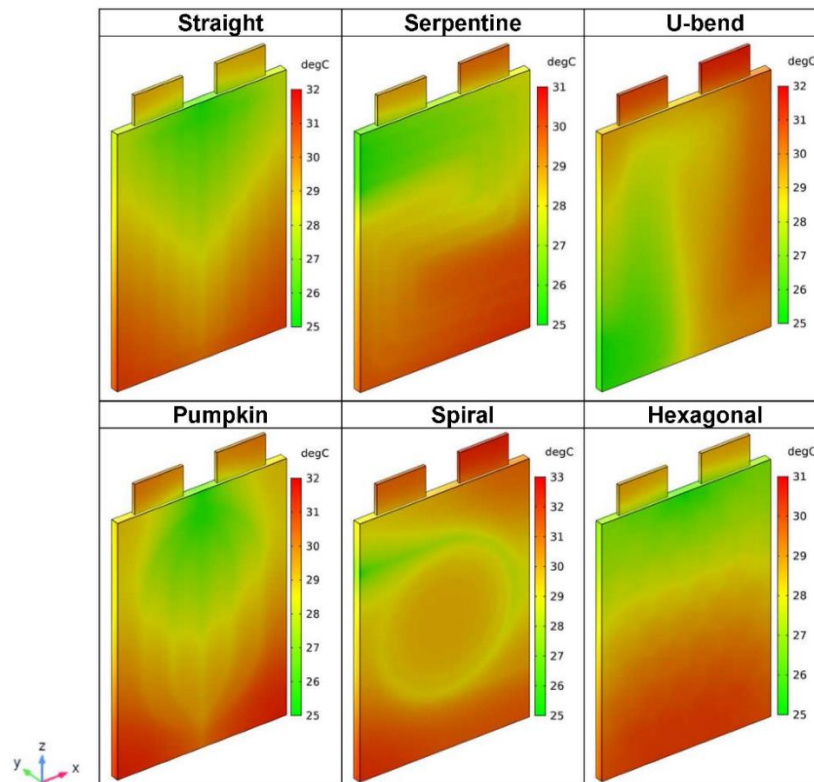


Fig. 3.14: Temperature distribution across the battery 2 with various channel designs for a  $T_a$  of 35 °C

### 3.3.4 Real-time performance investigation with a standard drive cycle data

In this section, one of the optimal designs obtained from the above comprehensive analysis, i.e., the hexagonal design, is chosen and subjected to a global US06 (highway) driving cycle to assess the actual performance during the on-road driving conditions. The current and voltage profiles for a 600s-long US06 drive cycle with aggressive driving behaviour are shown in Fig. 3.15. A  $\dot{m}_w$  of  $0.003 \text{ kg s}^{-1}$  is selected for the transient study, whereas  $T_a$  and  $T_{w,in}$  are maintained at  $35 \text{ }^\circ\text{C}$  and  $25 \text{ }^\circ\text{C}$ , respectively.

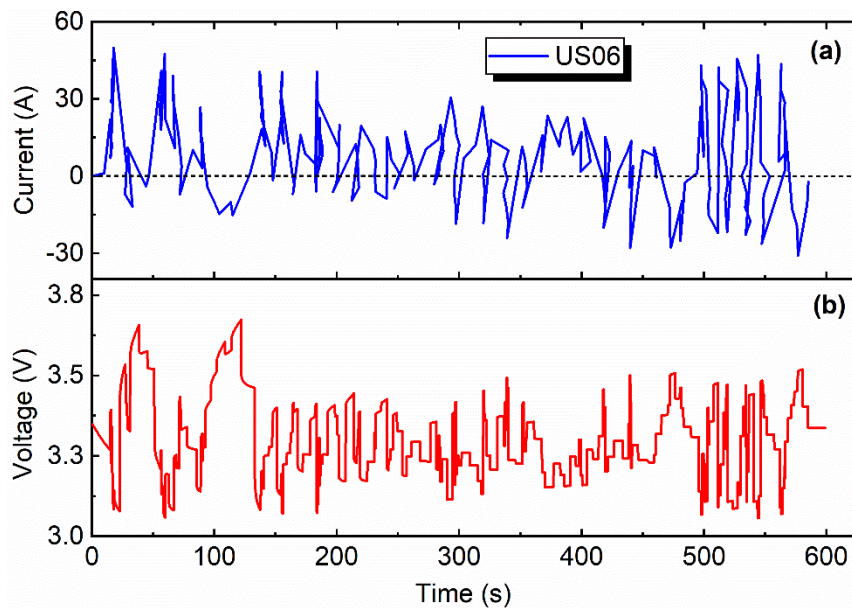


Fig. 3.15: (a) Current profile of US06 high way driving cycle ('+ sign' represents charging and '- sign' represents discharging) (b) Voltage distribution under US06 drive cycle

Five different points across the mid-battery surface for a battery module with a hexagonal-shaped cold plate design are selected to analyze the local thermal behaviour under realistic driving conditions. The temperature curve of each point across the surface of battery 2 is shown in Fig. 3.16.

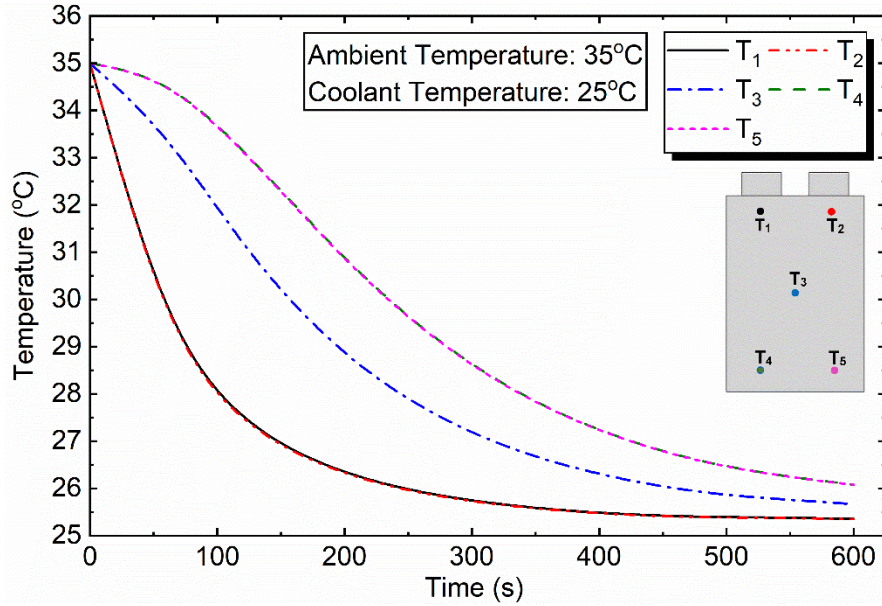


Fig. 3.16: Variation of local temperature across the surface of battery 2 integrated with hexagonal channel cold plate under US06 drive cycle.

The significant and rapid changes in the charge and discharge rates of the US06 cycle contributed to fluctuations in  $T_{\max}$ . It can be noted that even at an extreme temperature of 35 °C with high charge or discharge currents, the proposed liquid cooling system assists the battery temperature in reaching the pre-set standard within a permissible time of 600s. In the early stages of cooling up to 60s, the temperature difference between all points is significant owing to coolant flow time and heat transfer inactivity. Later, in the final stages, i.e., after 450s, the system progressively stabilized. At point 3, near the central portion of the battery,  $T_{\max}$  reduces by 9.33 °C as the flow time reaches an end of 600s. Besides this, the maximum deviation between point 1 and point 5 is noticed to be 5.85 °C and 0.72 °C during the initial 120s and final 600s of flow, respectively. These fluctuations in the battery temperature at different locations are mainly due to the profile of the cooling channel. For instance, points 1 and 2 exhibit a relatively same temperature near the inlet region. A similar trend is seen with the points 4 and 5 near the outlet. Besides this, as the flow

duration approaches 600s, the overall variation of local temperature distribution is stabilized. These results specify that the hexagonal design could maintain the temperature distribution across the battery module under dynamic conditions and also within a safe range.

### 3.4 Summary

Six distinct channel profiles, namely, serpentine, U-bend, straight, pumpkin, spiral, and hexagonal, are evaluated numerically for cooling a large-capacity battery module with varying  $\dot{m}_w$  and fixed discharge rate of 3C. Also, simulations are conducted for different ambient temperatures to evaluate their performance under unfavorable conditions. In addition, realistic drive cycle data is utilized to test the performance of an optimal design.

The conclusions drawn from the above investigation are summarized below:

- The channel profile significantly influences the hydro-thermal performance of a cold plate besides operating parameters. The flow-splitting channels exhibit better uniformity and heat transfer performance than a spiral channel for a fixed flow volume.
- The  $\Delta P$  and  $j/f$  factor of the pumpkin channel design is the least and most significant, respectively, compared to all other designs, indicating a greater cooling efficiency.
- Despite the higher  $\Delta P$ , for all  $\dot{m}_w$ , serpentine and hexagonal designs show a lower  $T_{avg}$ , as the  $\dot{m}_w$  exceeds  $0.003 \text{ kg s}^{-1}$ .
- Spiral design exhibits the largest  $\Delta P$  and  $T_{avg}$  with lowest  $j/f$  factor and  $\beta$  value of all the six flow fields considered, indicating poor cooling performance.

- Pumpkin design exhibits an excellent value of  $\beta$  followed by hexagonal, serpentine, U-bend, and straight channel configurations for all  $\dot{m}_w$  conditions.
- All the channel designs maintained the  $T_{avg}$  within a permissible limit i.e.  $< 40\text{ }^\circ\text{C}$  under different ambient conditions for a  $T_{w,in}$  of  $25\text{ }^\circ\text{C}$  and  $\dot{m}_w$  of  $0.003\text{ kg s}^{-1}$ .



# Chapter 4

## Optimize the Sizing and Rating Parameters of The Ideal Cold Plate Through Surrogate Models and NSGA II

**Keywords**  
Battery Thermal management;  
Electro-thermal model;  
Hexagonal design;  
Optimization;  
NSGA II

*This chapter provides a detailed exploration of Latin hypercube sampling, surrogate models and multi-objective optimization techniques for augmenting the performance of a hexagonal cooling plate design used in regulating the temperature of Li-ion batteries. To begin with, a systematic comparison of surrogate models, including Multi linear regression, Response surface approximation, Support vector machine and Kriging model, is conducted in search of the best one. Later, the study delves into the domain of multi-objective optimization by employing non-dominated sorting genetic algorithm II. Additional to the optimization-driven enhancements, Shapley Additive explanation techniques is employed to interpret the Kriging model, unravelling the design and operating variable's impact on the objective functions.*

### 4.1 Introduction

In the previous chapter, hexagonal and serpentine designs are found to be best if thermal performance is of major interest, while pumpkin design could be a good choice for obtaining an excellent hydraulic performance. However, an optimized channel design that simultaneously minimizes maximum temperature, temperature deviation and energy consumption is more beneficial in real-world applications. Balancing all these functions is critical in achieving cost-effectiveness and optimal thermal performance. Thus, to compromise this conflict, multi-objective optimization is essential. A typical optimization workflow combines machine learning (ML) models with multi-objective genetic algorithms (MOGA). Currently, most studies employ the response surface method (RSM)

and non-dominated sorting genetic algorithm II (NSGA-II) for optimizing the channel design. Here, multi-objective analysis establishes a relation between the input variables and the output functions, built on a preliminary set of numerical results. These solutions give decision-makers various possibilities, allowing flexibility in meeting specific requirements or preferences. (Deng *et al.* 2019; Chen *et al.* 2019; Liu and Zhang 2019; Li *et al.* 2022) followed the analogous methodology with maximum temperature, temperature deviation and pressure drop as the key objectives. The effectiveness of NSGA-II is demonstrated in these examples of finding optimal solutions for BTMS, where one needs to consider several objectives and constraints simultaneously. Although few studies ponder this context, it is important to establish a complete system of guidelines for the precision of ML models.

In the current work, an effective battery cooling system is accomplished by optimizing one of the best channel designs (i.e., the hexagonal design) proposed in the previous chapter. The effect of structural parameters such as channel width, branching angle, and side length of the hexagon, as well as operating parameters including mass flow rate and coolant temperature, are considered. The design optimization is based on minimizing maximum temperature and pressure drop along with maximizing heat transfer performance simultaneously. The study commences by employing a Latin hypercube sampling technique to generate a set of points, serving as the basis for conducting simulations using COMSOL Multiphysics 5.4 software. Later, the obtained data is used to test and train with different ML models such as Multi-Linear regression, Support vector machine, Kriging/Gaussian process regression and RSM. An appropriate ML model is selected based on the error analysis and then coupled with NSGA-II. Finally, a K-means clustering

algorithm is employed to attain the best compromise solutions from the Pareto front, which are later used for numerical validation. In addition, the present work also utilizes the SHapley Additive exPlanations (SHAP) technique to make the outcome of an ML model more understandable by visualizing it. The insights obtained through SHAP are noteworthy as it explains the ML model and calculates each feature's contribution to the prediction.

While meeting the goals mentioned above, the current work also shows how liquid cooling systems' design and operating parameters are to be prioritized based on their impact on battery health and energy consumption. For instance, increasing the temperature gradient can accelerate the heat transfer rate from the battery to the coolant by allowing a colder fluid to pass through the mini channels. Alternatively, it can be improved by raising the heat transfer coefficient and elevating the mass flow rate. To decide between these options, evaluating the cooling effectiveness and energy efficiency of each approach is imperative. Increasing the fluid velocity or enlarging the channel cross-sectional area can achieve a higher coolant flow rate. However, pumping a large quantity of liquid over a wider channel area or a small amount of coolant at a high velocity to overcome pressure drop and attain high kinetic energy increases parasitic power consumption. This paper broadly addresses such competitive design aspects by investigating heat transfer and energy efficacy, facilitating better-informed retrofitting options for BTMS.

## 4.2 Problem definition

The present study considers one of the best designs, i.e., the hexagonal design obtained from the previous chapter, as shown in Figs. 3.1 and 3.2. The boundary conditions applied and the assumptions followed are the same as those of Chapter 3, except for the ambient

temperature, which is considered to be 35 °C, to make the study more viable for Indian climate.

## 4.3 Optimization techniques

### 4.3.1 Design variables

Considering the previous studies, channel parameters and inlet conditions displayed a significant role in determining the effectiveness of cold plates (Monika *et al.* 2021). Hence, three geometric parameters, such as the side length of a hexagon ( $L$ ), channel width ( $W_c$ ) and bifurcation angle ( $\theta$ ), are considered as design variables along with operating parameters mass flow rate ( $\dot{m}_w$ ) and coolant temperature ( $T_{w,in}$ ). The cold plate thickness and channel depth are maintained at a constant value considering the unidirectional effect of thermal performance. Table 4.1 lists the design variables range and can be mathematically expressed as:

$$X = [x_1, x_2, x_3, x_4, x_5] = [L, W_c, \theta, \dot{m}_w, T_{w,in}]^T \quad (4.1)$$

Table 4.1: Design variables and bound spaces

Bounds	Design variables				
	$L$ (mm)	$W_c$ (mm)	$\theta$ (°)	$T_{w,in}$ (°C)	$\dot{m}_w$ (kg s <sup>-1</sup> )
LB	15	3	60	25	0.001
UB	19	5	120	35	0.005

The upper bounds are arbitrarily chosen, while the lower bounds are selected so that they do not affect the optimization process. Since the flow structure of the hexagonal design is complex compared to a traditional design, parametric modelling is adopted in CATIA V5 to regulate the user parameters of the geometry. This allows all the other dimensions in the 3D model to alter any of the dimensions. For this, initially, the independent variables, i.e.,

the geometric parameters considered in the present work, are defined. Later, a few relations are created to interlink other design dimensions with the independent variables. For instance, the following formulas are used in the x-direction to regulate:

$$\text{Distance between two hexagons (d): } d = r + \frac{W_c}{2} \quad (4.2)$$

$$\text{Width of the hexagon ( } W = 2 \times r \text{): } r = L \times \cos(90 - (\theta/2)) \quad (4.3)$$

### 4.3.2 Response parameters

- i. The maximum temperature  $T_{\max}$  assesses the cold plate's functioning since it can reveal the battery's worse state.
- ii. An augmentation in fluid flow to facilitate rapid heat dissipation leads to an inevitable rise of  $P_{\text{pump}}$ . Complex channel designs that promote heat transfer exhibit significant pressure drop,  $\Delta P$  resulting in similar implications. As per Darcy-Welsbach law,  $\Delta P$  for the laminar flow is calculated as follows:

$$\Delta P = P_{\text{outlet}} - P_{\text{inlet}} \quad (4.4)$$

- iii. The average heat transfer coefficient ( $\text{W m}^{-2} \text{ } ^\circ\text{C}^{-1}$ ) of liquid coolant serves as a measure to evaluate the heat exchange performance of cold plates is considered, as mentioned in Eq.'s 2.3 and 2.4.

### 4.3.3 Latin hypercube sampling

In general, Latin hypercube sampling (LHS) is employed to generate design points, known as design of experiments (DOE), for the prediction modelling of the objective functions. The present work implements an enhanced stochastic evolutionary algorithm (ESE) proposed by R. Jin *et al.* (2018) optimize the LHS. The algorithm usually comprises inner

and outer loop. An inner loop generates new designs through element exchanges and evaluates their suitability based on acceptance criteria. In contrast, the outer loop regulates the optimization process by modifying the threshold in the acceptance criterion. The threshold value is self-adjusted to match various DOE problems such as space-filling requirements, sample size, etc. Here, the threshold decides whether to accept or reject a new design. For a higher dimensionality problem, the ESE method helps produce optimal sample points with reasonable computational time (Taylor 2013). A total of 160 points are generated by the ESE-LHS method within a decision space limited by the lower and upper bounds, as defined in Table 3.1. This implies that each set of design points abides by the same limit imposed for the optimization process. Later, simulations are conducted to calculate the response parameters. The final data set is subsequently used to train different ML models and is reported in Appendix A.

#### **4.3.4 Surrogate models**

Multi-objective optimization (MOO) using evolutionary algorithms requires numerous calculations of the objective functions for the effective exploration of optimal solutions (Seshadri 2017). In the absence of an appropriate response function, the assessment of these objective functions can become time-consuming and costly. Hence, a surrogate/ML-based approximation is employed to assess the objective-function values, circumventing numerical or experimental costs and saving time. Four ML models are employed in the present work, including Multi-linear regression (MLR), Kriging/Gaussian process regression (GPR), Support vector machine (SVM) and Response surface method (RSM).

All the models are trained on an 80/20 split data set. A standard scalar function is used to standardize the input variables independently during pre-processing.

### ***Multi-linear regression***

MLR is a statistical approach that predicts the outcome of a response variable (dependent) by using several explanatory variables (independent). It aims to build a linear relation between independent and dependent variables and is represented mathematically as,

$$y_i = \beta_0 + \beta_1 x_{i1} + \beta_2 x_{i2} + \dots + \beta_p x_{ip} + e \quad (4.5)$$

where  $y_i$  and  $x_i$  are the dependent and independent variables, respectively;  $\beta_0$  is the  $y$ -intercept, and  $\beta_p$  represents the slope coefficient of independent variables;  $e$  is the error term or residual.

### ***Kriging/Gaussian process regression***

GPR (Søndergaard 2002) is a meta-modelling interpolation approach that uses a trend model,  $F(x)$ , for capturing large-scale variations during a systematic departure,  $Z(x)$ , to identify small-scale variations as:

$$f(x) = F(x) + Z(x) \quad (4.6)$$

Where,  $f(x)$  is the unknown function.  $F(x)$  and  $Z(x)$  represent the global model and localized deviation, respectively.  $Z(x)$  is the realization of a stochastic process with zero mean and non-zero covariance. The trend model uses a linear polynomial function in this approach, while systematic departure terms follow a Gaussian correlation function.

### ***Support vector machine***

SVM (Zhang *et al.* 2003) is a supervised ML algorithm which works best for small data sets but complex ones. It can be used for both classification and regression tasks. The algorithm tries to find the best hyperplane that separates  $n$ -dimensional space into classes,

ensuring an easy replacement of the new data into a correct category in future. The objective function of SVM is given as,

$$\arg \min_w \left\{ \frac{1}{n} \sum_{i=1}^n \max \{0, 1 - y_i f(x_i)\} + C w^T w \right\} \quad (4.7)$$

here,  $w$  and  $C$  are the error term's normalization vector and penalty parameter, respectively.

### ***Response surface method***

RSM (Myers *et al.* 2018) is a method of fitting polynomial functions to discrete responses based on numerical results. A second-order polynomial function is employed as the response function, which is specified by:

$$f(x) = \zeta_0 + \sum_{i=1}^N \zeta_i x_i + \sum_{i=1}^N \zeta_{ii} x_i^2 + \sum_{i < j}^N \zeta_{ij} x_i x_j \quad (4.8)$$

here,  $\zeta_0$  is the intercept;  $\zeta_i$ ,  $\zeta_{ii}$  and  $\zeta_{ij}$  are the linear, second order and quadratic interaction terms, respectively. The metrics adopted to evaluate the prediction accuracy include normalized mean absolute error (NMAE), normalized mean absolute deviation (NMAD), normalized root mean square error (NRMSE) and coefficient of determination ( $R^2$ ), as given by:

$$NMAE = \frac{1}{n} \sum_{i=1}^n \left| \frac{\hat{y}_i - y_i}{y_{\max} - y_{\min}} \right| \quad (4.9)$$

$$NMAD = \frac{1}{n} \sum_{i=1}^n \left| \frac{y_i - \bar{y}_i}{y_{\max} - y_{\min}} \right| \quad (4.10)$$

$$NRMSE = \frac{1}{y_{\max} - y_{\min}} \sqrt{\frac{1}{n} \left[ \sum_{i=1}^n (\hat{y}_i - y_i)^2 \right]} \quad (4.11)$$



$$R^2 = 1 - \frac{\sum_{i=1}^n (y_i - \hat{y}_i)^2}{\sum_{i=1}^n y_i^2} \quad (4.12)$$

Where,  $\hat{y}_i$  and  $y_i$  indicate the predicted and actual values, respectively.  $n$  signifies the number of data points.

### 4.3.5 Hyperparameter tuning

An ML model typically comprises two types of parameters. Model parameters can be initialized and updated during the training process. Conversely, the user must specifically define hyperparameters to control the training process. As a result, they must be set before training an ML model as they define the model structure. Hyperparameters are used to design an ML model (e.g.,  $C$  in SVM) or minimize the algorithm's loss function (e.g., Kernel type in SVM). The process of building an ideal ML model with the best possible combination of hyperparameters is known as hyperparameter tuning (HPT) (Yang and Shami 2020). The selection of hyperparameters determines the behaviour of an ML model. The scoring system (Metrics) is typically chosen as a means of HPT to compare different ML models in the current work. A well-known HPT technique, grid search is utilized to refine the models and metrics for evaluating the testing dataset. The best ML model is then found and used to predict response parameters.

### 4.3.6 Multi-objective optimization

Based on the parametric analysis, a substantial effect on the performance of the cold plate is seen with the change in any of the geometric features. Additionally, there is a possibility of interdependence between these parameters. Hence, obtaining the most favorable

parameter only through parametric analysis is not rational. A dedicated mathematical optimization algorithm is required to acquire the optimal parameter amalgamation.

However, many real-world optimization problems inherently consider multiple objectives that are often conflicting. This implies that improving one objective inevitably leads to the deterioration of the other. Therefore, it is imperative to employ a more comprehensive approach where the objective functions are optimized simultaneously rather than compounding them into a single one. Hence, the present work employs NSGA-II introduced by (Deb *et al.* 2002) in conjunction with the best ML model obtained from the previous sub-section. Here, the optimal solutions obtained from the algorithm are not a single one but a set of non-inferior solutions which is commonly known as Pareto optimal solutions. It is suitable to solve non-linear complex problems, unlike conventional methods.

In practice, seeking the optimal compromise solution is often necessary, even if a non-inferior solution has been found. However, it should be emphasized that each point on the Pareto front always corresponds to a non-inferior solution. Therefore, it is not permissible to arbitrarily choose a point from the front and consider it the optimal solution. In addition, a more significant reduction in the objective function becomes complicated as the problem gets closer to the extreme parts of the Pareto front. This implies that an optimal compromise solution should exist between both endpoints. Given this, a K-means clustering method (Deng *et al.* 2020) is performed to choose the best solutions out of the Pareto front in the context of MOO. The k-means algorithm uses the similarities among the non-dominated solutions in the multi-dimensional objective space to partition them into k clusters. The cluster in the analysis represents a unique and identifiable region comprising optimal

compromise solutions that provide trade-offs between the objectives of the analysis. The representative solutions are the solutions of the cluster, which are the centroid and the mean of all the solutions. The cluster representatives are chosen based on their suitability as the final optimal solutions in the specific application. This methodology helps in decision-making and finds well-distributed solutions for complex MOO problems.

The workflow followed is exhibited in Fig. 4.1. Python 3.12.1 is utilized to carry out the MOO procedure. NSGA II is implemented from the Pymoo 0.6.0 framework (Blank and Deb 2020) to determine optimal Pareto solutions.

The settings followed for MOGA are shown in Table 4.2. The population size,  $N$  of 100, a simulated binary crossover (SBX) crossover with  $\eta_c$  of 0.9 and polynomial mutation (PM) with  $\eta_m$  of 0.15 is applied. The crossover probability is always kept higher than the mutation probability, aiming to balance exploration and exploitation, promoting the efficient convergence toward optimal solutions while preserving diversity within the population. A termination criterion for a maximum of 500 iterations is implemented as a predefined stopping rule, specifying its limit to control computational resources or meet the desired convergence level.

Table 4.2: Settings for MOGA

<b>Parameter</b>	<b>Value</b>
Population size, $N$	100
Crossover probability, $\eta_c$	0.9
Mutation probability, $\eta_m$	0.15
Maximum no. of iterations, $g$	500

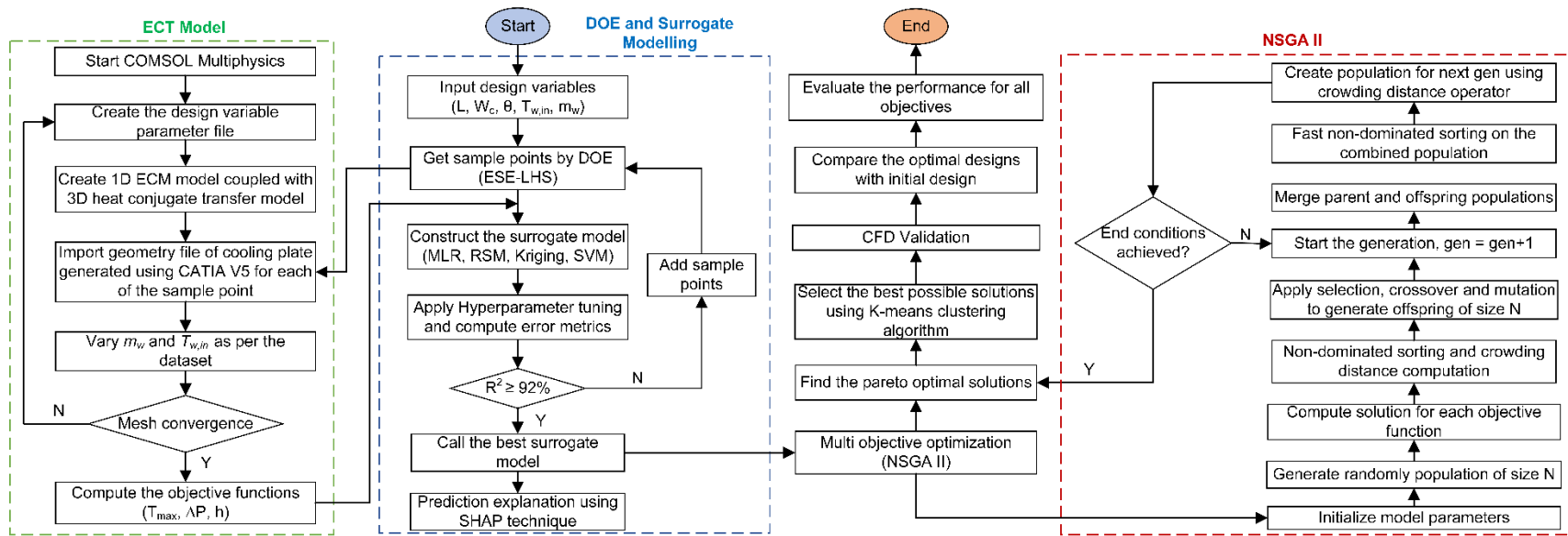


Fig. 4.1: Optimization workflow based on simulations and NSGA-II

The multi-objective problem is formulated as follows:

$$\text{Find } x = \{x_1, x_2, x_3, x_4, x_5\} \quad (4.13)$$

$$f(x) = \{f_1(x), f_2(x), f_3(x)\} \quad (4.14)$$

$$\text{Min} \quad \begin{cases} f_1(x) = T_{\max}(x) \\ f_2(x) = \Delta P(x) \end{cases} \quad (4.15)$$

$$\text{Max} \quad f_3(x) = h(x). \quad (4.16)$$

$$\text{Such that} \quad \begin{cases} g_1 = T_{\max} - 40; g_2 = \Delta P - 650 \\ g_3 = x_4 - 0.003 \\ 15 \leq x_1 \leq 19; 3 \leq x_2 \leq 5 \\ 60 \leq x_3 \leq 120; 0.001 \leq x_4 \leq 0.005 \\ 25 \leq x_5 \leq 35 \end{cases} \quad (4.17)$$

## 4.4 Results and discussion

### 4.4.1 Grid convergence

The computational domain is discretized using a free tetrahedral mesh with different size constraints, as shown in Fig. 4.2. One of the test cases is described in the current work, and the corresponding grid independence results are reported in Table 4.3.

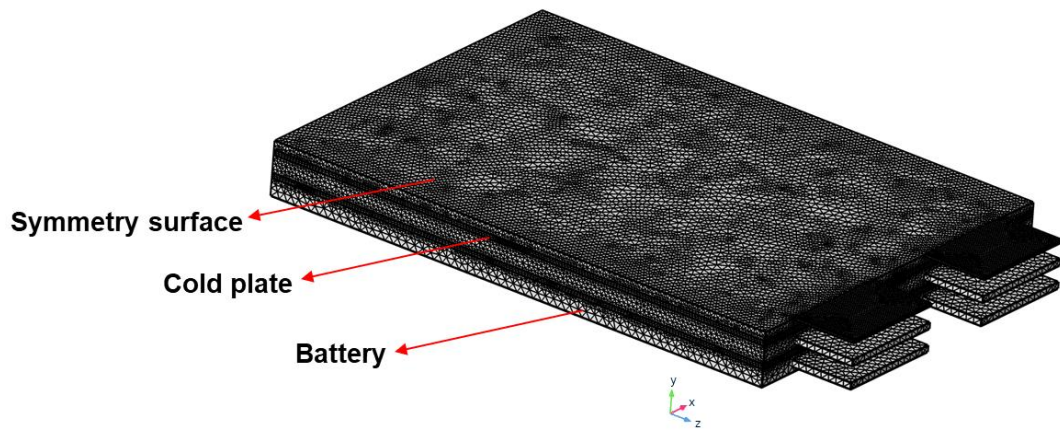


Fig. 4.2: Mesh model of the computational domain

Four grid schemes with different number of nodes ranging from  $3.3 \times 10^6$ ,  $5.8 \times 10^6$ ,  $7.5 \times 10^6$  and  $8 \times 10^6$  are used to conduct the mesh independence test with  $\dot{m}_w = 0.003 \text{ kg s}^{-1}$ ,  $W_c = 4.662 \text{ mm}$ ,  $\theta = 68.23^\circ$ ,  $L = 15.613 \text{ mm}$  and  $T_{w,in} = 29.72 \text{ }^\circ\text{C}$  for a discharge rate of 3C and an ambient temperature of  $35 \text{ }^\circ\text{C}$ . Grid convergence is computed for two variables: maximum temperature and pressure drop. As seen in Table 4.3, the variations in both variables are less than 1%, with the number of nodes exceeding  $7.5 \times 10^6$ . This indicates that the number of nodes  $7.5 \times 10^6$  is dense enough to ensure accuracy and is considered for simulation.

Table 4.3: Grid independence results

Number of nodes	$T_{\max}$ ( $^\circ\text{C}$ )	$e$ (%)	$\Delta P$ (Pa)	$e$ (%)
$3.3 \times 10^6$	36.69	0.03	380.40	3.23
$5.8 \times 10^6$	36.69	0.02	382.80	2.62
$7.5 \times 10^6$	36.69	0.02	391.90	0.31
$8.0 \times 10^6$	36.68	-	393.10	-

#### 4.4.2 Experimental validation of the ECT model

Experimental validation is carried out to verify the stability of the electrochemical-thermal (ECT) battery model. The details of the experimental test rig are already reported in Fig. 2.2. The experimental procedure followed to test the battery is as follows:

- 1) Place the cell in an environmental chamber at an ambient temperature of  $35 \text{ }^\circ\text{C}$  and connect it to the battery tester. Wait till the battery reaches chamber temperature.
- 2) Discharge at constant current (CC) of 2C-rate with a fully charged cell and a minimum voltage of 2.5 V. C-rate is the measure at which the battery is charged or discharged.
- 3) Rest 30 min for heat dissipation.

- 4) Charge the cell in a galvanostatic (CC-) mode at 1C-rate with a maximum voltage of 3.65 V followed by potentiostatic (Constant voltage, CV-) mode till the cut-off current reaches 0.2 A. At this stage, the battery reaches a state of charge (SOC) between 80% and 90%.
- 5) Rest 30 min for potential balance.
- 6) Repeat steps 2-5 to conduct the battery's charge/discharge cycling test.

Fig. 4.3 displays the current and voltage profile of the battery during the charge-discharge cycle test. In the graph, C represents charging. R and D indicate rest and discharge, respectively. The temperature at five different locations and heat flux at the central region of the battery surface during the cyclic test is displayed in Fig. 4.4.

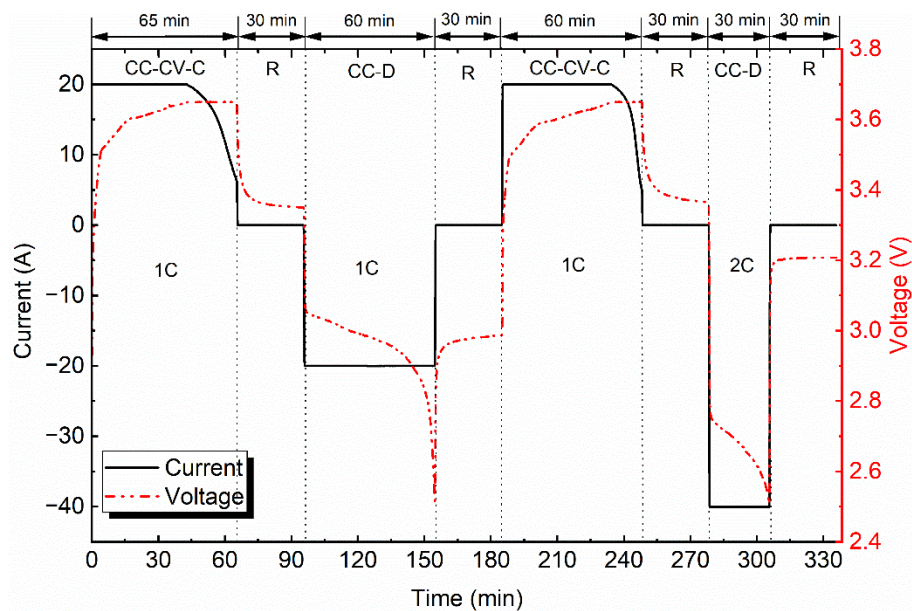


Fig. 4.3: Variation in current and voltage concerning time during the cycle test

The average battery temperature obtained from the five thermocouples of cell surface is used to validate the numerical results. Fig. 4.5 shows a closer agreement between the experimental and simulation results, assuring the validity and accuracy of the battery ECM model.

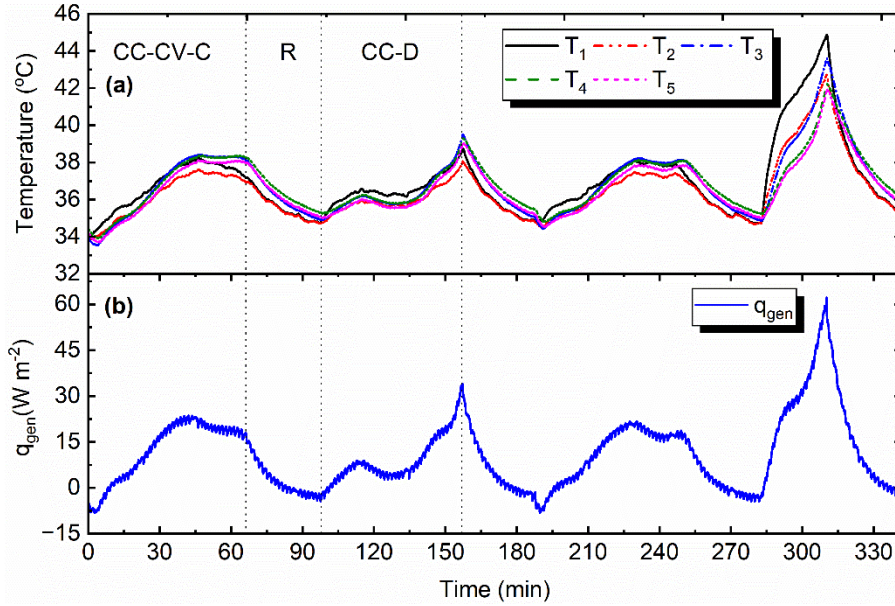


Fig. 4.4: Variation of (a) temperature at different locations and (b) heat flux at the central region of the battery

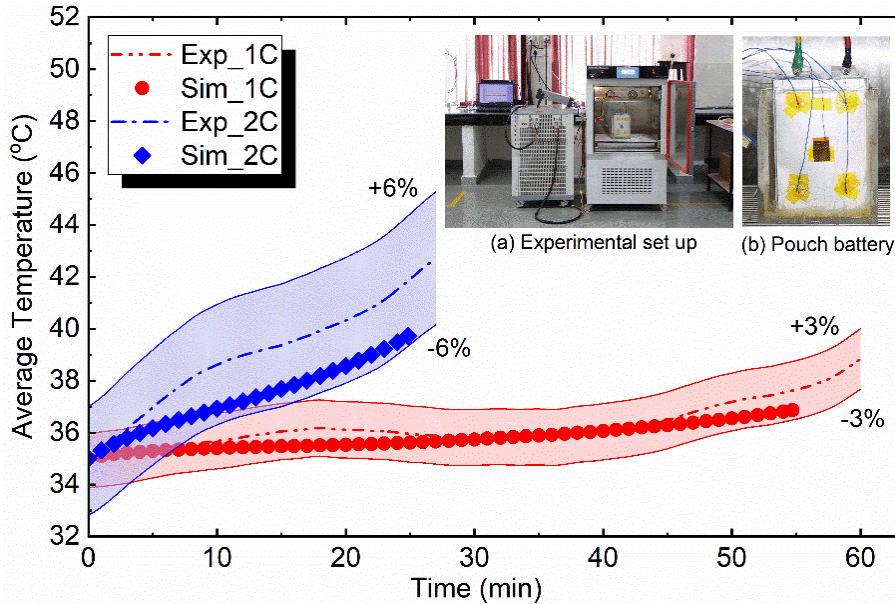


Fig. 4.5: Validation of numerical results with the experiment for varying discharge rate

### 4.4.3 Effect of discharge rate on cooling effectiveness

Due to the unavailability of experimental data for the hexagonal channel design integrated with a pouch battery module, preliminary simulations are conducted at varying discharge rates to self-validate the ECT model when coupled with a conjugate heat transfer model.



In parallel, these simulations aid in investigating the cooling efficiency of the initial hexagonal design before the optimization techniques are applied. Here,  $\dot{m}_w = 0.003 \text{ kg s}^{-1}$ ,  $W_c = 3.25 \text{ mm}$ ,  $\theta = 120^\circ$ ,  $L = 16.25 \text{ mm}$  and  $T_{w,in} = 25^\circ \text{C}$  for a discharge rate of 3C and an ambient temperature of  $35^\circ \text{C}$ .

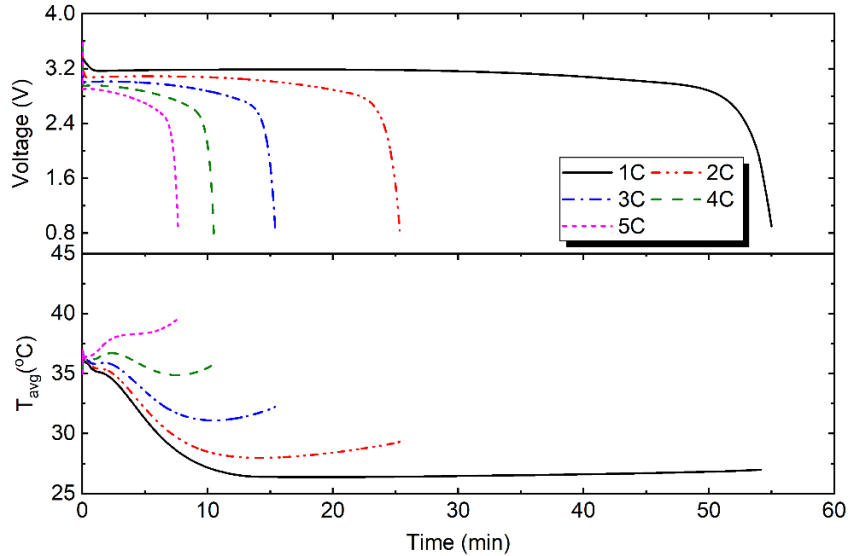


Fig. 4.6: (a) Change in the discharge voltage and (b) average temperature for different discharge rates

Fig. 4.6 shows the transient variation in voltage and maximum temperature of battery module for varying discharge rates. It is noticed that the voltage trend remains unchanged with an increase in discharge rate of 1C and 2C even when coupled with a cooling channel design compared to that of a single battery (refer to Fig. 4.5&4.6), thus validating the reliability and accuracy of the model. Besides this, the  $T_{avg}$  of the module is seen to reduce with the initiation of cooling for all the discharge rates. For instance, in the case of 1C, the  $T_{avg}$  reaches almost ambient value, with an increase of discharge rate to 5C,  $T_{avg}$  increases by  $12^\circ \text{C}$ . In real-time, on-road driving conditions can increase batteries' charge and discharge rates, causing an uneven temperature distribution and performance degradation. Thus, adequate cooling and a well-designed channel are required to control the temperature

disparity across the module. Keeping this in view, the present work considers a mid-range discharge rate, i.e., 3C, to evaluate the battery module's performance and optimize the channel design for effective cooling.

#### 4.4.4 Accuracy analysis of ML models

The dataset used as input for the ML models comprises numerical findings for the distinctive points obtained using the ESE-LHS method (Appendix A). Among the dataset of 160, 140 are randomly selected for training, and the remaining are used for testing the model and evaluating the fitting accuracy of design points and the objective functions. The HPT procedure followed for all the models considered is described in the previous subsection 3.5. Table 4.4 summarizes the error metrics for the ML models trained using the ESE-LHS data.

Table 4.4: Metrics for the different ML models trained using the dataset A

Objectives	Metrics	MLR	RSM-Poly	Kriging	SVM
$T_{\max}$ ( $^{\circ}C$ )	NRMSE	0.0285	0.0183	0.0154	0.0184
	NMAD	0.0166	0.0129	0.0086	0.0098
	NMAE	0.0213	0.0148	0.0123	0.0139
	$R^2$	0.8273	0.9344	0.9515	0.9332
$\Delta P$ (Pa)	NRMSE	0.3152	0.2008	0.1786	0.2320
	NMAD	0.1872	0.1625	0.1409	0.1247
	NMAE	0.2518	0.166	0.1460	0.1737
	$R^2$	0.8365	0.9164	0.9314	0.8761
$h_w$ ( $W m^{-2} ^{\circ}C^{-1}$ )	NRMSE	0.0942	0.0789	0.0788	0.0816
	NMAD	0.0470	0.0454	0.0454	0.0523
	NMAE	0.0655	0.0608	0.0551	0.0608
	$R^2$	0.8823	0.9316	0.9296	0.9217

It can be inferred that the Kriging model attains the best results among the four ML models in the case of  $T_{\max}$  ( $R^2 = 0.9515$ ) and  $\Delta P$  ( $R^2 = 0.9314$ ), followed by RSM, SVM and MLR. Irrespective of the objective function, MLR performs inferiorly with widely scattered data points (Fig.4.7) and the lowest  $R^2$  value. A higher  $R^2$  value would reflect that the model trained could accurately predict the relation between the design points and the objective

functions. In addition, the data points of the Kriging cluster appear to be within close proximity to the diagonal line, which may also show that the model predictive performance is very firm and is a good fit for the data. This suggests that Kriging’s spatial correlation modelling is highly suitable for the data set, likely leading to the highest  $R^2$  value.

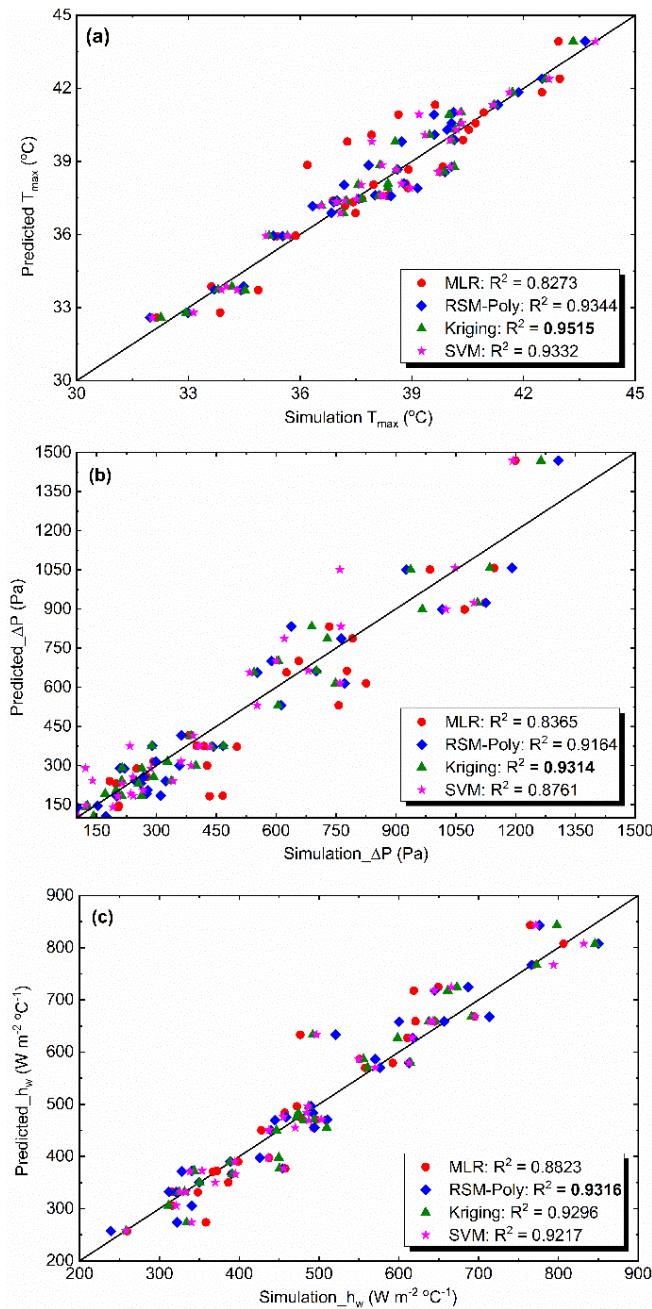


Fig. 4.7: Parity plot of randomly tested data for different ML models

The RSM, placed second, indicates that it captured the curvature in the data effectively, but it could not surpass the performance of Kriging. Although SVM showed a reasonable fit to the diagonal line, there is still some spread. However, it could outperform MLR, emphasizing the presence of non-linear patterns successfully captured by the SVM's Kernel functions, whereas MLR's reliance on linear assumptions is less suitable for the dataset. In the case of  $h_w$ , RSM performed the best compared to the other ML models by achieving the highest  $R^2$ . However, the difference in error metrics between RSM ( $R^2 = 0.9316$ ) and Kriging ( $R^2 = 0.9296$ ) is noticed to be marginal. Although, a spatial correlation is present in the data, the quadratic correlations captured by RSM gave a slightly better fit. Hence, with Kriging as the selected ML model, NSGA II is employed for conducting the MOO procedure.

#### 4.4.5 Optimization results and verification

In the current work, equal weights are given to maximum temperature, pressure drop and heat transfer coefficient for the NSGA II to generate optimal set of solutions that provides a trade-off among these conflicting objectives. Fig. 4.8 displays the Pareto optimal frontier (POF) obtained using NSGA II for the three objectives, including  $h_w$  (Maximizing) along the vertical axis,  $T_{\max}$  and  $\Delta P$  (Minimizing) along the horizontal axes. Since there are three objectives, the Pareto front takes a complex and non-linear shape. The front comprises diverse non-dominated solutions, each offering different trade-offs between the three objectives. The end points of POF represent a pair comprising a lower value of one objective and the highest of the other. This can be attributed to the natural conflict between  $h_w$ ,  $T_{\max}$  and  $\Delta P$ , as one of them is maximizing while the other two are to be minimized.

Once the POF is examined, designers may gain insight into solutions targeted to their preferences and priorities. For example, focusing on objective maximization of the  $h_w$  results in searching for solutions closer to the front's maximizing boundary. It may be accomplished at the expense of achieving higher values for the minimization objectives. In contrast, if one wants to achieve equally good performance for all the three objectives, bounds located in the central area of the front will be most suitable. The Pareto front enables complete exploration of the decision space, allowing the designers to make prudent choices according to their application's needs.

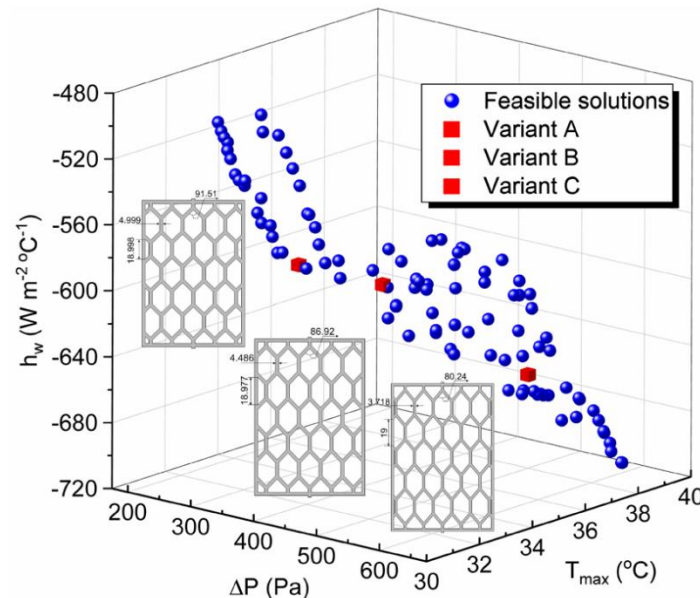


Fig. 4.8: Pareto optimal (blue) and representative solutions (red) obtained using NSGA II and K-means clustering, respectively

The K-means clustering algorithm is utilized to obtain the representative solutions (Points with a red mark in Fig. 4.8 to verify the accuracy of the ML model selected and the optimizer performance. It also helps to evaluate the relationship between design points and objective functions. Table 4.5 summarizes the corresponding values of design points and objective functions for the three representative solutions. The  $\dot{m}_w$  is kept constant at 0.003

$\text{kg s}^{-1}$  and is given as a constraint (Section 3.6) to maintain uniformity during comparison. The predicted values of the objective functions are then compared with the ones attained by simulations. The difference between the two values is computed as follows:

$$e(\%) = \left( \frac{X_{CFD} - X_{MOGA}}{X_{CFD}} \right) \times 100 \quad (4.18)$$

Table 4.5: Comparison between numerical and Kriging-RBF predicted values for the obtained Pareto optimal solutions

<b>Design</b>	<b>A</b>	<b>B</b>	<b>C</b>
$L$ (mm)	18.998	18.977	19.000
$W_c$ (mm)	4.999	4.486	3.718
$\theta$ ( $^\circ$ )	91.513	86.915	80.236
$T_{w,in}$ ( $^\circ\text{C}$ )	25.041	26.383	29.164
$\dot{m}_w$ ( $\text{kg s}^{-1}$ )	0.003	0.003	0.003
<b>Predicted results</b>			
$T_{\max}$ ( $^\circ\text{C}$ )	32.56	33.34	35.72
$\Delta P$ (Pa)	363.18	464.10	595.19
$h_w$ ( $\text{W m}^{-2} \text{ }^\circ\text{C}^{-1}$ )	580.80	587.89	642.96
<b>Simulation results</b>			
$T_{\max}$ ( $^\circ\text{C}$ )	32.28	33.53	36.10
$\Delta P$ (Pa)	369.50	436.40	543.15
$h_w$ ( $\text{W m}^{-2} \text{ }^\circ\text{C}^{-1}$ )	537.22	578.81	628.37
<b>Relative error (%)</b>			
$T_{\max}$ ( $^\circ\text{C}$ )	0.85	0.58	1.05
$\Delta P$ (Pa)	1.71	6.35	9.58
$h_w$ ( $\text{W m}^{-2} \text{ }^\circ\text{C}^{-1}$ )	8.11	1.57	2.32

For Variant B, the maximum error in the predictions of  $T_{\max}$  is observed to be less than 1%, whereas the  $\Delta P$  limits the error less than 7%, and  $h_w$  is within 2%. The deviations of Variants A and C are marginally higher. Although the disparity in  $T_{\max}$  is within 1%,  $\Delta P$  and  $h_w$  show an error below 10%. This specifies that the predicted values agree with the simulation results. It can be noticed from Table 4.5 that the values of  $T_{\max}$  are within the recommended range of 25  $^\circ\text{C}$  – 40  $^\circ\text{C}$ . The values of  $L$  and  $W_c$  are nearer to the upper

bound, while the  $\theta$  and  $T_{w,in}$  values are somewhere in the middle of the bound, indicating their sensitivity.

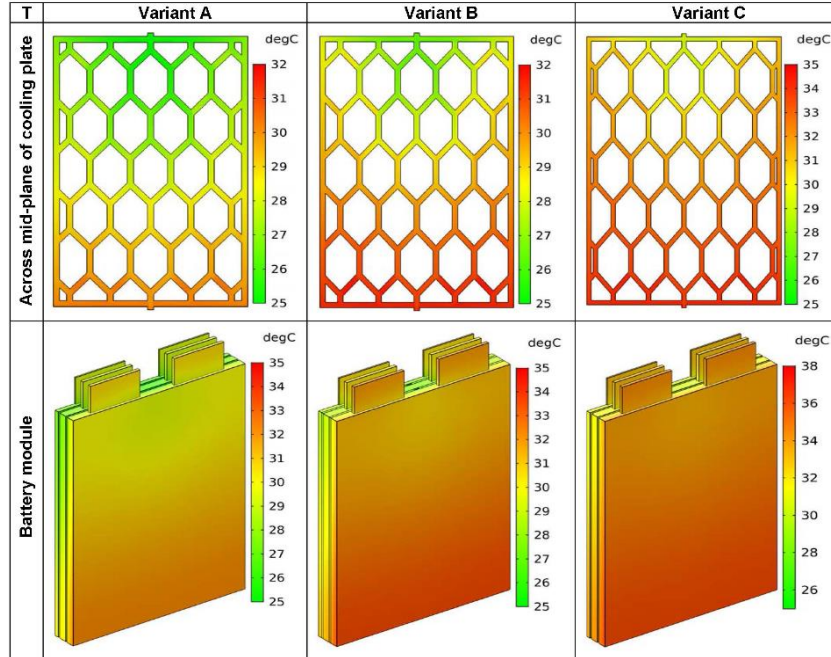


Fig. 4.9: Temperature contours across the mid-plane of the cooling plate and battery module for the Variants A, B and C

It is seen that the  $T_{\max}$  is almost 3 °C higher for the case of Variant C when compared to that of A and B. The same phenomenon is noticed for  $\Delta P$  and  $h_w$ . This is due to the increased  $T_{w,in}$  and reduced  $W_c$ , thereby affecting the flow distribution and heat transfer across the surface of the cooling plate. Additionally, this led to the localized temperature hot spots across the module (Fig. 4.9). In contrast, Variant A and B show a lesser  $T_{\max}$  and  $\Delta P$ , however, at the expense of slightly lower  $h_w$ , because of the increase in  $W_c$  and  $\theta$ , resulting in the amplification of heat transfer area. This helps to achieve a uniform and well-distributed thermal profile, reflecting good heat dissipation and minimal hotspots. It can be noted that the battery region near the cooling plate's inlet experienced a lesser

temperature than the one near the bottom. In brief, the temperature distribution is homogenous with Variant A, followed by Variant B and C. However, all three results obtained are within the safe operating range of a battery.

#### 4.4.6 Feature importance using SHAP

SHAP (Lundberg and Lee 2017) is a novel technique that expands upon the Shapley values of cooperative game theory; It evaluates ML models more meaningfully by interpreting the input features that matter most to various output. The principle on which this technique is built is to assign the credits of output features to the inputs or allocate the attribution of an output feature across the inputs. By taking advantage of the Shapley values properties, SHAP makes it possible to determine how important each of the individual input feature is to the output, thereby allowing for a comprehensive analysis of any ML model.

As LHS is used for generating the data required for training, the fundamental influence of the input features is not readily evident. However, as the proposed Kriging model accurately represents the relation between the input and output features, the SHAP method is used to determine the impact of features, i.e. finding out the most influenced design variable for a specific output ( $T_{\max}$ ,  $\Delta P$  and  $h_w$ ). These variables are, hence the most significant while optimizing the channel design. The SHAP plots for each output are displayed in Figures 4.10-4.12. Here, plot (a) represents bees warm plot and (b) signifies the summary bar plot.

Bees warm plot helps in visualizing the distribution of SHAP values among the features in a dataset. In brief, it offers a concise overview of the relationship between the most important features in a dataset and the model's output. A dot on the particular feature row



represents the explanation for each instance. The x-position of the dot is determined by the SHAP value for that specific feature and these dots stack-up along the feature row to indicate density. A wide dispersion or higher dot density specifies a greater impact on model's predictions. This enables us to evaluate a feature's significance in influencing the model's output. For a given feature, the corresponding feature value can positively or negatively impact the output depending on whether it is increasing (red) or decreasing (blue). The features are sorted based on the maximum absolute SHAP values, highlighting the ones showing significant impact on that particular output. In the current work, the coolant inlet temperature and mass flow rate are seen to have most influence on maximum temperature (Fig. 4.10a). Whereas, pressure drop (Fig. 4.11a) and heat transfer coefficient (Fig. 4.12a) are predominantly influenced by mass flow rate of coolant and channel width.

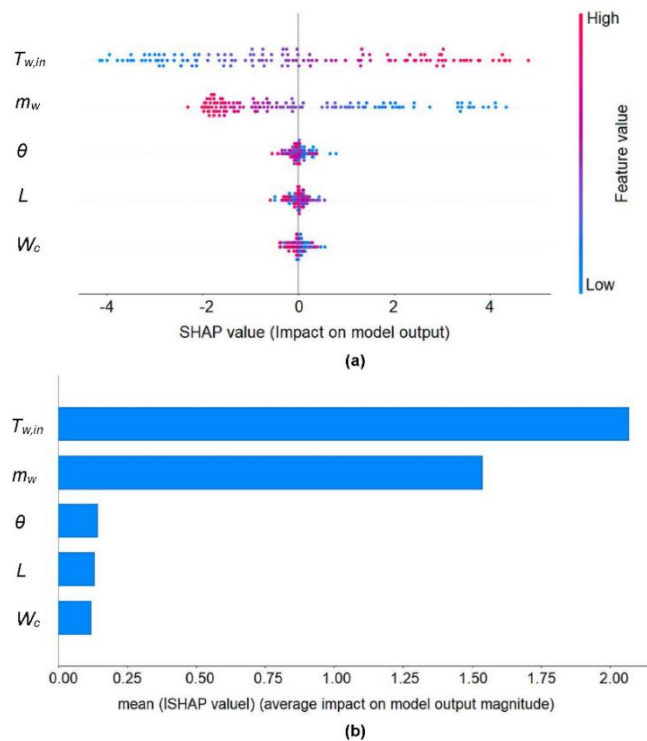


Fig. 4.10: (a) Bees warm plot (on the top) and (b) summary bar plot (on the bottom) to determine feature impact using Kriging model output on  $T_{\max}$

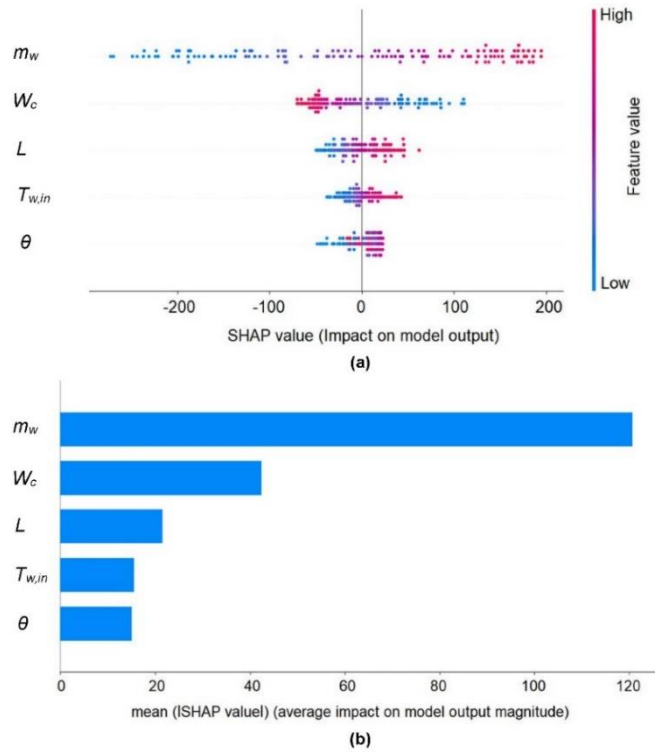


Fig. 4.11: Feature impact using Kriging model output on  $\Delta P$

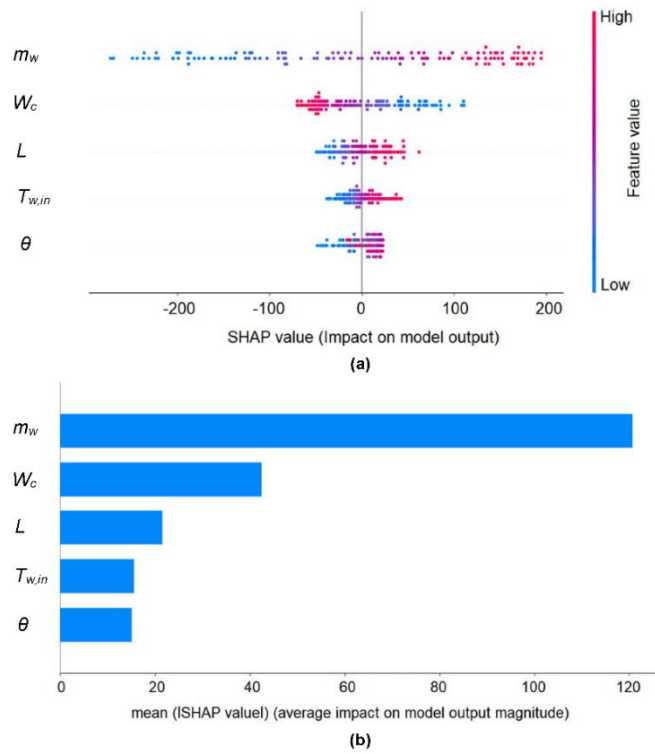


Fig. 4.12: Feature impact using Kriging model output on  $h_w$

The summary bar plots, on the other hand, are another effective visual tool, providing an insight into the importance of each feature on the ML model. It uses horizontal bars to show the magnitude and direction of the features influence on the model's output. Longer the bar, more significant the importance of feature on that particular output. The average absolute SHAP values are used to determine the feature order. The results attained are similar to that of the bees warm plots.

However, given the nature of ML technique, the SHAP approach could have certain limitations. This is due to the fact that one relies on data driven models, which are often based on either limited or misrepresented, making it difficult to understand and explain the cause of underlying issue fully. However, considerable efforts have been made recently to link the data-driven and physics-based techniques by incorporating well-known physics concepts in these ML models (Karniadakis *et al.* 2021). In addition, ML based techniques have been applied to increase our understanding of complex systems and elucidate the underlying physics (Karagiorgi *et al.* 2022).

#### 4.4.7 Comparative analysis

The representative solutions obtained using K-means clustering are compared with the initial design ( $L = 16.25$  mm,  $W_c = 3.25$  mm and  $\theta = 120^\circ$ ) under the same conditions for a wide range of  $\dot{m}_w$ . All the variants showed a negligible deviation concerning the temperature when compared with the initial design. On average, for a given flow rate, the change in temperature difference between the two designs is below 0.2%. Hence, the evaluation is conducted based on  $\Delta P$  and  $h$ , and the corresponding plots are displayed in Fig. 4.13.

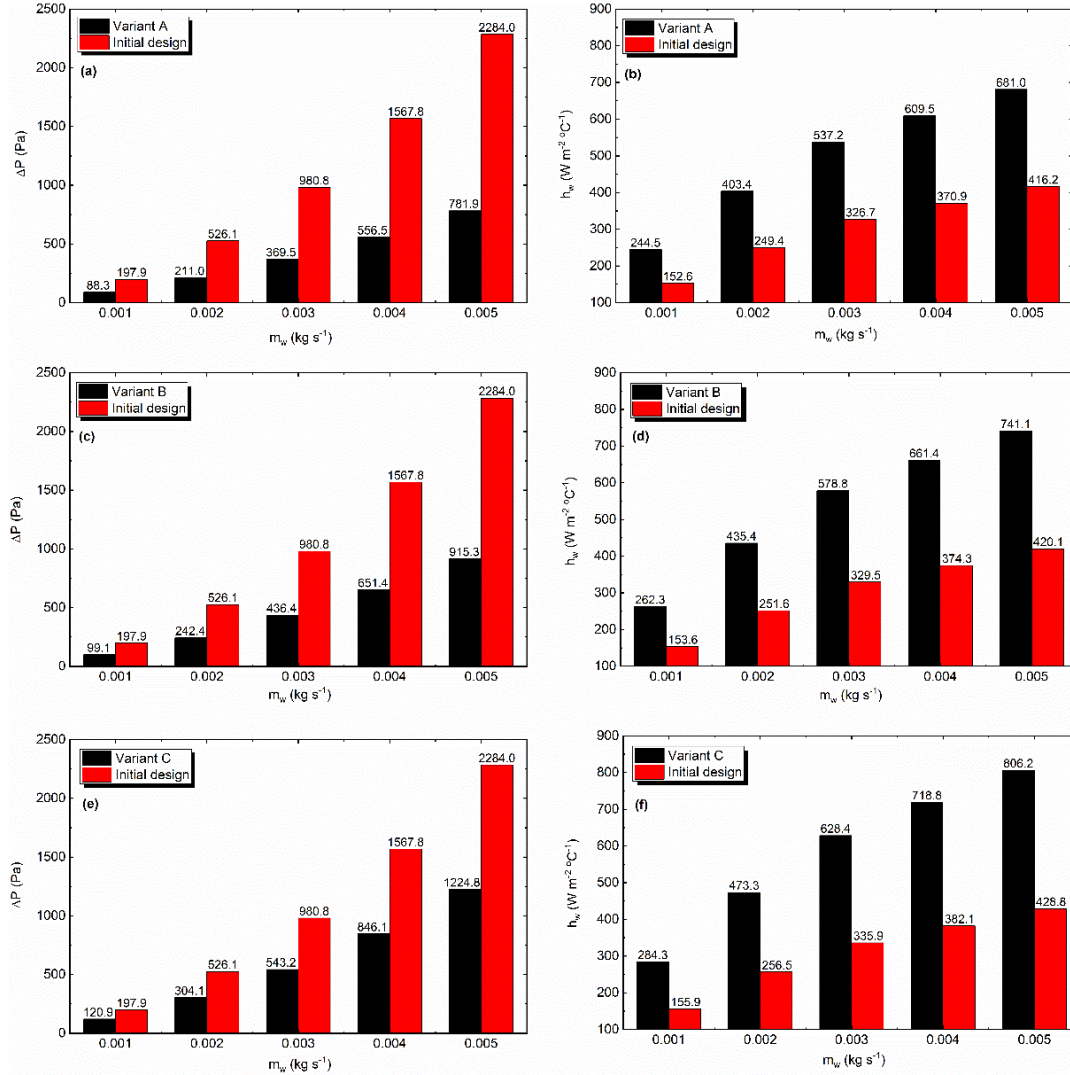


Fig. 4.13: Comparison of  $\Delta P$  and  $h_w$  for (a, b) Variant A, (c, d) Variant B, and (e, f) Variant C with the initial design for varying  $\dot{m}_w$

Fig. 4.13(a) illustrates the relation between  $\Delta P$  and varying  $\dot{m}_w$  while Fig. 4.13(b) showcases the evolution of  $h_w$  with different  $\dot{m}_w$  for both initial and optimal designs. It can be seen that the optimized design, i.e., Variant A yields a consistent improvement in  $\Delta P$  and  $h_w$  across different  $\dot{m}_w$ . For instance, Variant A shows a 55.37% reduction of  $\Delta P$  and an improvement of 60.27% in  $h_w$  for a  $\dot{m}_w$  of 0.001 kg s<sup>-1</sup> than that of the initial design. As the  $\dot{m}_w$  increases to 0.005 kg s<sup>-1</sup>,  $\Delta P$  is reduced by 65.76%, whereas  $h_w$  is enhanced by

63.61%. In other words, with the increase in  $\dot{m}_w$  from 0.001 to 0.005 kg s<sup>-1</sup>, a reduction of 18.76% is seen in the  $\Delta P$  while the  $h_w$  is improved by 5.55% with Variant A compared to the initial design. The drop in  $\Delta P$  shows a remarkable flow efficacy, resulting in significant energy savings within the cooling system. In addition, the improvement in  $h_w$  is necessary to keep the battery module's temperature uniform and prevent localized heating.

Table 4.6: Evaluation of the optimal design with the initial design under a  $\dot{m}_w$  of 0.003 kg s<sup>-1</sup>

Design	Range	Initial value	Optimal value	Improvement
$L$ (mm)	[15, 19]	16.25	18.99	-44.68%
$W_c$ (mm)	[3, 5]	3.25	4.99	+53.54%
$\theta$ (°)	[60, 120]	120	91.51	-23.74%
$T_{w,in}$ (°C)	[25, 35]	25	25.04	+0.16%
<b>Objectives</b>				
$T_{max}$ (°C)	Min	32.26	32.28	+0.07%
$\Delta P$ (Pa)	Min	980.8	369.5	-62.32%
$h_w$ (W m <sup>-2</sup> °C <sup>-1</sup> )	Max	326.75	537.2	-64.41%

Similar results can be seen with Variants B and C. Compared with the initial design, the  $\Delta P$  is reduced by 49.93% and 38.90%, while  $h_w$  is enhanced by 70.83% and 82.42% for a  $\dot{m}_w$  of 0.001 kg s<sup>-1</sup> with Variants B and C, respectively. With the increase of  $\dot{m}_w$  to 0.005 kg s<sup>-1</sup>,  $\Delta P$  reduces by 59.93% and 46.37%, whereas an improvement of 76.43% and 88% in  $h_w$  is noticed with Variants B and C, respectively. In brief, as the  $\dot{m}_w$  varies from 0.001 to 0.005 kg s<sup>-1</sup>, Variants B and C can achieve an overall reduction of 20% and 19.21% in  $\Delta P$ , while an enhancement of 7.89% and 6.78% in  $h_w$ , respectively. Thus, these results indicate that optimized designs are effective in augmenting the performance of cooling plates. Table 4.6 summarizes the assessment of optimal design i.e., Variant A with the initial design for a  $\dot{m}_w$  fixed at 0.003 kg s<sup>-1</sup>.

Altogether, it can be said that the results exhibited collectively provide a holistic understanding of how optimization progressively influences the cooling plate's performance and its potential implications in regulating the temperature of the battery module.

## 4.5 Summary

The current work investigates the performance enhancement of the hexagonal channel design proposed in the previous chapter to cool the battery module by applying multi-objective optimization techniques. Three geometric and two operational parameters are considered for the optimization. ESE-LHS is utilized to generate a dataset of distinctive sample points. The three objective functions, i.e.  $T_{\max}$ ,  $\Delta P$  and  $h_w$ , are computed numerically using COMSOL Multiphysics for each sample point. Later, the obtained data is used for training surrogate models, and the best one is coupled with NSGA II to produce optimal design solutions. The conflicting nature of objectives is evident in the POF. The critical findings obtained are as follows:

- The Kriging model emerges as the most promising ML model with consistent performance for most cases, despite a smaller difference in the  $R^2$  value with RSM for  $h_w$ .
- The SHAP analysis indicates that  $\dot{m}_w$  and  $T_{w,in}$  are the main variables regulating the change in  $T_{\max}$ .  $\Delta P$  and  $h_w$  are driven mainly by the  $\dot{m}_w$  and  $W_c$ .
- After the optimization, the resultant Pareto solutions showed a  $T_{\max}$  varying from 31.75 °C to 38 °C. The  $\Delta P$  varies from 224.4 Pa to 649.9 Pa, and  $h_w$  from 493.35

$\text{W m}^{-2} \text{C}^{-1}$  to  $703.40 \text{ W m}^{-2} \text{C}^{-1}$ . The improvements can be elucidated as a compromise between the output features.

- Besides this, the three best solutions (A, B and C) selected by the K-means clustering algorithm from the Pareto front are validated numerically, for which the maximum relative error is found below 10%, further confirming the validation of the Kriging model selected.
- The initial design is compared with the best solutions for varying  $\dot{m}_w$  and a significant improvement in overall performance is seen with the optimized designs.

Finally, a hexagonal channel design with  $L = 18.99 \text{ mm}$ ,  $W_c = 4.99 \text{ mm}$ ,  $\theta = 91.51^\circ$ , and

$T_{w,in} = 25.04 \text{ }^\circ\text{C}$  is ideal for the thermal management of 20Ah Li-ion battery module.

# Chapter 5

## Introducing an Innovative Cold Plate Design with Multi-Stage Tesla Valve for Enhanced Cooling of Pouch-Type Li-ion Batteries

### Keywords

Multi-stage Tesla valve;  
Thermal management;  
Channel design;  
Pouch batteries;  
Reverse flow;  
Simulation.

*A liquid cooling plate comprising Tesla valve configuration with high recognition in microfluidic applications is proposed to provide a safer temperature range for pouch type Li-ion batteries. A multi-stage Tesla valve with forward and reverse flow configuration is designed and analyzed to improve a conventional rectangular channel's intrinsic temperature gradient issues for turbulent flow conditions. Moreover, the influence of various parameters such as channel number, the distance between two consecutive valves, channel width, outer curve radius, and valve angle are numerically investigated for varying Reynold's number by applying heat flux on the cooling plate's upper and lower surfaces using COMSOL Multiphysics software.*

### 5.1 Introduction

Until date, several investigations have been carried out on the cooling plate configuration for battery TMS since this shows a substantial impact on the performance of the overall cooling system. Considering the previously mentioned research works, it is understandable that most of the literature focuses on improving the existing channel layout, modifying the design features, or incorporating fins. Conversely, the temperature gradient is still greater than 2 °C as there exists a limitation in heat transfer coefficient enhancement. Unlike the formerly employed channel designs, the present work suggests a novel liquid cooling channel plate by utilizing the Tesla valve design that has grown to prominence in microfluidics, micro-pumps, microelectronics, fuel cell, and heat



pipe systems (Bardell and Microsciences 2017; Wahidi *et al.* 2020). A standard Tesla valve functions as a fluidic diode, allowing the fluid to flow in both forward and reverse directions, inflicting direction-dependent pressure drop. Porwal *et al.* (2018) successfully analyzed the ability of a multi-staged Tesla valve to operate as a mini or microchannel heat exchanger in both forward and reverse directions. Qian *et al.* (2019) utilized the working principle of the Tesla valve's reverse flow to decompress hydrogen for a fuel cell in an EV. Also, the pressure and velocity within the multi-stage Tesla valve (MSTV) are dramatically affected by varying the number of stages, including the pressure ratio across the entry and exit of each valve. A power-law relation is also derived among stage number, flow rate, and pressure ratio.

Despite the extensive studies on the Tesla valve in various fields, its application in an indirect liquid cooling system with a cold plate on the battery thermal management is still unnoticed. From this perspective, the present work explores the potential of MSTV design as a mini channel cold plate for TMS of pouch-type batteries to achieve thermal homogeneity.

The current work is systematized in the following way: A 3D numerical model of the cold plate embedded with MSTV is designed and developed to mitigate the temperature disparities across the pouch-type batteries using COMSOL Multiphysics software. Preliminary simulations are conducted to compare the effectiveness of forward and reverse directions in MSTV with the straight channel design under turbulent flow conditions by varying Reynolds number from 2500 to 5500. The structural parameters of the MSTV design, including channel count, valve-to-valve distance, channel width, outer curve radius, and valve angle, are considered variables to examine its cooling proficiency. The

main motive behind choosing a multi-stage design is that it can offer lower frictional resistance, intensifying the fluidic diode effect. Furthermore, temperature, pressure, and velocity distributions are examined to analyse the flow behaviour of a typical MSTV design.

## 5.2 Methodology

### 5.2.1 Model and analysis

To address the limitation of temperature accumulation in a conventional rectangular channel and enhance the temperature distribution homogeneity, an MSTV design inspired by (Gamboa *et al.* 2005) is introduced, which is extensively used in mini/microfluidic applications.

Fig. 5.1 shows a schematic layout of the battery module with the liquid cooling system and its geometrical features. The battery module arrangement considered in this study comprises two thin rectangular pouch cells. A cold plate of the same rectangular dimension is placed between two consecutive cells. The heat generated by batteries acts on the cold plate's lower and upper surfaces. The coolant flowing across the cooling plate exchanges heat with batteries, reducing its temperature. The cooling plate consists of 3D mini channels with a 10-staged MSTV design, as shown in Fig. 5.1(a). Due to the complexity of the design and to reduce the computational load, constant heat flux is applied on the top and bottom surfaces of the cold plate, as shown in Fig. 5.1(b). As seen in the magnified image of Fig. 5.1(b), a single Tesla valve comprises bent and straight channel segments, while an MSTV is formed by combining a number of Tesla valves in series. The external dimensions of the cooling plate, i.e., 160 mm (W)×227 mm (L)×2 mm (t), are ascertained

by using the size of a 20Ah pouch battery 160 mm×227 mm×7.25 mm used in EVs. The other dimensional parameters of the cold plate are presented in Table 5.1.

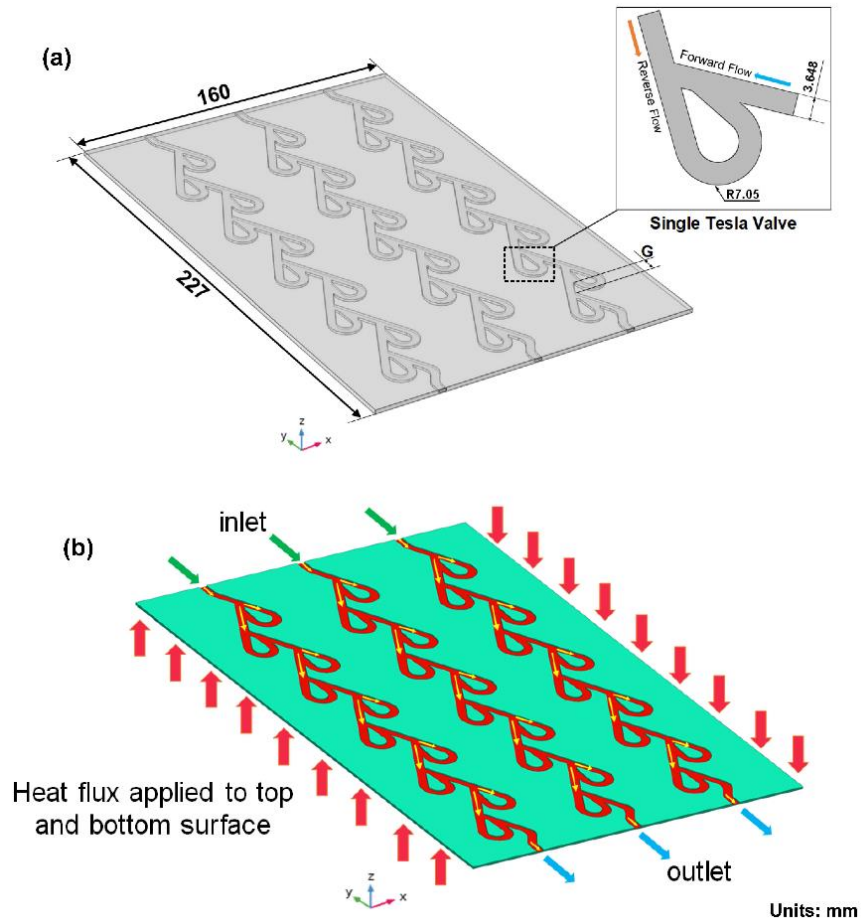


Fig. 5.1: (a) A 3D cold plate with MSTV design and (d) Sectional view of cooling plate representing a reverse flow in MSTV

Table 5.1: Cold plate parameters

Parameter	Value
Plate length, $L$ (mm)	227
Plate width, $W$ (mm)	160
Plate thickness, $t$ (mm)	2
Channel width, $W_c$ (mm)	3.648
Channel depth (mm)	1
Outer curve radius, $R$ (mm)	7.05
Valve angle, $\theta$ ( $^\circ$ )	41.6
Valve to valve distance, $G$ (mm)	8.82
Number of stages, $N$	10

## 5.2.2 Boundary conditions

The boundary conditions related to the cooling system are provided below:

- Velocity is defined at the inlet of the cooling plate by varying  $Re$  from 2500 to 5500

$$\omega_{in} = \frac{Re \mu}{\rho D_h}, \text{ where } D_h = \frac{4A_{ch}}{P} \quad (5.1)$$

- At the outlet, a pressure of 0 Pa is specified.
- Constant heat flux is assigned to the cooling plate's top and bottom surfaces, assuming the other walls are adiabatic. Assuming the cold plate is positioned between two successive batteries connected in series, where each battery's capacity and voltage are 20 Ah and 3.3 V, the heat flux is calculated as  $\phi = P_h / A' = 7269 \text{ W m}^{-2}$  for a battery discharging at 4C and generating heat of 264 W.
- The interior surfaces of the cooling plate are given a no-slip boundary condition.

## 5.2.3 Assumptions

The following assumptions are made for the cooling plate simulation:

- The coolant flow is assumed to be single-phase, steady, incompressible and turbulent.
- The cooling plate is homogenous and isotropic.
- The properties of working fluid and solid are temperature-independent.
- Except for the heat flux applied surfaces, the remaining faces of a cold plate are assumed to be adiabatic.
- Gravity and viscosity dissipation effects are neglected.

The thermophysical properties of cooling fluid (water) and solid (aluminium) assumed for the present investigation are provided in Table 3.2.

## 5.2.4 Governing equations

The equations governing the fluid flow are same as mentioned in Eq.'s 3.5 to 3.7. Due to its robustness, the standard  $k$ - $\varepsilon$  turbulence model is utilized for modelling turbulent flow with a turbulent intensity of 5% (Deng *et al.* 2019). The transport equation of turbulent kinetic energy is expressed as

$$\frac{\partial(\rho\kappa)}{\partial(t)} + \bar{\nabla} \cdot (\rho\kappa\bar{v}) = \bar{\nabla} \cdot [\alpha_{\kappa} (\mu + \mu_t) \cdot \bar{\nabla}(\kappa)] + 2\mu_t E_{ij} \cdot E_{ij} - \rho\varepsilon \quad (5.2)$$

Here,  $k$ ,  $\varepsilon$  and  $\mu_t$  represent turbulent kinetic energy, turbulent dissipation rate and turbulent dynamic viscosity, respectively. The transport equation of turbulent dissipation rate is expressed as

$$\frac{\partial(\rho\varepsilon)}{\partial(t)} + \bar{\nabla} \cdot (\rho\varepsilon\bar{v}) = \bar{\nabla} \cdot [\alpha_{\varepsilon} (\mu + \mu_t) \cdot \bar{\nabla}(\varepsilon)] + C_{1\varepsilon}^+ \frac{\varepsilon}{\kappa} 2\mu_t E_{ij} \cdot E_{ij} - C_{2\varepsilon} \rho \frac{\varepsilon^2}{\kappa} \quad (5.3)$$

The turbulent (or eddy) viscosity is calculated as

$$\mu_t = \frac{\rho \times C_{\mu} \times k^2}{\varepsilon} \quad (5.4)$$

$$C_{1\varepsilon}^+ = C_{1\varepsilon} - \frac{\eta(1-\eta/\eta_0)}{1+\beta'\eta^3} \quad (5.5)$$

$$\eta = \left(2E_{ij} \cdot E_{ij}\right)^{\frac{1}{2}} \frac{\kappa}{\varepsilon} \quad (5.6)$$

where,  $C_{\mu} = 0.00845$ ;  $\alpha_{\kappa}$  and  $\rho\varepsilon$  are 1.39;  $C_{\kappa}$  and  $C_{\varepsilon}$  are 1.42 and 1.68, respectively.  $\eta_0$  and  $\beta'$  are 4.377 and 0.012, respectively. The turbulent viscosity ratio,  $\eta$ , is 10.

In addition, a heat transfer between the channel wall and cooling fluid exists as per Newton's law of cooling (Eq. 3.4).

## 5.2.5 Data reduction

A 3D cold plate model is developed and designed using CATIA V5; later, the solid file is imported into COMSOL Multiphysics software for meshing and analysis. The effectiveness of the cold plate with MSTV design is evaluated through maximum temperature ( $T_{\max}$ ), standard deviation ( $T_{\sigma}$ ) and pressure drop ( $\Delta P$ ) across inlet and outlet of the cold plate. The  $T_{\max}$  is considered as it represents the battery's worst working conditions. Also,  $T_{\sigma}$  which is an indicator of the heat transfer coefficient and reflects the homogenous temperature distribution of the battery is considered. The lesser the temperature variance of the cell, greater the amount of heat carried away by coolant and more homogenous the distribution. The surface  $T_{\sigma}$  can be calculated using Eq. (5.7).

$$T_{\sigma} = \sqrt{\frac{\int_A (T - T_{avg})^2 dA}{\int_A dA}}, \text{ where } T_{avg} = \frac{\int_A T dA}{\int_A dA} \quad (5.7)$$

Under turbulent flow conditions, the  $\Delta P$  across the entry ( $P_{in}$ ) and exit ( $P_{out}$ ) of the cooling plate is obtained as:

$$\Delta P = P_{in} - P_{out} \quad (5.8)$$

A rectangular cross-section GMF Tesla valve with a hydraulic diameter,  $D_h$ , of 1.57 mm is investigated, as shown in Fig.5.1(a). Usually, the functionality of the Tesla valve is determined by pressure diodicity,  $Di$ , which is a proportion of the pressure differential

around the valve in reverse and forward directions for a specific velocity (Thompson *et al.* 2015).

$$Di = \frac{\Delta P_r}{\Delta P_f} \bigg|_{\omega} \quad (5.9)$$

Higher the value of  $Di$ , more significant is the fluid movement in the forward flow direction. In general, the  $Di$  value for microscale Tesla valve ranges from 1 to 2, whereas for macro scale, the value reaches higher orders of 4 due to the implication of dynamic flow or larger  $Re$ .

### 5.2.6 Validation of the model

Due to the limitation of an experimental study on an MSTV design as a mini-channel cooling plate, a 3D micro GMF Tesla valve is designed as per the dimensions of Gamboa *et al.* (2005). The authors conducted experiments by varying the  $Re$  from 500 to 2000. Based on the literature available on a micro-scale Tesla valve design (Thompson *et al.* 2013; Thompson *et al.* 2015; Porwal *et al.* 2018), it is observed that laminar flow conditions would exist only for  $Re \leq 300$  and the flow reaches into early stages of the transitional regime for  $Re \geq 300$ . Hence, a turbulent flow solver is adopted to validate numerical results with the experimental data. Table 5.2 compares the  $Di$  value calculated from the simulation of MSTV with forward and reverse flows and the experimental data obtained from Gamboa *et al.* (2005). A good agreement between the experimental and numerical data is observed with a maximum deviation of 7% for  $Re$  ranging from 500 to 2000. Moreover, it is seen that the  $Di$  upsurges with an increase in  $Re$  for both cases. A slight discrepancy is observed

between the  $Di$  values for  $Re$  of 500 and 1000, which can be attributed to the absence of either instrumental error or real-world losses in the numerical procedure.

Table 5.2: Comparison of numerical results with experimental results of (Gamboa *et al.* 2005)

$Re$	Experimental ( $Di$ )	Simulation ( $Di$ )	Relative error (%)
500	1.48	1.37	7.1
750	1.48	1.43	3.2
1000	1.58	1.47	6.5
1200	1.56	1.51	3.4
1500	1.58	1.54	2.3
1750	1.64	1.57	4.5
2000	1.61	1.59	1.3

### 5.2.7 Grid independence test

For selected test cases, a rigorous grid sensitivity test is performed. However, a particular case of grid independence test is reported in which the cold plate is embedded with 3-channelled MSTV. The corresponding width and depth of the channel are 3.648 mm and 1 mm, respectively, while  $Re$  is 2500. A free tetrahedral mesh is used for the construction of mesh (Fig. 5.2).

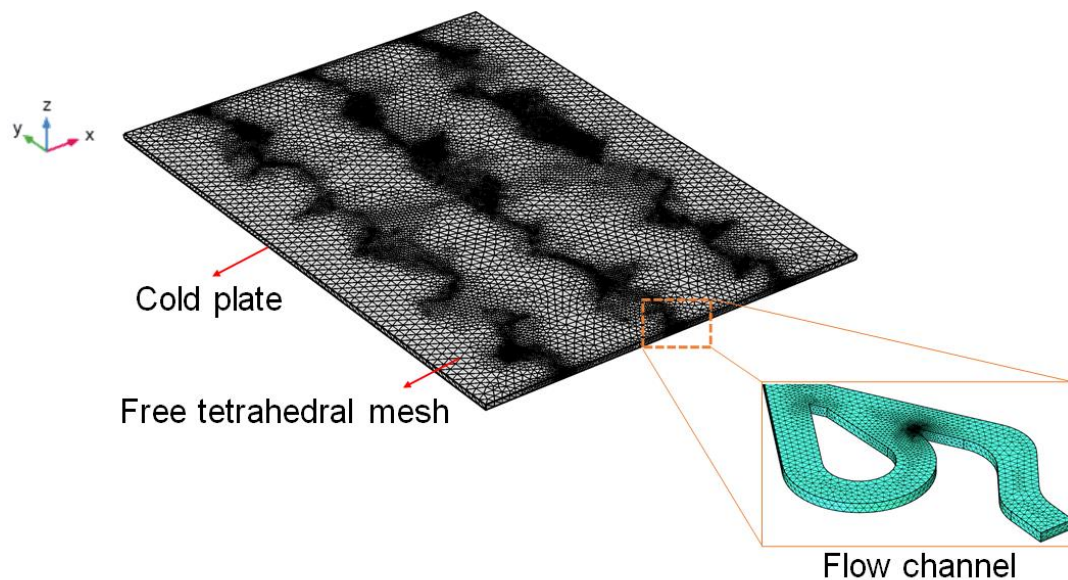


Fig. 5.2: Mesh model of the cold plate



Three different mesh sizes are adopted, where the cold plate's minimum element size is altered as 4.66 mm, 3.64 mm, and 2.95 mm, respectively. At the same time, the flow channels minimum element size varies to 0.5 mm, 0.4 mm, and 0.3 mm, called Mesh 1, Mesh 2, and Mesh 3, respectively. Considering Mesh 3, the  $Di$  is found to be 3.17, whereas, for Mesh 1 and Mesh 2, the  $Di$  is noticed to be 3.10 and 3.16, respectively. The overall deviation in  $Di$  is observed to be less than 0.36% for Mesh 2, where the minimum element size of the cold plate and flow channels are 3.64 mm and 0.38 mm, respectively. Considering computational time and accuracy of results, Mesh 2 is selected for further investigations. For this, the total number of nodes is noticed to be 29,71,328.

## 5.3 Results and discussion

This section investigates the influence of different structural parameters such as channel number, the distance between two consecutive valves, channel width, outer curve radius and valve angle for different  $Re$  and a constant heat flux calculated for a battery discharge rate of 2C. The simulation results are discussed elaborately in the following six subsections.

### 5.3.1 Comparison of straight channel design with MSTV forward and reverse flow directions

A cold plate's primary role is to remove the heat dissipating from batteries and maintain homogenous temperature distribution across the active area. Before analyzing the influence of structural parameters on the cold plate's performance, preliminary simulations are conducted to compare the effectiveness of forward and reverse flow direction in MSTV

(number of stages,  $N = 10$ ) with a straight channel design under constant flow volume. All simulations are performed for  $Re$  ranging from 2500 to 5500 while imposing an adiabatic condition on the cold plate's outer walls.

Fig. 5.3 provides the comparison of maximum temperature,  $T_{max}$ , and temperature deviation,  $T_{\sigma}$ , for MSTV and straight channel designs. It is evident that the  $T_{max}$  and  $T_{\sigma}$  decreases asymptotically for both forward and reverse flow directions in MSTV as the  $Re$  increases, while a more considerable reduction is observed in reverse flow MSTV. For  $Re$  of 5500,  $T_{max}$  is reduced significantly with the reverse flow compared to that of forward flow in MSTV and straight channel design by 3.6 °C and 6 °C, respectively. This implies that the reverse flow pattern in MSTV is exceptionally effective in transferring heat along the flow path. This flow behaviour is anticipated due to the complex flow characteristics, including impingement and secondary flows, enhancing the local heat transfer coefficient and fluid mixing. Comparatively, the  $T_{max}$  and  $T_{\sigma}$  decline more gradually along the channel length of straight channel design, resulting in a lower heat transfer rate than those within MSTV.

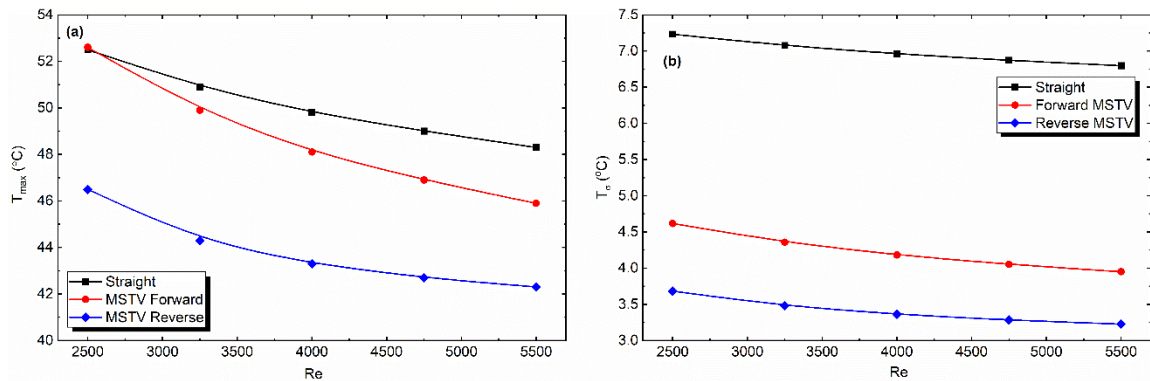


Fig. 5.3: Variation of (a)  $T_{max}$  and (b)  $T_{\sigma}$  across straight channel design, forward and reverse flow direction in MSTV

The pressure difference,  $\Delta P$ , and average temperature,  $T_{avg}$ , of straight channel design, forward and reverse flow directions in MSTV for different  $Re$ , are reported in Table 5.3. With an increase in  $Re$ ,  $\Delta P$  increases enormously, while a substantial reduction in temperature is seen in all the channel designs considered. This indicates that  $Re$  significantly influences pressure loss across the cold plate. The  $\Delta P$  for a straight channel is found to be lowest, while forward and reverse flow in MSTV results in a more significant  $\Delta P$ , specifically for reverse flow. This phenomenon is anticipated, as a Tesla valve is devised to induce high-pressure loss in reverse flow direction as a result of the minor losses at each valve's entry and exit in MSTV.

Table 5.3: Comparison of straight channel design, forward and reverse direction in MSTV at varying  $Re$

$Re$	$T_{avg}$ (°C)			$\Delta P$ (kPa)		
	Straight channel	Forward MSTV	Reverse MSTV	Straight channel	Forward MSTV	Reverse MSTV
2500	37.75	39.11	34.72	5.01	23.6	75.1
3250	36.59	37.05	33.26	7.94	40.2	131
4000	35.83	35.71	32.33	11.4	61.0	204
4750	35.28	34.75	31.67	15.3	85.9	291
5500	34.87	34.03	31.20	19.8	115	393

A significant criterion for assessing heat transfer augmentation is by evaluating the fluid flow inside a cooling plate. An improved fluid flow could initiate and impede boundary layer growth near the solid surface in a cooling plate. This effect enhances the fluid flow motion and, as a result, dramatically improves heat transmission (Om *et al.* 2018). Hence, it is advantageous to consider the mechanism of the flow field for analyzing the heat transfer characteristics inside a cooling plate. Fig. 5.4 exhibits the pressure, velocity, and temperature contours of straight and MSTV channel designs of forward and reverse direction along the cold plate's half-depth plane for  $Re$  of 4000.

It is apparent that MSTV provides higher pressure loss along forward and reverse flow directions than straight channel design. In both forward and reverse flow directions, the major pressure loss is attributable to viscous forces in the channel segments preceding Tesla valves, as shown in Fig. 5.4. In the forward flow direction, the minor pressure loss is primarily the effect of flow disruption caused by the region *iii* between Tesla valves, enabling a linear pressure profile (Fig. 5.5a). Also, the pressure loss in forward flow is always lower than in reverse flow, indicating MSTV's fluidic diode effect. The non-linearity in pressure loss across reverse flow direction is attributable to minor losses in region *ii* and region *iii* at each Tesla valve's entry and exit, respectively (Fig. 5.5b) (Porwal *et al.* 2018).

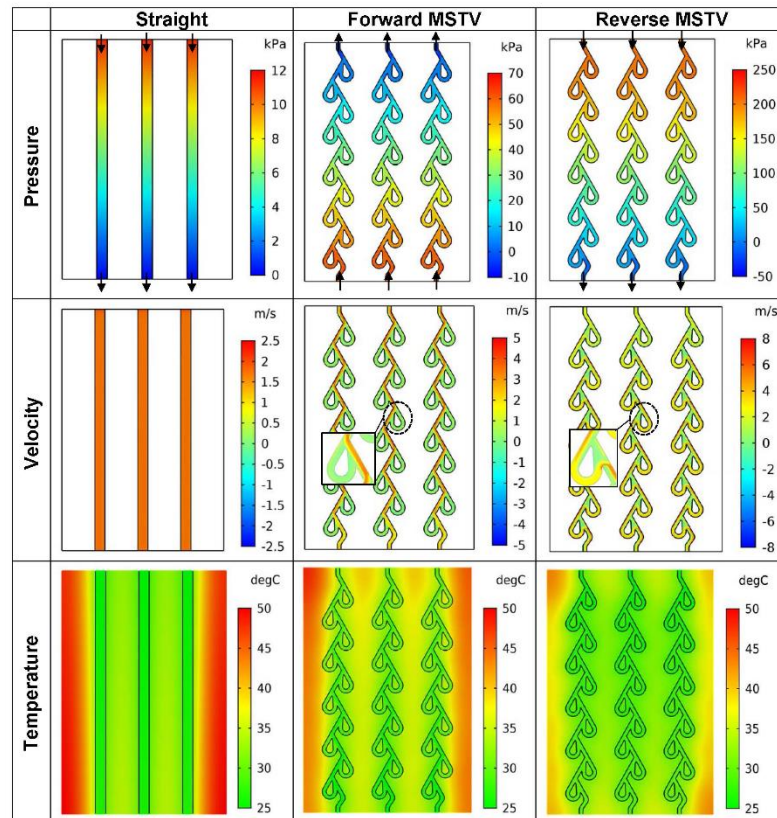


Fig. 5.4: Pressure, velocity and temperature contours for straight channel design, forward and reverse flow direction in MSTV for Re of 4000

Whereas the velocity profile is similar throughout the channel length for each selected case. Compared to conventional straight channel design, the heat transfer capability of MSTV forward flow design is improved. This is primarily due to the formation of vortices in region *ii*, leading to secondary flows at each Tesla valve's entry and exit, where flow splitting occurs despite an enhanced surface area (Fig. 5.5a).

A more dynamic flow phenomenon is observed in the reverse flow of the MSTV design. High velocities prevail between adjacent valves during reverse flow, while low velocities exist at each Tesla valve's entry and exit due to jet impingements. The maximum velocity is also considerably higher in the recirculation region caused by jetting effects (Thompson *et al.* 2015; Porwal *et al.* 2018). An additional augmentation in heat transfer rate is noticed due to the flow bifurcation and mixing mechanisms in region *iii* along each valve's exit, resulting in a secondary flow (Fig. 5.5b). Besides this, negative velocities are observed in the forward and reverse flow of MSTV. This is mainly due to the circulation of coolant in the corner adjacent to each Tesla valve's outlet due to 3D flow turning, leading to complex secondary flow characteristics within the shear layer (Thompson *et al.* 2015).

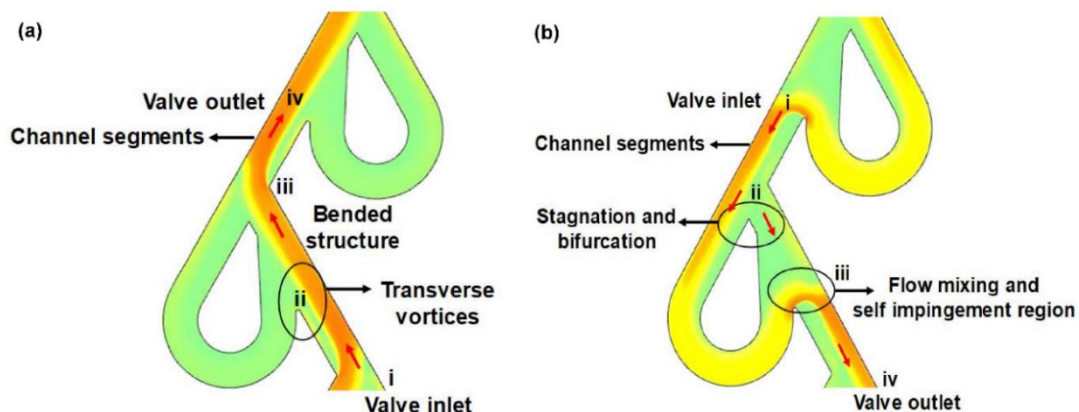


Fig. 5.5: Closer view of velocity contours at  $Re = 4000$  (brighter colour: high velocity, lighter colour: low velocity) encountered in (a) forward flow MSTV, and (b) reverse flow MSTV

In parallel, higher temperature regions are more along the edges, while lower temperature regions are distributed equally along the flow region of all designs (Fig. 5.4). In straight channel design,  $T_{\max}$  corresponds to 49.14 °C on the right side of the cold plate, respectively. While, in the forward and reverse flows,  $T_{\max}$  is 47.56 °C and 42.86 °C on the upper-left edge of the cold plate, respectively. Comparatively, hot spots are higher in straight channel design than reverse and forward flow in MSTV. Thus, it can be comprehended that the MSTV design provides a lower temperature rise and is more efficient than straight channel design at the cost of  $\Delta P$ . However, a balance must be maintained between  $T_{\max}$  incremental tolerance and pressure drop.

From the results mentioned above, it can be reckoned that reverse flow in MSTV provides effective cooling despite a higher  $\Delta P$ . Hence, it is used to evaluate the impact of different parameters on the cold plate's thermal and hydraulic behaviour in further simulations.

### 5.3.2 Effect of channel number

To assess the cooling proficiency of the cold plate with reverse flow MSTV design, the channel number is pre-set to 2, 3 and 4. The flow channels are equally spaced along with the cold plate's width and length directions.

Fig. 5.6 shows the comparison of  $T_{\max}$  and  $T_{\sigma}$ , for reverse flow in MSTV by varying number of channels in the cold plate at different  $Re$ . As the  $Re$  increases from 2500 to 5500,  $T_{\max}$  falls by 6.3 °C, 4.2 °C and 3.2 °C with 2, 3 and 4 number of channels, respectively. Concurrently,  $T_{\sigma}$  is improved by 5.28%, 12.39% and 22.17% with 2, 3 and 4 number of channels, respectively. From Fig. 5.6, it is evident that the cold plate with 4 number of

channels exhibited the lowest  $T_{\max}$  and enhanced  $T_{\sigma}$  for all  $Re$  values compared to other designs. For 4 number of channels with  $Re$  of 2500,  $T_{\max}$  is reduced by 27.4 °C and 8.2 °C, while  $T_{\sigma}$  is augmented by 80.96% and 50.98% when compared to 2 and 3 number of channels, respectively. With an increase in  $Re$  to 5500 for 4 number of channels,  $T_{\max}$  is decreased by 24.3 °C and 7.2 °C, whereas  $T_{\sigma}$  is improved by 84.35% and 56.45% when compared to 2 and 3 number of channels, respectively. This indicates that a cold plate comprising a greater channel number exhibits a lower temperature rise and retains homogenous temperature distribution due to increased heat transfer area.

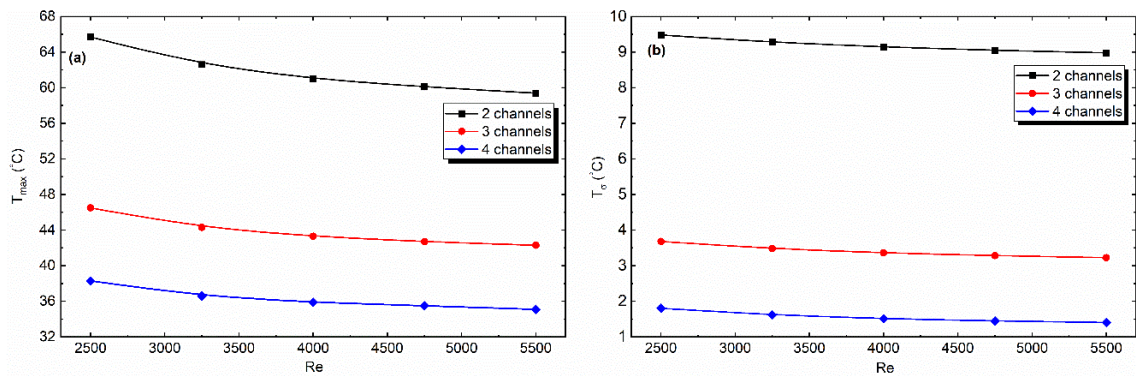


Fig. 5.6: Comparison of (a)  $T_{\max}$  and (b)  $T_{\sigma}$  across reverse flow direction in MSTV for varying channel number

It is seen from Table 5.4 that the values of  $\Delta P$  and  $T_{\text{avg}}$  reduce with an increase in channel number from 2 to 4. For instance, with  $Re$  of 2500,  $\Delta P$  for 2 channels is 75.9 kPa, which is reduced to 73.6 kPa with an increase of channel number to 4. Similarly, for  $Re$  of 5500,  $\Delta P$  is reduced by 4.52% with the alteration of channel number from 2 to 4. Although there is a considerable reduction  $T_{\text{avg}}$ , a minimal change in  $\Delta P$  is seen with the amplification of channel number.

Table 5.4: Performance of reverse flow direction in MSTV for different design parameters

Parameter	Variation	<i>Re</i>									
		2500		3250		4000		4750		5500	
		$T_{avg}$ (°C)	$\Delta P$ (kPa)	$T_{avg}$ (°C)	$\Delta P$ (kPa)	$T_{avg}$ (°C)	$\Delta P$ (kPa)	$T_{avg}$ (°C)	$\Delta P$ (kPa)	$T_{avg}$ (°C)	$\Delta P$ (kPa)
<b>Channel number</b>	2 channels	45.29	75.9	43.06	132.8	41.63	209	40.63	294	39.88	398
	3 channels	34.72	75.1	33.26	131	32.33	203.7	31.67	291	31.2	393
	4 channels	31.06	73.6	29.98	129	29.31	199	28.84	283	28.48	380
<b>Valve to valve distance (G)</b>	4.41 mm	31.75	83.04	30.63	143	29.92	291	29.42	310	29.05	416
	5.88 mm	31.48	79.5	30.38	137.6	29.68	211.3	29.19	299	28.83	401
	7.35 mm	31.33	76.9	30.16	133	29.47	205.7	28.99	292	28.64	392
	8.82 mm	31.06	73.6	29.99	129	29.31	199	28.84	283	28.48	380
<b>Channel width (<math>W_c</math>)</b>	3.04 mm	31.65	71.037	30.48	123	29.74	189.44	29.23	270.3	28.85	366.57
	3.65 mm	31.11	68.45	30.04	117.82	29.35	180.2	28.88	255.86	28.53	344.63
	4.26 mm	30.48	67.73	29.52	115.67	28.91	175.98	28.48	248.99	28.17	334.71
	4.86 mm	30.06	61.13	29.18	103.89	28.62	157.52	28.23	222.19	27.94	298
<b>Curve radius (R)</b>	5.86 mm	31.78	68.65	30.66	118.09	29.94	180.71	29.44	256.6	29.07	348.65
	7.05 mm	31.11	68.45	30.04	117.82	29.35	180.2	28.88	255.86	28.53	344.63
	8.23 mm	30.59	65.67	29.55	113.16	28.9	173.2	28.44	246.1	28.1	331.65
	9.4 mm	30.15	64.12	29.16	110.52	28.35	169.18	28.1	240.23	27.78	323.8
<b>Valve angle (<math>\theta</math>)</b>	40.8°	30.47	67.822	29.46	116.84	28.82	178.76	28.37	253.65	28.04	341.45
	41.6°	30.59	65.674	29.55	113.16	28.9	173.2	28.44	246.1	28.1	331.65
	42.4°	30.62	64.716	29.59	111.44	28.94	170.6	28.48	242.34	28.15	326.69
	43.32°	30.86	62.252	29.81	107.03	29.15	163.6	28.68	232	28.34	312.94



The temperature variation across the cold plate's half-depth plane exhibits a spread-out area of low temperature along the coolant flowing path, as shown in Fig. 5.7. It can be noted that the coolant carries away a greater amount of heat and reduces high-temperature regions with an increase in the channel number. Alongside, this phenomenon reduces the weight of the overall cooling system. For  $Re$  of 4000, it is seen that when the channel number is 2, the hot spot regions are higher on the cold plate's lower right edge, and the corresponding  $T_{max}$  is 60.05 °C. This gradually reduces to 35.09 °C as the channel number increases to 4.

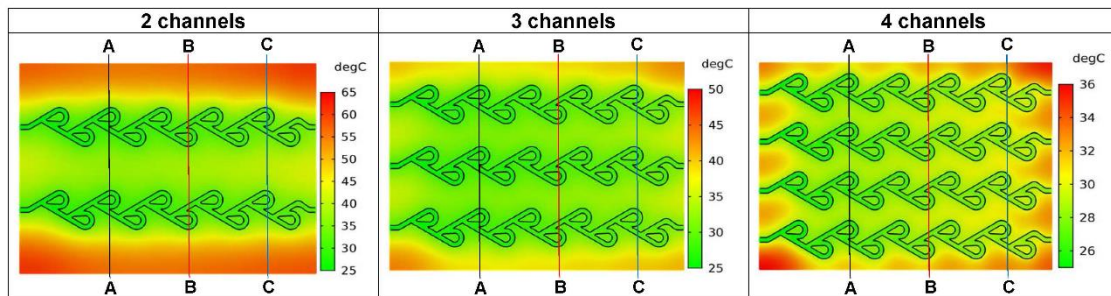


Fig. 5.7: Evolution of temperature contours for reverse flow direction in MSTV at  $Re$  4000 for varying channel number

For a clear view, three different cross-sections in the  $y$ -direction of the cooling plate A-A, B-B, and C-C at a distance from the extreme left of 56.75 mm, 113.5 mm and 170.25 mm are considered, and the temperature profiles at each location are plotted along the  $x$ -direction (0 to 160 mm) for a  $Re$  of 4000 in Fig. 5.8. The temperature distribution at each location is mainly due to the profile of MSTV design and the corresponding velocity distribution. It can be noticed that temperature rise is maximum at location C-C than others. This occurs because high-heat regions are distributed mainly downstream of the cooling plate. For 2 channels, at  $x = 40$  mm, the temperature difference between the locations B-B and A-A, C-C and B-B is noticed to be 7.24 °C and 0.79 °C, respectively. As the channel number is increased to 4, the temperature difference between the locations B-B and A-A, C-C and B-B are reduced by 0.35 °C and 1.01 °C, respectively. For location A-A, at  $x = 0$

mm, the  $T_{\max}$  of 4 channels is observed to be 25.64 °C and 7.23 °C less than 2 and 3 channels, respectively. While at  $x = 160$  mm,  $T_{\max}$  is reduced by 24.35 °C and 6.73 °C when compared to 2 and 3 channels, respectively. A similar pattern is noticed at locations B-B and C-C. Overall, the temperature rise is seen to reduce with an increase of number of channels, which is analogous to the results of Fig. 5.7. Hence, the data specifies that a cold plate with 4 channels exhibits superior performance and enhances the heat dissipation efficacy of the liquid cooling system for all  $Re$ .

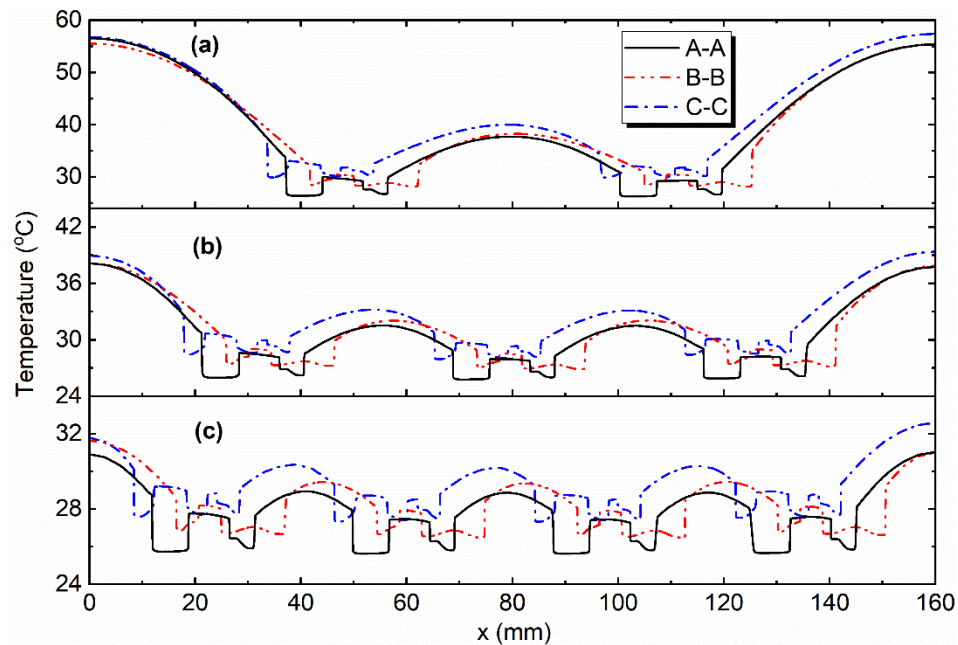


Fig. 5.8: Temperature profiles in the x-direction of cooling plate at different locations for (a) 2 channels, (b) 3 channels and (c) 4 channels

### 5.3.3 Effect of valve-to-valve distance

Restraining the number of stages  $N$  to 10 and considering 4-channelled reverse flow MSTV design, the distance between consecutive valves is varied as 4.41 mm, 5.88 mm, 7.35 mm, and 8.82 mm, whereas the other dimensions in the design remain unchanged. Fig. 5.9

shows the comparison of  $T_{\max}$  and  $T_{\sigma}$  for reverse flow in MSTV by altering valve to valve distance,  $G$ .

For  $Re$  of 2500, as  $G$  varies from 4.41 mm to 8.82 mm, the  $T_{\max}$  reduces by 3.6 °C, while  $T_{\sigma}$  improves by 31.19%, simultaneously. With an increase in  $Re$  to 5500,  $T_{\max}$  falls by 2.1 °C, while  $T_{\sigma}$  enhances by 33.02%. These results specify that an increase in  $G$  improves the cooling capability substantially. In addition, a significant difference in the rise of  $\Delta P$  and  $T_{\text{avg}}$  is seen with the increasing value of  $G$  (Table 5.4). With  $G$  of 8.82 mm, the  $\Delta P$  reaches minimum of 380 kPa, whereas it attains a maximum of 416 kPa for  $G$  of 4.41 mm. A similar variation in  $\Delta P$  is also observed for variation of  $Re$ . With  $Re$  of 5500,  $\Delta P$  is reduced by 8.65% with  $G = 8.82$  mm compared to that of  $G = 4.41$  mm. This indicates that the influence of reducing  $G$  value is relatively low on the cold plate's thermal performance. This can be ascribed to the increased heat transfer area with  $G$  value. Alongside, the structural strength of the channel design weakens with decreasing  $G$ .

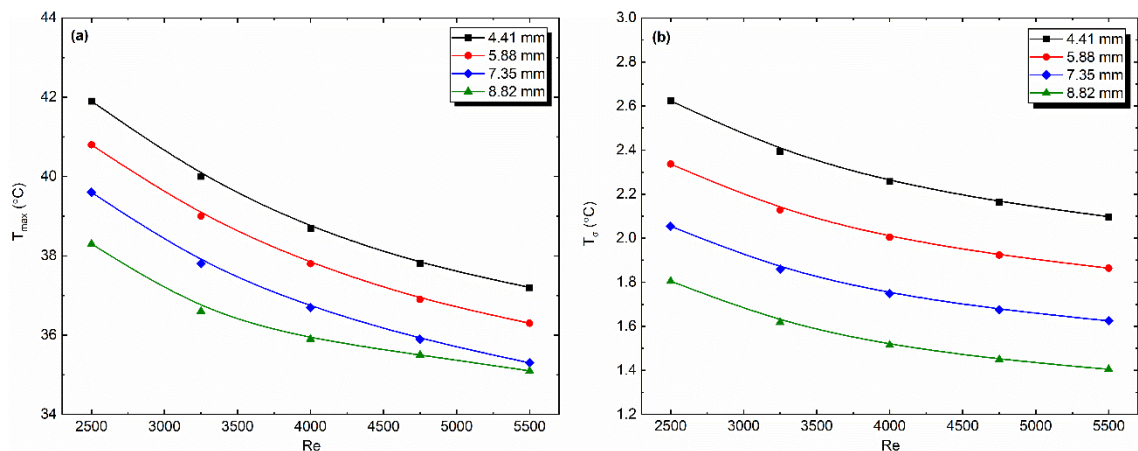


Fig. 5.9: Comparison of (a)  $T_{\max}$  and (b)  $T_{\sigma}$  across 4-channelled cold plate with reverse flow direction in MSTV for varying  $G$

### 5.3.4 Effect of channel width

In general, a wider channel facilitates more heat transfer area and enables high cooling capacity. Keeping this in view, the channel width,  $W_c$  of the MSTV design is varied as 3.04 mm, 3.65 mm, 4.26 mm, and 4.86 mm to examine its impact on the cooling plate's performance. Whereas, the number of stages, outer curve radius and valve angle in the MSTV design remain unaltered as 10, 7.05 mm, and  $41.6^\circ$ , respectively. The effect of  $W_c$  on the  $T_{\max}$ , and  $T_\sigma$  of the cold plate as a function of  $Re$  is reported in Fig. 5.10.

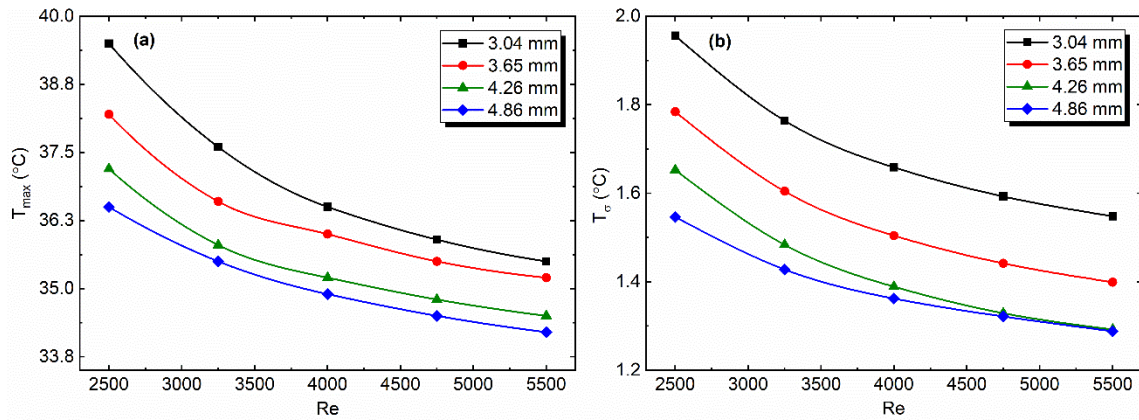


Fig. 5.10: Variation of (a)  $T_{\max}$  and (b)  $T_\sigma$  across MSTV cold plate with reverse flow for different  $W_c$  and  $Re$

The  $T_{\max}$  and  $T_\sigma$  reduce with a rise of  $Re$  for all selected  $W_c$ . Simultaneously, a significant change in temperature rise and corresponding deviation is seen with the increase of  $W_c$ . For a  $Re$  of 2500, as  $W_c$  alters from 3.04 mm to 4.86 mm, the  $T_{\max}$  decreases by  $3^\circ\text{C}$ , while  $T_\sigma$  enriches by 20.92% at the same time. With the increase of  $Re$  to 5500,  $T_{\max}$  decreases by  $1.3^\circ\text{C}$ , while  $T_\sigma$  enhances by 16.77%. However, the change in  $T_{\max}$  is seen to be minimal as  $W_c$  varies from 4.26 mm to 4.86 mm i.e.,  $0.3^\circ\text{C}$ , as the  $Re$  exceeds 3250. Similarly, the change in  $T_\sigma$  is noticed to be insignificant as the  $Re$  exceeds 4750. To be

specific, even if the coolant's available heat transfer area increases with varying  $W_c$ , its effect on  $T_{\max}$  and  $T_{\sigma}$  is negligible with an increase of  $W_c$  from 4.26 mm to 4.86 mm at higher  $Re$ .

The  $\Delta P$  varies inversely with  $Re$ , whereas a linear relation is seen between  $T_{avg}$  and  $Re$  for the same  $W_c$  due to the increase in available heat transfer area (Table 5.4). Greater the  $Re$  is, larger the  $\Delta P$  difference in the MSTV. As a result, an increasing  $W_c$  can considerably reduce  $\Delta P$ . If the  $W_c$  of the channel is too narrow (3.04 mm), the  $\Delta P$  is seen to be higher when compared to a channel with larger  $W_c$  of 4.86 mm irrespective of  $Re$ . For a given  $Re$  of 5500, as the  $W_c$  varies from 3.04 mm to 4.86 mm, the  $\Delta P$  across the MSTV and  $T_{avg}$  reduce by 18.71% and 3.15% respectively. Moreover, for the same  $Re$ , the difference in  $\Delta P$  is seen to reduce by 10.96% while a slight enhancement of 0.82% is seen in the  $T_{avg}$ , as the  $W_c$  is amplified from 4.26 mm to 4.86 mm.

A closer view of velocity and pressure distributions on the central  $xy$  plane of the cooling plate with MSTV design for varying  $W_c$  when  $Re$  is 4000 are plotted, and the results are exhibited in Fig. 5.11. A similar variation in pressure and velocity distributions is noticed for varying  $W_c$ . As seen in Fig. 5.11, flow from the straight and bent channel converges, resulting in coolant impingement onto the wall with a high velocity, which causes a recirculation zone to form at region *iii* (Z. jiang Jin *et al.* 2018) leading to a low-pressure zone. Moreover, the pressure is noticed to be greater in the straight channel when compared with the bent channel. This can be attributed to another recirculation zone formed at region *ii* due to the abrupt shift in the flow direction. However, for a larger width, i.e., 4.86 mm,

the pressure difference within the channel is seen to be smaller. This is mainly attributable to the coolant flowing mostly into the bent channel, which results in more impingements due to an increase in cross-sectional area at a larger width. Aside from that, negative pressures and velocities are seen in the MSTV design, as there is an out-of-plane circulation at each Tesla valve's outlet. This is caused by 3D flow turning, which results in an intricate secondary flow pattern within the shear layer (Thompson *et al.* 2015).

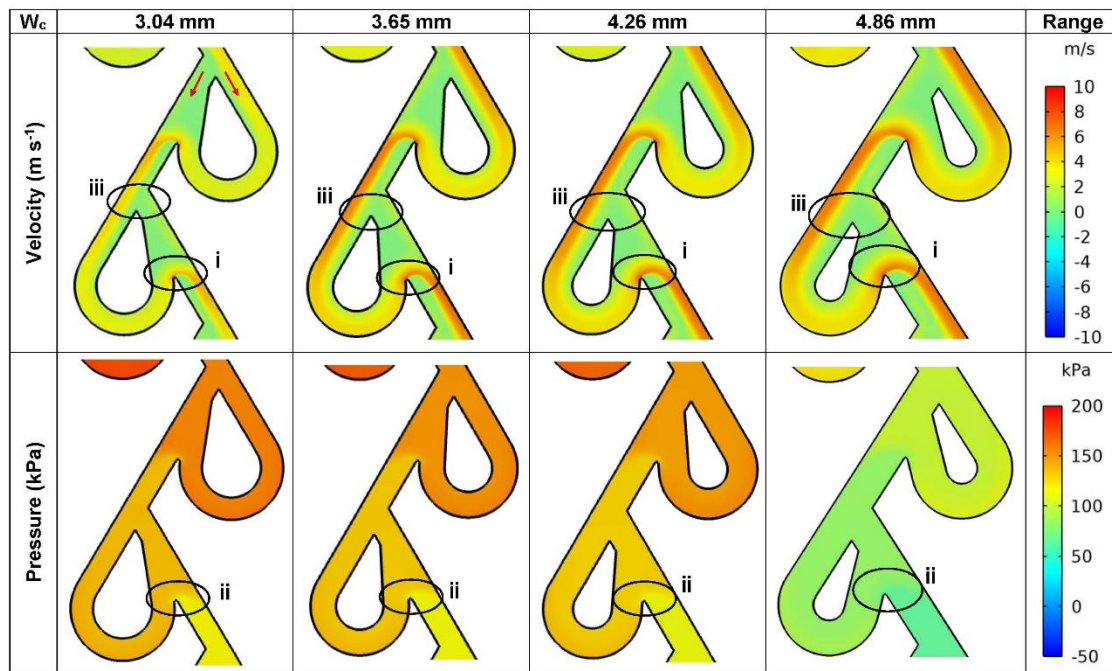


Fig. 5.11: A closer view of velocity and pressure contours on the central xy plane of cooling plate for varying  $W_c$  at a  $Re$  of 4000

In brief, it can be stated that a lower  $W_c$  exhibits a higher  $\Delta P$  and  $T_{max}$ , while an insignificant change in  $T_{max}$  and  $T_\sigma$  is seen with  $W_c$  greater than 4.26 mm. Hence, a balance must be maintained between thermal and hydraulic performance while choosing an optimal  $W_c$  in the cooling plate.

### 5.3.5 Effect of outer curve radius

Four different values of the outer curve radius,  $R$ , are selected to analyze the cooling plate's performance further. While the number of stages, channel width, and valve angle in the MSTV design are maintained constant at 10, 3.65 mm, and  $41.6^\circ$ , respectively. The effect of  $R$  on the  $T_{\max}$ , and  $T_\sigma$  of the cooling plate as a function of  $Re$  is exhibited in Fig. 5.12.

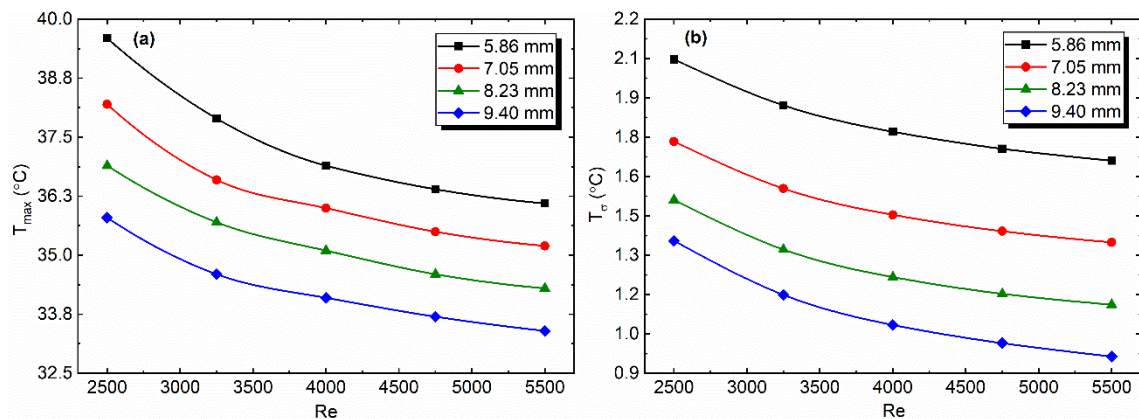


Fig. 5.12: Variation of  $T_{\max}$  and  $T_\sigma$  across MSTV cold plate with reverse flow for different  $R$  and  $Re$

As the  $Re$  alters from 2500 to 5500,  $T_{\max}$  drops by 3.5 °C, and 3 °C, with  $R$  of 5.86 mm and 7.05 mm, respectively. While  $T_{\max}$  reduces by 2.6 °C and 2.4 °C with  $R$  of 8.23 mm, and 9.4 mm, respectively. Alongside,  $T_\sigma$  is improved by 18.44%, 21.59%, 25.60%, and 31.42% with 5.86 mm, 7.05, 8.23, and 9.4 mm, respectively. From Fig. 5.12 it is apparent that a minimum rise in  $T_{\max}$  and  $T_\sigma$  is exhibited by a  $R$  of 9.4 mm, while the maximum rise is seen with  $R$  of 5.86 mm, for all  $Re$ . For a  $R$  of 9.4 mm and  $Re$  of 2500,  $T_{\max}$  is reduced by 3.8 °C, 2.4 °C, and 1.1 °C while  $T_\sigma$  is improved by 32.99%, 21.22%, and 9.99% when compared to 5.86 mm, 7.05 mm, and 8.23 mm, respectively. With a rise in  $Re$  to 5500 for  $R$  of 9.4 mm,  $T_{\max}$  is decreased by 2.7 °C, 1.8 °C, and 0.9 °C whereas  $T_\sigma$  is enhanced by

43.65%, 31.10%, and 17.03%, respectively. It can be noted that increasing the  $R$  in Tesla valve linearly lowers the peak temperature and deviation within the cooling plate.

Table 5.4 shows the variation in  $\Delta P$  and  $T_{avg}$  across the cooling plate for different  $R$  and  $Re$ . It can be seen that with an increase of  $R$ , the  $\Delta P$  and  $T_{avg}$  reduce linearly for any larger  $Re$ . The difference in  $\Delta P$  with increasing  $R$  is marginal as  $Re$  is less than 4750. For a particular  $R$  (say 5.86 mm), with the increase in  $Re$  from 2500 to 5500, the  $\Delta P$  increases by 5 times while  $T_{avg}$  reduces by 8.53%. For a  $Re$  of 2500 and 5500, as the  $R$  alters from 5.86 mm to 9.4 mm, the  $\Delta P$  reduces by 6.59% and 7.13% whereas the  $T_{avg}$  reduces by 5.13% and 1.27%, respectively. Although increasing the Tesla valve's  $R$  led to a substantial variation in  $T_{max}$  and  $T_{\sigma}$ , it showed a marginal change in reducing  $\Delta P$  across the cooling plate.

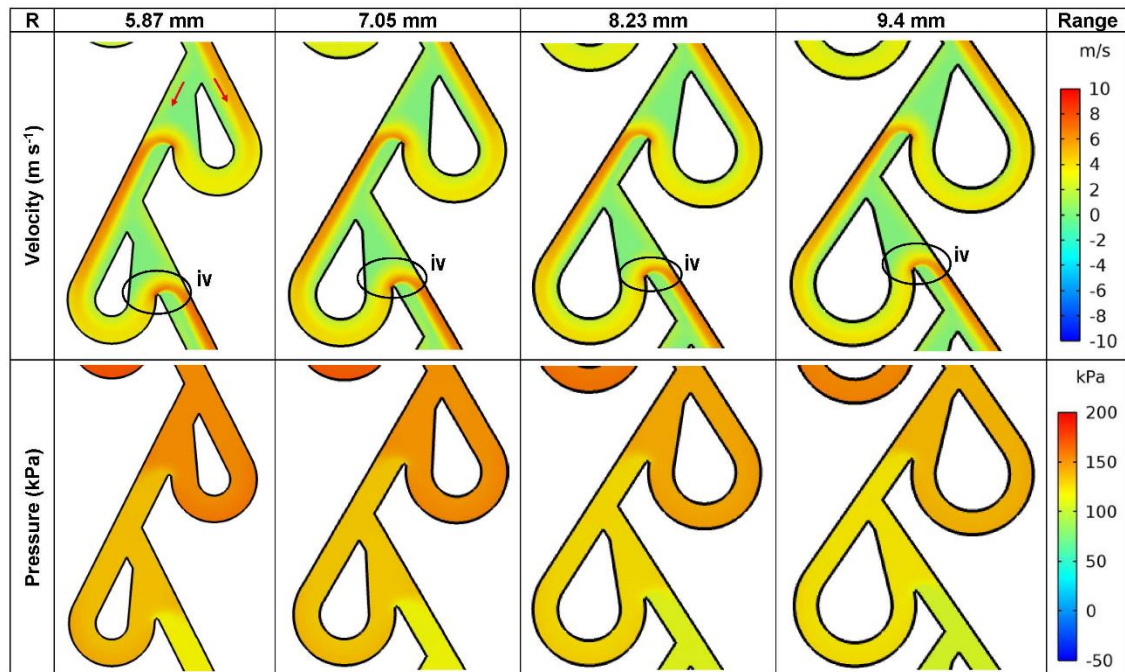


Fig. 5.13: A closer view of velocity and pressure contours on the central  $xy$  plane of cooling plate for varying  $R$  at a  $Re$  of 4000



Fig. 5.13 shows the closer view of velocity and pressure distributions on the central  $xy$  plane of the cooling plate with MSTV design for varying  $R$  with  $Re$  of 4000. A similar variation in pressure and velocity distribution is seen for different  $R$ . On comparing Fig. 5.11 and Fig. 5.13, it is noticed that due to a ridge in the straight channel, a large portion of the coolant flows from the entry with a high velocity through the bent channel. With a rise in  $R$ , the coolant interaction inside the bent and straight channels reduces, thereby decreasing the peak velocity and jet impingement behind the bent channel (region *iii*). Consequently, the pressure loss in the Tesla valve with a smaller  $R$  is larger. For a smaller  $R$ , the pressure is higher in the bent and straight channels. On the contrary, when  $R$  increases, the pressure in the straight channel is greater than that of the bent channel. This phenomenon is mainly due to the reduced interaction of confluence. Most of the pressure losses occur behind bent channels due to the formation of jet impingement and recirculation zone in that particular region. A pressure reduction occurs at each stage of MSTV, followed by a recovery process. However, the reclaimed pressure is lesser than the preceding pressure. As the coolant flows towards the exit, the pressure drops even more, and the lowest pressure is reached at the last stage, i.e.,  $N=10$  (Qian *et al.* 2019).

An optimal channel design reduces temperature escalation and enhances the homogeneity of temperature distribution. The temperature profiles for varying  $R$  on the central  $xy$  plane of the cooling plate for  $Re$  of 4000 are depicted in Fig. 5.14. This illustrates that all four pictures have the common aspect of diverse high-heat regions spread over the cold plate edges. In general, low-temperature regions are found in a valve with a high-velocity zone. For the same  $R$ , a marginal temperature variation can be seen in the bent channel due to the difference in the flow field. As can be seen, the cooling plate's upper-right edge has high

heat zones, and the associated  $T_{\max}$  is 36.67 °C for a  $R$  of 5.87 mm. The  $T_{\max}$  is gradually reduced to 33.89 °C as the  $R$ -value is increased to 9.4 mm, and the hot spots are seen to reduce simultaneously. This reduction in hot spots with varying  $R$  is mainly due to the difference in velocity distributions as the coolant flows along the MSTV design. These results specify that increasing the  $R$  of the Tesla valve can effectively improve temperature homogeneity.

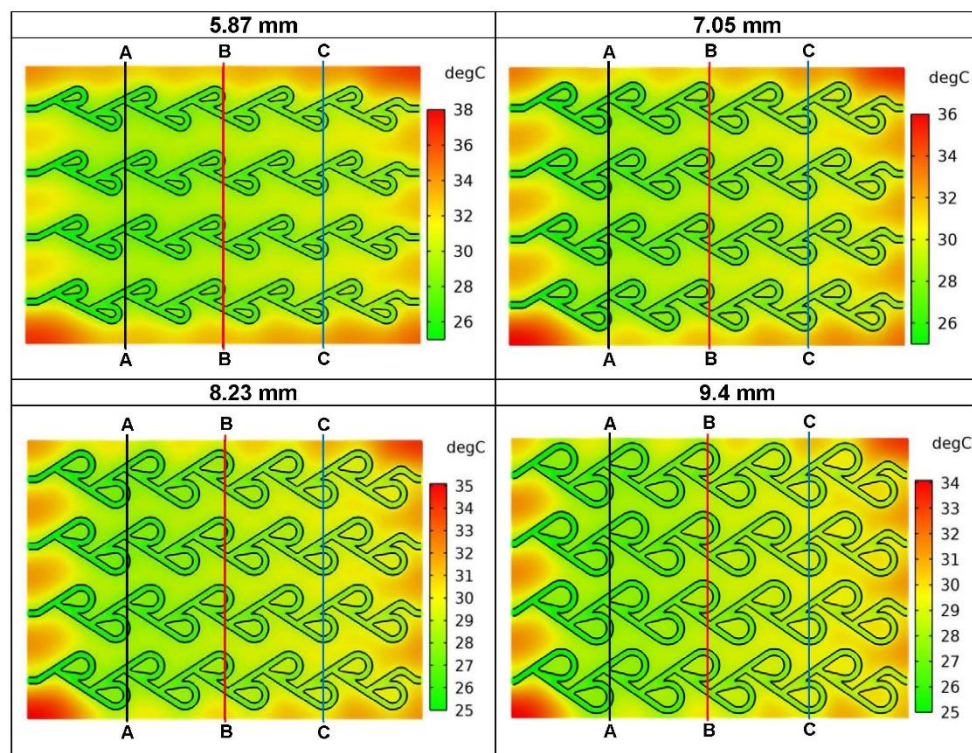


Fig. 5.14: Temperature contours on the central  $xy$  plane of cooling plate for varying  $R$  at a  $Re$  of 4000

The variation in temperature along the  $x$ -direction of the cooling plate for different  $R$  with  $Re$  of 4000 is shown in Fig. 5.15. The temperature contours are obtained at three different locations along the  $y$ -direction, namely at  $y = 56.75$ ,  $113.5$ , and  $170.25$  mm from the left side of the cooling plate, as indicated in Fig. 5.15. All designs exhibit a high temperature at  $x = 0$  and  $160$  mm, as that particular region is at a cold plate edge with lesser cooling. As  $R$  is amplified from 5.87 mm to 9.4 mm, the temperature at locations A-A, B-B, and C-

C ( $x = 0$  mm) are observed to reduce by 4.5 °C, 3.66 °C, and 4.7 °C, respectively. While at  $x = 160$  mm, the temperature is decreased by 4.14 °C, 4.42 °C, and 3.48 °C, respectively. Also, it is apparent from the graph that a temperature difference exists between the locations, and it varies depending on the  $R$  of the Tesla valve. For  $R$  of 5.87 mm and  $x$  of 40 mm, the temperature difference between the locations B-B and A-A is noticed 0.37 °C, whereas it increases to 1.01 °C in the case of B-B and C-C. As  $R$  is increased to 9.4 mm, the temperature disparity between the locations B-B and A-A is decreased by 0.58 °C, and in the case of C-C and B-B, the reduction is 0.73 °C. Similarly, at  $x = 120$  mm, as the  $R$  varies from 5.87 to 9.4 mm, the temperature rise is reduced by 1.71 °C, 1.50 °C, and 1.35 °C at locations A-A, B-B, and C-C, respectively. This temperature difference can be ascribed to the profile of the MSTV design and the corresponding velocity distributions. Hence, it can be concluded that a larger  $R$  of the Tesla valve should be chosen to obtain lower  $T_{\max}$ .

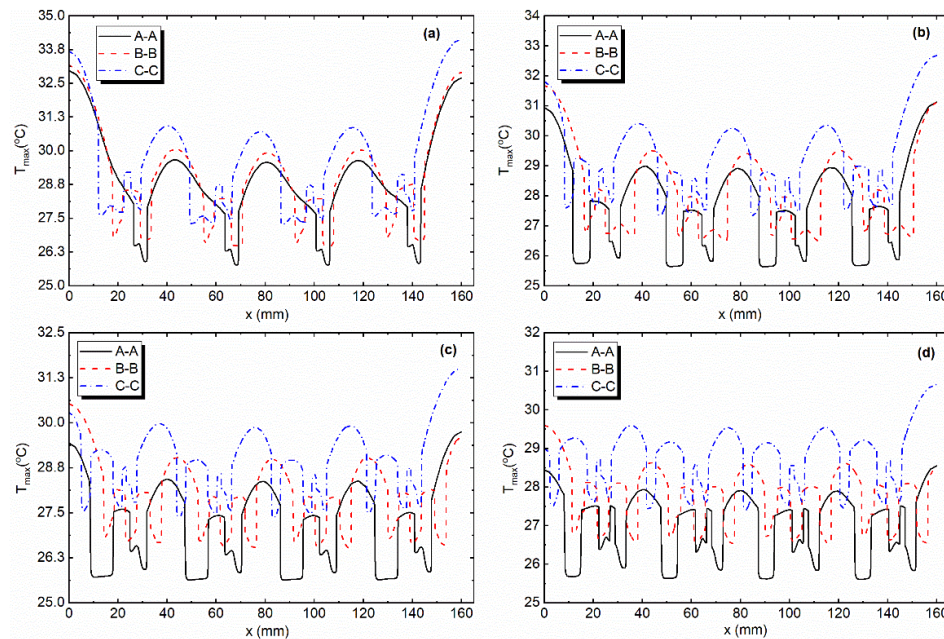


Fig. 5.15: Temperature profiles in the  $x$ -direction at different locations for a  $R$  of (a) 5.87 mm, (b) 7.05 mm, (c) 8.23 mm, and (d) 9.4 mm

### 5.3.6 Effect of valve angle

Four different valve angles,  $\theta$ , are selected to reflect their significance on the functioning of the cooling plate. The other design parameters, including the number of stages, channel width, and outer curve radius in the MSTV design, are set as 10, 3.65 mm, and 8.23 mm, respectively. The effect of  $\theta$  on the  $T_{\max}$ , and  $T_{\sigma}$  of the cooling plate as a function of  $Re$  is displayed in Fig. 5.16.

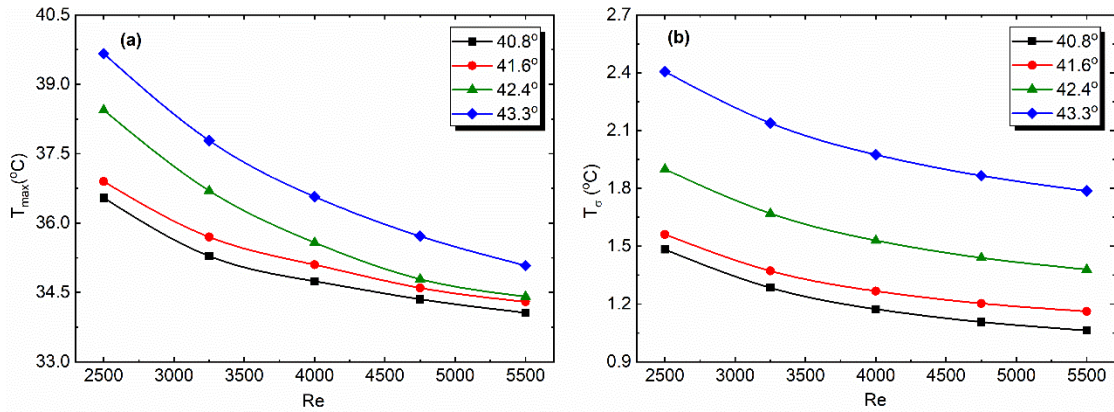


Fig. 5.16: Variation of  $T_{\max}$  and  $T_{\sigma}$  across MSTV cold plate with reverse flow for different  $\theta$  and  $Re$

The  $T_{\max}$ , and  $T_{\sigma}$  of the cooling plate are seen to increase with an increment of  $\theta$ . At the same time, the  $T_{\max}$ , and  $T_{\sigma}$  show a reducing trend with a rise of  $Re$ . It is noticed that at a lower  $Re$  (2500), the  $T_{\max}$  reaches 39.66 °C and  $T_{\sigma}$  is greater than 2 °C for  $\theta$  of 43.3°. However, for the same  $\theta$ , the difference in temperature rise and deviation is seen to reduce as  $Re$  exceeds 4750. For a  $Re$  of 2500, as the  $\theta$  is increased from 40.8° to 43.3°, the  $T_{\max}$  is increased by 3.12 °C. The  $T_{\max}$  is seen to be higher at a larger valve angle (43.3°) than that of a lower valve angle (40.8°) for all values of  $Re$  due to the reduced jet impingements (Fig. 5.17). For  $\theta$  of 40.8°, as the  $Re$  varies from 2500 to 5500, the  $T_{\max}$  is reduced by 2.48 °C while  $T_{\sigma}$  is improved by 28.38%. Whereas, for  $\theta$  of 43.3°, the  $T_{\max}$  is decreased by 4.58 °C

while  $T_{\sigma}$  is enhanced by 25.76%. However, the rate of temperature decrement is observed to be lower as the  $Re$  exceeds 4750. From these results, it can be said that the sensitivity of  $T_{\max}$  and  $T_{\sigma}$  to  $Re$  reduces after a certain extent.

The  $\Delta P$  and  $T_{avg}$  across the cooling plate for different  $\theta$  and  $Re$  is shown in Table 5.4. It is evident that the  $\Delta P$  increases with the increase of  $Re$  while  $T_{avg}$  reduces. On the other hand, with the increase of  $\theta$ ,  $\Delta P$  reduces while  $T_{avg}$  increases. However, the incremental rate of  $\Delta P$  is lower with the rise of  $\theta$ . For a  $Re$  of 2500, as the  $\theta$  is increased from 40.8° to 43.3°, the  $\Delta P$  reduces by 8.21% while  $T_{avg}$  rises by 1.27%. With an enhanced  $Re$  of 5500, the  $\Delta P$  decreases by 8.35% while  $T_{avg}$  increases by 1.07%. This indicates that the effect of varying  $\theta$  on the  $\Delta P$  and  $T_{avg}$  is minimal. Hence, considering all the factors, it can be said that a smaller valve angle could be beneficial in improving the cooling plate's potential to transmit heat.

### 5.3.7 Comparison of optimized hexagonal channel design with MSTV

The performance of optimized hexagonal channel design obtained in the chapter 4 is compared with MSTV design under the same boundary conditions for varying  $Re$ . Although the flow rate is given per channel to the cold plate comprising the MSTV design in the above sections, with the goal to compare it to that of a single inlet hexagonal design, a common inlet header is utilized for the MSTV design to compare them under same flow conditions. Two parameters,  $T_{\max}$  and  $\Delta P$  are considered for comparison, and the results are shown in Table 5.5. It can be seen that the hexagonal design outperforms MSTV design

in reducing the  $T_{\max}$  with a minimal difference in  $\Delta P$ . For a  $Re$  of 2500, the hexagonal design reduces the  $T_{\max}$  by 3.7 °C compared to that of MSTV design. The same trend continues when  $Re$  increases to 5500,  $T_{\max}$  drops by 2.2 °C. From the results, it can be understood that an increase in flow rate is required for both designs to obtain a safe temperature range. Besides this, further optimization of the MSTV design is essential to achieve results similar to those of an optimized hexagonal design.

Table 5.5: Comparison of optimized hexagonal channel design with MSTV

$Re$	$T_{\max}$ (°C)		$\Delta P$ (kPa)	
	Opt. Hex.	MSTV	Opt. Hex.	MSTV
2500	51.9	55.6	4.29	4.03
3250	46.99	49.99	7.27	7.12
4000	43.79	46.4	11.03	11.14
4750	41.52	43.9	15.63	16.15
5500	39.82	42.04	20.97	22.1

## 5.4 Summary

In the present study, a novel MSTV configuration is proposed and numerically evaluated to mitigate the temperature gradient issues of conventional straight channel-based cold plates for thermal management of EVs pouch type battery module using COMSOL Multiphysics software. Different design variables are varied to analyze the cold plate's cooling efficacy. The significant findings drawn from the present study are abridged below.

- MSTV design provides effective cooling by enhancing the mini channel cold plate's heat transfer rate with flow bifurcation, self-impingement, and fluid mixing mechanisms compared to conventional straight channel design.
- At  $Re$  of 4000,  $T_{\max}$  is reduced substantially with the reverse flow in MSTV compared to that of the forward flow MSTV and straight channel design by 4.8 °C and 6.5 °C, at the cost of pressure drop.

- Increasing the channel number in the cold plate can significantly reduce the  $T_{\max}$  and  $T_{\sigma}$ . A 4-channelled reverse flow MSTV design provides a lower  $T_{\max}$  of 35.1 °C and also improves  $T_{\sigma}$  achieving 1.40 °C across the cold plate surface as  $Re$  increases from 2500 to 5500.
- For a given  $Re$ , decreasing the  $G$  value from 4.41 mm to 8.82 mm yields a higher  $T_{\max}$  and reduces the cold plate's heat transfer efficacy.
- Comparatively, a 4-channelled reverse flow MSTV cold plate with  $G$  of 8.82 mm is noticed to effectively reduce the  $T_{\max}$  by 3.2 °C and enhance  $T_{\sigma}$  by 22.17% across the cold plate surface for the variation of  $Re$  from 2500 to 5500.
- For all  $Re$ , the  $T_{\max}$  reduces with an increase of  $W_c$  and  $R$  but an inverse trend is seen with the increase of  $\theta$ . However, as the  $Re$  exceeds 3250, a minimal change in temperature reduction is observed for a  $W_c$  greater than 4.26 mm.
- For the same  $\theta$ , the change in  $T_{\max}$  and  $T_{\sigma}$  is observed to reduce at higher  $Re$ , i.e. > 4750. Moreover, for  $\theta$  of 43.3°, the  $T_{\sigma}$  is seen to be >2 °C at a lower  $Re$  of 2500. Hence, a smaller valve angle should be chosen while designing an MSTV to augment the heat transfer competency of the cooling plate.
- It can be emphasised that while selecting a  $W_c$ , the dimensions of  $R$  and  $\theta$  should be chosen synthetically, as the minimum value of  $R$  is limited for a given  $\theta$ .

A 4-channelled cold plate with reverse flow in MSTV and corresponding dimensions of  $G = 8.82$  mm,  $W_c = 3.65$  mm,  $R = 8.23$  mm and  $\theta = 40.8^\circ$  is found to be ideal in cooling the pouch batteries.

# Chapter 6

## Conclusions and Scope of Future Research

**Keywords**  
Conclusions;  
Liquid cooling;  
Future scope.  
Limitations

*This chapter highlights the conclusions based on the experimental and simulation work conducted on battery thermal management using indirect liquid cooling approach. Alongside, the scope for future work of the present dissertation is emphasized.*

### 6.1 Conclusions

The present dissertation makes contributions in two distinct domains of battery thermal management. The first step involves an in-depth evaluation of a simple mini-channelled cold plate integrated with a battery simulator to understand the efficacy of liquid cooling. Subsequently, the liquid cooling approach is enhanced particularly by modifying and optimizing the cold plate designs and regulating the temperature of the battery module within the safe operating range through simulation.

A test facility emulating heating conditions of 20Ah pouch battery using cartridge heaters and an ingeniously designed rectangular mini-channelled cold plate is developed for experimentation. Later, the study delves into the computational domain by utilizing COMSOL Multiphysics software. A three-dimensional heat transfer model is coupled with an electro-chemical thermal model to study the thermal behaviour of the pouch battery module. Followed by, designing and comparing six different channel designs with a constant volume to obtain an optimal design. Despite the conventional cold plate designs, a novel multi-stage Tesla valve is introduced to cool the pouch batteries and the corresponding thermo-hydraulic performances are explored.



The contributions of different chapters based on the objectives proposed are as follows:

### 6.1.1 Develop an experimental test facility

An experimental evaluation of liquid thermal management strategy for a 20Ah pouch-type battery module designed for an EV or HEV application is conducted. This includes a battery simulator integrated with an indigenously designed mini-channel cold plate, exploring a wide range of operating conditions such as coolant temperature, coolant flow rate and flow direction. The critical insights based on the present investigation are as follows:

- A coolant temperature range of 20 °C to 25 °C is ideal for upholding the test module within the desired range of 25 °C to 40 °C at a given coolant flow rate of 300 mL min<sup>-1</sup>.
- However, a lesser coolant flow rate of 250 mL min<sup>-1</sup> and the corresponding  $Re = 748.48$  provides trade-off between pressure drop of 2.86 kPa and heat transfer capability of 176.71 W m<sup>-2</sup> °C<sup>-1</sup>. Moreover, the capacity to reduce the maximum temperature of the module is limited with the increasing flow rate.
- Among the several flow arrangements, a parallel flow with a coolant inlet port near to the heating region is found to be the best choice with  $h_w = 185.59$  W m<sup>-2</sup> °C<sup>-1</sup> and  $\beta = 2.17$ , despite a marginal increase in temperature.

In brief, it can be stated that the temperature of the test module retained within the optimal range, justifying the utilization of a cold plate comprising rectangular mini channels to ensure better thermal management.

### 6.1.2 Comparison of different channel designs

The thermo-hydraulic performance of six different channel designs namely serpentine, U-bend, straight, pumpkin, spiral, and hexagonal, are evaluated numerically for cooling a large-capacity battery module with varying  $\dot{m}_w$  and a fixed discharge rate of 3C. The critical findings from this investigation are summarized below:

- The channel profile has a considerable impact on the hydro-thermal performance of a cold plate besides operating parameters. For a fixed flow volume, the flow-splitting channels outperform spiral channel in terms of uniformity and heat transfer performance.
- Pumpkin channel shows superior cooling performance, characterized by least pressure drop and  $j/f$  factor, among all the designs. Despite higher pressure losses, serpentine and hexagonal channel configurations achieve lower  $T_{avg}$ . Comparatively, spiral design exhibits suboptimal cooling with largest  $\Delta P$  and highest  $T_{avg}$ .
- However, all the channel designs maintained the  $T_{avg}$  within an allowable limit i.e.  $< 40$  °C under different ambient conditions for a  $T_{w,in}$  maintained at 25 °C and  $\dot{m}_w$  of 0.003 kg s<sup>-1</sup>.

### 6.1.3 Optimization through surrogate models and NSGA-II

As hexagonal channel design exhibits the best thermal performance, it is essential to optimize its design parameters and thermo-hydraulic performances. Therefore, a multi-

objective optimization technique is employed and the corresponding observations are noted.

- Despite a marginal difference in the  $R^2$  value compared to RSM in case of  $h_w$ , the Kriging model exhibits consistent performance for most of the scenarios.
- On applying SHAP technique to the Kriging model, the variables regulating the change in  $R^2$  for  $T_{\max}$  are found to be  $\dot{m}_w$  and  $T_{w,in}$ . Similarly, in the case of  $\Delta P$  and  $h_w$ , the  $\dot{m}_w$  and  $W_c$  are the major influential variables.
- Following optimization, the Pareto solutions reflected a compromise improvement in  $T_{\max}$  (31.75 °C to 38 °C), pressure drop (224.4 Pa to 649.9 Pa) and  $h_w$  (493.35 W m<sup>-2</sup> C<sup>-1</sup> to 703.40 W m<sup>-2</sup> C<sup>-1</sup>).
- The validation of three best solutions obtained by K-means clustering algorithm attests to the Kriging model's accuracy, with a maximum relative error below 10%.

### 6.1.4 Introducing a novel channel design

Here, a novel MSTV configuration is introduced and numerically assessed to alleviate the temperature gradient issues of a traditional straight channel design-based cold plates for cooling of pouch batteries utilizing COMSOL Multiphysics software. The key findings from the investigation are summarized as follows:

- At  $Re$  of 4000,  $T_{\max}$  is reduced substantially with the reverse flow in MSTV compared to that of the forward flow MSTV and conventional straight channel design by 4.8 °C and 6.5 °C, at the cost of pressure drop.

- A 4-channelled reverse flow MSTV cold plate with  $G$  of 8.82 mm is noticed to effectively reduce the  $T_{\max}$  by 3.2 °C and enhance  $T_{\sigma}$  by 22.17% across the cold plate surface for the variation of  $Re$  from 2500 to 5500 due to the presence of flow bifurcation, self-impingement, and fluid mixing mechanisms.
- For a given  $Re$ , the  $\Delta P$  reduces linearly with an increase in  $W_c$ , with a minimal decrement rate with varying  $R$  and  $\theta$ . Whereas, temperature reduction is seen to be maximum with increased  $W_c$  and  $R$ , but an inverse trend with  $\theta$ . However, as the  $Re$  exceeds 3250, only a small change in temperature reduction is seen with a  $W_c > 4.26$  mm.
- It can be emphasised that while selecting a  $W_c$ , the dimensions of  $R$  and  $\theta$  should be chosen synthetically, as the minimum value of  $R$  is limited for a given  $\theta$ .

The proposed MSTV design with the reverse flow can effectively reduce the maximum temperature and maintain homogeneity for a battery discharge rate of 2C.

The final outcome of this thesis is summarized as liquid cooling with innovative hexagonal or MSTV based cold plates can effectively retain the Li-ion battery module temperature of an EV within the range of 25 °C to 40 °C for diverse operating conditions. Although the present work is limited to pouch-type batteries, in practical applications, the above-obtained insights can help design a cold plate for BTMS as different battery types, chemistry, or capacities could be employed in an EV.

## 6.2 Scope of Future Work

The dissertation offers insightful information on the BTMS using an indirect liquid cooling approach. Yet, certain aspects could not be considered in the present dissertation. However,

the outcomes of the research conducted open up a new direction in further enhancing the battery module cooling, some of which are stated below:

- Fabrication of cold plate, real-time experiments with a  $\text{LiFePO}_4$  pouch battery module and simulation results validation can all be done using the identified optimal channel designs-serpentine, hexagonal and pumpkin-as a basis.
- The experiments can be further extended to different battery chemistries and large battery packs based on the size and rating used in an EV under real-time Indian driving profiles, ensuring the robustness of cold plate.
- The ability of proposed multi-stage Tesla valve and its practical implementation in BTMS can be further expanded by fine-tuning its design and operational parameters using appropriate surrogate models and metaheuristic algorithms. Further, its performance can be validated with real-time experiments using an actual battery module.
- The present work considers aluminium as the material for cold plate. By integrating advanced materials in the fabrication of cold plate, the cooling efficiency and thermal conductivity can be further enhanced.

## REFERENCES

---

---

- Alfaryjat, A. A., Mohammed, H. A., Adam, N. M., Ariffin, M. K. A. and Najafabadi, M. I. (2014), Influence of geometrical parameters of hexagonal, circular, and rhombus microchannel heat sinks on the thermohydraulic characteristics, *International Communications in Heat and Mass Transfer*, Vol. 52, pp. 121–131.
- An, Z., Shah, K., Jia, L. and Ma, Y. (2019), A parametric study for optimization of minichannel based battery thermal management system, *Applied Thermal Engineering*, Vol. 154, No. February, pp. 593–601.
- Bahiraee, F., Fartaj, A. and Nazri, G. A. (2017), Electrochemical-thermal Modeling to Evaluate Active Thermal Management of a Lithium-ion Battery Module, *Electrochimica Acta*, Vol. 254, pp. 59–71.
- Bahiraee, F., Ghalkhani, M., Fartaj, A. and Nazri, G. A. (2017), A pseudo 3D electrochemical-thermal modeling and analysis of a lithium-ion battery for electric vehicle thermal management applications, *Applied Thermal Engineering*, Vol. 125, pp. 904–918.
- Bandhauer, T. M., Garimella, S. and Fuller, T. F. (2011), A critical review of thermal issues in lithium-ion batteries, *Journal of the Electrochemical Society*, Vol. 158, No. 3, .
- Bardell, R. L. and Microsciences, M. (2017), The Diode Mechanism of Tesla-Type No-Moving-Parts Valves The Diode Mechanism of Tesla-Type No-Moving-Parts Valves University of Washington Program Authorized to Offer Degree : Mechanical Engineering, No. October, .
- Berdichevsky, G., Everett, T., Kohn, S., Park, M., Lyons, D., Alto, P., Mendez, N. J. and View, M. (2009), Battery Pack Thermal Management System (US20090023056A1), , Vol. 1, No. 19, .
- Bernardi, D., Pawlikowski, E. and Newman, J. (1985), A General Energy Balance for Battery Systems\_Bernardi D, Powlikowski E and Newman, *Journal of the electrochemical society*, Vol. 132, No. 1, pp. 5–12.
- Blank, J. and Deb, K. (2020), Pymoo: Multi-Objective Optimization in Python, *IEEE Access*, Vol. 8, pp. 89497–89509.
- Chang, G., Cui, X., Li, Y. and Ji, Y. (2020), Effects of reciprocating liquid flow battery thermal management system on thermal characteristics and uniformity of large lithium-ion battery pack, *International Journal of Energy Research*No. March, pp. 1–13.
- Chen, K., Song, M., Wei, W. and Wang, S. (2019), International Journal of Heat and Mass Transfer Design of the structure of battery pack in parallel air-cooled battery thermal management system for cooling efficiency improvement, *International Journal of Heat and Mass Transfer*, Vol. 132, pp. 309–321.
- Chen, Y., Chen, K., Dong, Y. and Wu, X. (2022), Bidirectional symmetrical parallel mini-channel cold plate for energy efficient cooling of large battery packs, *Energy*, Vol. 242, .
- Chiew, J., Chin, C. S., Toh, W. D., Gao, Z., Jia, J. and Zhang, C. Z. (2019), A pseudo three-dimensional electrochemical-thermal model of a cylindrical LiFePO<sub>4</sub>/graphite battery, *Applied Thermal Engineering*,

- Vol. 147, No. August 2018, pp. 450–463.
- Cho, H. M., Choi, W. S., Go, J. Y., Bae, S. E. and Shin, H. C. (2012), A study on time-dependent low temperature power performance of a lithium-ion battery, *Journal of Power Sources*, Vol. 198, pp. 273–280.
- Cuma, M. U. and Koroglu, T. (2015), A comprehensive review on estimation strategies used in hybrid and battery electric vehicles, *Renewable and Sustainable Energy Reviews*, Vol. 42, pp. 517–531.
- Deb, K., Pratap, A., Agarwal, S. and Meyarivan, T. (2002), A fast and elitist multiobjective genetic algorithm: NSGA-II, *IEEE Transactions on Evolutionary Computation*, Vol. 6, No. 2, pp. 182–197.
- Deng, T., Ran, Y., Yin, Y., Chen, X. and Liu, P. (2019), Multi-objective optimization design of double-layered reverting cooling plate for lithium-ion batteries, *International Journal of Heat and Mass Transfer*, Vol. 143, pp. 118580.
- Deng, T., Ran, Y., Yin, Y. and Liu, P. (2020), Multi-objective optimization design of thermal management system for lithium-ion battery pack based on Non-dominated Sorting Genetic Algorithm II, *Applied Thermal Engineering*, Vol. 164, No. 66, pp. 114394.
- Deng, T., Ran, Y., Zhang, G., Chen, X. and Tong, Y. (2019), Design optimization of bifurcating mini-channels cooling plate for rectangular Li-ion battery, *International Journal of Heat and Mass Transfer*, Vol. 139, pp. 963–973.
- Deng, T., Ran, Y., Zhang, G. and Yin, Y. (2019), Novel leaf-like channels for cooling rectangular lithium ion batteries, *Applied Thermal Engineering*, Vol. 150, No. 66, pp. 1186–1196.
- Deng, T., Zhang, G. and Ran, Y. (2018), Study on thermal management of rectangular Li-ion battery with serpentine-channel cold plate, *International Journal of Heat and Mass Transfer*, Vol. 125, pp. 143–152.
- Deng, Y., Feng, C., Jiaqiang, E., Zhu, H. and Chen, J. (2018), Effects of different coolants and cooling strategies on the cooling performance of the power lithium ion battery system: A review, *Energy*, Vol. 142, No. April, pp. 10–29.
- Dong, F., Cheng, Z., Song, D. and Ni, J. (2021), Investigation and optimization on cooling performance of serial-parallel mini-channel structure for liquid-cooled soft pack batteries, *Numerical Heat Transfer; Part A: Applications*, Vol. 80, No. 7, pp. 368–387.
- Fan, L., Khodadadi, J. M. and Pesaran, A. A. (2013), A parametric study on thermal management of an air-cooled lithium-ion battery module for plug-in hybrid electric vehicles, *Journal of Power Sources*, Vol. 238, pp. 301–312.
- Fan, Y., Wang, Z. and Fu, T. (2021), Multi-objective optimization design of lithium-ion battery liquid cooling plate with double-layered dendritic channels, *Applied Thermal Engineering*, Vol. 199, No. May, pp. 117541.
- Fathabadi, H. (2014), A novel design including cooling media for Lithium-ion batteries pack used in hybrid and electric vehicles, *Journal of Power Sources*, Vol. 245, pp. 495–500.
- Feng, X., Lu, L., Ouyang, M., Li, J. and He, X. (2016), A 3D thermal runaway propagation model for a large format lithium ion battery module, *Energy*, Vol. 115, pp. 194–208.
- Feng, X., Ouyang, M., Liu, X., Lu, L., Xia, Y. and He, X. (2018), Thermal runaway mechanism of lithium ion battery for electric vehicles: A review, *Energy Storage Materials*, Vol. 10, pp. 246–267.

- Gamboa, A. R., Morris, C. J. and Forster, F. K. (2005), Improvements in fixed-valve micropump performance through shape optimization of valves, *Journal of Fluids Engineering, Transactions of the ASME*, Vol. 127, No. 2, pp. 339–346.
- George Em Karniadakis, Ioannis G. Kevrekidis, Lu Lu, Paris Perdikaris, S. W. and L. Y. (2021), Physics-informed machine learning, *Nature Reviews Physics*, Vol. 3, pp. 442–440.
- Gou, J. and Liu, W. (2019), Feasibility study on a novel 3D vapor chamber used for Li-ion battery thermal management system of electric vehicle, *Applied Thermal Engineering*, Vol. 152, No. February, pp. 362–369.
- Gu, H. (1983), Mathematical Analysis of a Zn / NiOOH Cell, *Journal of The Electrochemical Society*, Vol. 130, No. 7, pp. 1459–1464.
- Al Hallaj, S., Prakash, J. and Selman, J. R. (2000), Characterization of commercial Li-ion batteries using electrochemical–calorimetric measurements, *Journal of Power Sources*, Vol. 87, No. 1, pp. 186–194.
- Huang, Y., Mei, P., Lu, Y., Huang, R., Yu, X., Chen, Z. and Roskilly, A. P. (2019), A novel approach for Lithium-ion battery thermal management with streamline shape mini channel cooling plates, *Applied Thermal Engineering*, Vol. 157, No. November 2018, pp. 113623.
- Huo, Y., Rao, Z., Liu, X. and Zhao, J. (2015), Investigation of power battery thermal management by using mini-channel cold plate, *Energy Conversion and Management*, Vol. 89, pp. 387–395.
- Jarrett, A. and Kim, I. Y. (2011), Design optimization of electric vehicle battery cooling plates for thermal performance, *Journal of Power Sources*, Vol. 196, No. 23, pp. 10359–10368.
- Jiang, G., Zhuang, L., Hu, Q., Liu, Z. and Huang, J. (2020), An investigation of heat transfer and capacity fade in a prismatic Li-ion battery based on an electrochemical-thermal coupling model, *Applied Thermal Engineering*, Vol. 171, No. September 2019, .
- Jiang, P., Fan, M., Si, G. and Ren, Z. (2001), Thermal  $\pm$  hydraulic performance of small scale micro-channel and porous-media heat-exchangers, , Vol. 44, .
- Jiaqiang, E., Han, D., Qiu, A., Zhu, H., Deng, Y., Chen, Jingwei, Zhao, X., Zuo, W., Wang, H., Chen, Jianmei and Peng, Q. (2018), Orthogonal experimental design of liquid-cooling structure on the cooling effect of a liquid-cooled battery thermal management system, *Applied Thermal Engineering*, Vol. 132, pp. 508–520.
- Jiaqiang, E., Xu, S., Deng, Y., Zhu, H., Zuo, W., Wang, H., Chen, J., Peng, Q. and Zhang, Z. (2018), Investigation on thermal performance and pressure loss of the fluid cold-plate used in thermal management system of the battery pack, *Applied Thermal Engineering*, Vol. 145, No. July, pp. 552–568.
- Jin, L. W., Lee, P. S., Kong, X. X., Fan, Y. and Chou, S. K. (2014), Ultra-thin minichannel LCP for EV battery thermal management, *Applied Energy*, Vol. 113, pp. 1786–1794.
- Jin, R., Chen, W. and Sudjianto, A. (2018), Detc2003 / D Ac -48 760 an Efficient Algorithm for Constructing Optimal, pp. 1–10.
- Jin, Z. jiang, Gao, Z. xin, Chen, M. rui and Qian, J. yuan (2018), Parametric study on Tesla valve with reverse flow for hydrogen decompression, *International Journal of Hydrogen Energy*, Vol. 43, No. 18, pp. 8888–8896.
- Jung, J. Y. and Kwak, H. Y. (2008), Fluid flow and heat transfer in microchannels with rectangular cross



- section, *Heat and Mass Transfer/Waerme- und Stoffuebertragung*, Vol. 44, No. 9, pp. 1041–1049.
- Karagiorgi, G., Kasieczka, G., Kravitz, S., Nachman, B. and Shih, D. (2022), Machine learning in the search for new fundamental physics, *Nature Reviews Physics*, Vol. 4, No. 6, pp. 399–412.
- Keyser, M., Pesaran, A., Li, Q., Santhanagopalan, S., Smith, K., Wood, E., Ahmed, S., Bloom, I., Dufek, E., Shirk, M., Meintz, A., Kreuzer, C., Michelbacher, C., Burnham, A., Stephens, T., Francfort, J., Carlson, B., Zhang, J., Vijayagopal, R., Hardy, K., Dias, F., Mohanpurkar, M., Scofield, D., Jansen, A. N., Tanim, T. and Markel, A. (2017), Enabling fast charging – Battery thermal considerations, *Journal of Power Sources*, Vol. 367, pp. 228–236.
- Kim, J., Oh, J. and Lee, H. (2019), Review on battery thermal management system for electric vehicles, *Applied Thermal Engineering*, Vol. 149, No. November 2018, pp. 192–212.
- Kim, U. S., Shin, C. B. and Kim, C. S. (2008), Effect of electrode configuration on the thermal behavior of a lithium-polymer battery, *Journal of Power Sources*, Vol. 180, No. 2, pp. 909–916.
- Lai, Y., Du, S., Ai, Liang, Ai, Lihua, Cheng, Y., Tang, Y. and Jia, M. (2015a), Insight into heat generation of lithium ion batteries based on the electrochemical-thermal model at high discharge rates, *International Journal of Hydrogen Energy*, Vol. 40, No. 38, pp. 13039–13049.
- Lai, Y., Du, S., Ai, Liang, Ai, Lihua, Cheng, Y., Tang, Y. and Jia, M. (2015b), Insight into heat generation of lithium ion batteries based on the electrochemical-thermal model at high discharge rates, *International Journal of Hydrogen Energy*, Vol. 40, No. 38, pp. 13039–13049.
- Li, K., Wang, H., Xu, C., Wu, W., Zhang, W., Hou, J., Rui, X., Chen, Y., Fan, L., Feng, X. and Ouyang, M. (2022), Multi-objective optimization of side plates in a large format battery module to mitigate thermal runaway propagation, *International Journal of Heat and Mass Transfer*, Vol. 186, pp. 122395.
- Li, W., Garg, A., Xiao, M. and Gao, L. (2021), Optimization for liquid cooling cylindrical battery thermal management system based on gaussian process model, *Journal of Thermal Science and Engineering Applications*, Vol. 13, No. 2, .
- Li, W. Q., Qu, Z. G., He, Y. L. and Tao, Y. B. (2014), Experimental study of a passive thermal management system for high-powered lithium ion batteries using porous metal foam saturated with phase change materials, *Journal of Power Sources*, Vol. 255, pp. 9–15.
- Li, Y., Zhou, Z. and Wu, W. T. (2019), Three-dimensional thermal modeling of Li-ion battery cell and 50 V Li-ion battery pack cooled by mini-channel cold plate, *Applied Thermal Engineering*, Vol. 147, No. July 2018, pp. 829–840.
- Lin, X., Perez, H. E., Mohan, S., Siegel, J. B., Stefanopoulou, A. G., Ding, Y. and Castanier, M. P. (2014), A lumped-parameter electro-thermal model for cylindrical batteries, *Journal of Power Sources*, Vol. 257, pp. 12–20.
- Liu, H. ling, Shi, H. bo, Shen, H. and Xie, G. (2019), The performance management of a Li-ion battery by using tree-like mini-channel heat sinks: Experimental and numerical optimization, *Energy*, Vol. 189, pp. 116150.
- Liu, Y. and Zhang, J. (2019), Design a J-type air-based battery thermal management system through

- surrogate-based optimization, *Applied Energy*, Vol. 252, No. March, pp. 113426.
- Lu, M., Zhang, X., Ji, J., Xu, X. and Zhang, Y. (2020), Research progress on power battery cooling technology for electric vehicles, *Journal of Energy Storage*, Vol. 27, No. December 2019, pp. 101155.
- Lundberg, S. M. and Lee, S. I. (2017), A unified approach to interpreting model predictions, *Advances in Neural Information Processing Systems*, Vol. 2017-Decem, No. Section 2, pp. 4766–4775.
- Lyu, Y., Siddique, A. R. M., Majid, S. H., Biglarbegian, M., Gadsden, S. A. and Mahmud, S. (2019), Electric vehicle battery thermal management system with thermoelectric cooling, *Energy Reports*, Vol. 5, pp. 822–827.
- Ma, S., Jiang, M., Tao, P., Song, C., Wu, J., Wang, J., Deng, T. and Shang, W. (2018), Temperature effect and thermal impact in lithium-ion batteries: A review, *Progress in Natural Science: Materials International*, Vol. 28, No. 6, pp. 653–666.
- Mevawalla, A., Shabeer, Y., Tran, M. K., Panchal, S., Fowler, M. and Fraser, R. (2022), Measurable Parameters, pp. 1–34.
- Mishra, P. and Gupta, S. N. (1979), Momentum Transfer in Curved Pipes. 1. Newtonian Fluids, *Industrial and Engineering Chemistry Process Design and Development*, Vol. 18, No. 1, pp. 130–137.
- Mistry, A. N., Palle, H. R. and Mukherjee, P. P. (2019), In operando thermal signature probe for lithium-ion batteries, *Applied Physics Letters*, Vol. 114, No. 2, .
- Moffat, R. J. (1988), Describing the uncertainties in experimental results, *Experimental Thermal and Fluid Science*, Vol. Vol. 1, pp. 3–17.
- Monika, K., Chakraborty, C., Roy, S., Dinda, S., Singh, S. A. and Datta, S. P. (2021), Parametric investigation to optimize the thermal management of pouch type lithium-ion batteries with mini-channel cold plates, *International Journal of Heat and Mass Transfer*, Vol. 164, pp. 120568.
- Myers, R. H., Montgomery, D. C., Vining, G. G., Connie, M., Kowalski, S. M., Myers, R. H., Montgomery, D. C., Vining, G. G., Connie, M., Myers, R. H., Vining, G. G. and Kowalski, S. M. (2018), Response Surface Methodology : A Retrospective and Literature Survey Response Surface Methodology : A Retrospective and Literature Survey, , Vol. 4065, .
- Naqiuddin, N. H., Saw, L. H., Yew, M. C., Yusof, F., Ng, T. C. and Yew, M. K. (2018), Overview of micro-channel design for high heat flux application, *Renewable and Sustainable Energy Reviews*, Vol. 82, No. February 2017, pp. 901–914.
- Newman and Tiedemann (1993), Potential and Current Distribution in Electrochemical Cells Interpretation of the Half-Cell Voltage Measurements as a Function of Reference-Electrode Location, *J Electrochem Soc*, Vol. 140, No. 7, pp. 9.
- Om, N. I., Zulkifli, R. and Gunnasegaran, P. (2018), Influence of the oblique fin arrangement on the fluid flow and thermal performance of liquid cold plate, *Case Studies in Thermal Engineering*, Vol. 12, No. June, pp. 717–727.
- Panchal, S., Dincer, I., Agelin-Chaab, M., Fraser, R. and Fowler, M. (2017), Transient electrochemical heat transfer modeling and experimental validation of a large sized LiFePO<sub>4</sub>/graphite battery, *International*

- Journal of Heat and Mass Transfer, Vol. 109, pp. 1239–1251.
- Panchal, S., Khasow, R., Dincer, I., Agelin-Chaab, M., Fraser, R. and Fowler, M. (2017), Numerical modeling and experimental investigation of a prismatic battery subjected to water cooling, *Numerical Heat Transfer; Part A: Applications*, Vol. 71, No. 6, pp. 626–637.
- Panchal, S., Khasow, R., Dincer, I., Agelin-Chaab, M., Fraser, R. and Fowler, M. (2017), Thermal design and simulation of mini-channel cold plate for water cooled large sized prismatic lithium-ion battery, *Applied Thermal Engineering*, Vol. 122, pp. 80–90.
- Patil, M. S., Seo, J. H., Panchal, S., Jee, S. W. and Lee, M. Y. (2020), Investigation on thermal performance of water-cooled Li-ion pouch cell and pack at high discharge rate with U-turn type microchannel cold plate, *International Journal of Heat and Mass Transfer*, Vol. 155, pp. 119728.
- Porwal, P. R., Thompson, S. M., Walters, D. K. and Jamal, T. (2018), Heat transfer and fluid flow characteristics in multistaged Tesla valves, *Numerical Heat Transfer; Part A: Applications*, Vol. 73, No. 6, pp. 347–365.
- Qian, J. yuan, Chen, M. rui, Liu, X. ling and Jin, Z. jiang (2019), A numerical investigation of the flow of nanofluids through a micro Tesla valve, *Journal of Zhejiang University: Science A*, Vol. 20, No. 1, pp. 50–60.
- Qian, J. yuan, Wu, J. yi, Gao, Z. xin, Wu, A. and Jin, Z. jiang (2019), Hydrogen decompression analysis by multi-stage Tesla valves for hydrogen fuel cell, *International Journal of Hydrogen Energy*, Vol. 44, No. 26, pp. 13666–13674.
- Qian, Z., Li, Y. and Rao, Z. (2016), Thermal performance of lithium-ion battery thermal management system by using mini-channel cooling, *Energy Conversion and Management*, Vol. 126, pp. 622–631.
- Qu, J., Ke, Z., Zuo, A. and Rao, Z. (2019), Experimental investigation on thermal performance of phase change material coupled with three-dimensional oscillating heat pipe (PCM/3D-OHP) for thermal management application, *International Journal of Heat and Mass Transfer*, Vol. 129, pp. 773–782.
- Qu, Z. G., Li, W. Q. and Tao, W. Q. (2014), Numerical model of the passive thermal management system for high-power lithium ion battery by using porous metal foam saturated with phase change material, *International Journal of Hydrogen Energy*, Vol. 39, No. 8, pp. 3904–3913.
- Rao, Z., Huo, Y. and Liu, X. (2014), Experimental study of an OHP-cooled thermal management system for electric vehicle power battery, *Experimental Thermal and Fluid Science*, Vol. 57, pp. 20–26.
- Rao, Z., Qian, Z., Kuang, Y. and Li, Y. (2017), Thermal performance of liquid cooling based thermal management system for cylindrical lithium-ion battery module with variable contact surface, *Applied Thermal Engineering*, Vol. 123, pp. 1514–1522.
- Rao, Z. and Xuan Zhang (2019), Investigation on thermal management performance of wedge - shaped microchannels for rectangular Li-ion batteries, *international journal of energy research* No. February, pp. 3876–3890.
- Rhodes, M. J. and Thompson, S. M. (2020), Experimental investigation of a flat-plate oscillating heat pipe with groove-enhanced minichannels, *Journal of Thermal Science and Engineering Applications*, Vol. 12, No.

6, pp. 1–13.

Ruan, H., Sun, B., Jiang, J., Zhang, W., He, X., Su, X., Bian, J. and Gao, W. (2021), A modified-electrochemical impedance spectroscopy-based multi-time-scale fractional-order model for lithium-ion batteries, *Electrochimica Acta*, Vol. 394, pp. 139066.

Saw, L. H., Poon, H. M., Thiam, H. S., Cai, Z., Chong, W. T., Pambudi, N. A. and King, Y. J. (2018), Novel thermal management system using mist cooling for lithium-ion battery packs, *Applied Energy*, Vol. 223, No. April, pp. 146–158.

Seaman, A., Dao, T. S. and McPhee, J. (2014), A survey of mathematics-based equivalent-circuit and electrochemical battery models for hybrid and electric vehicle simulation, *Journal of Power Sources*, Vol. 256, pp. 410–423.

Seshadri, A. (2017), 19th International Conference on Human-Computer Interaction, HCI International 2017, Lecture Notes in Computer Science (including subseries Lecture Notes in Artificial Intelligence and Lecture Notes in Bioinformatics), Vol. 10271 LNCS, pp. 1–729.

Sheng, L., Su, L., Zhang, H., Li, K., Fang, Yidong, Ye, W. and Fang, Yu (2019), Numerical investigation on a lithium ion battery thermal management utilizing a serpentine-channel liquid cooling plate exchanger, *International Journal of Heat and Mass Transfer*, Vol. 141, pp. 658–668.

Siruvuri, S. D. V. S. S. V. and Budarapu, P. R. (2020), Studies on thermal management of Lithium-ion battery pack using water as the cooling fluid, *Journal of Energy Storage*, Vol. 29, No. March, pp. 101377.

Smith, J., Singh, R., Hinterberger, M. and Mochizuki, M. (2018), Battery thermal management system for electric vehicle using heat pipes, *International Journal of Thermal Sciences*, Vol. 134, No. June 2017, pp. 517–529.

Søndergaard, J. (2002), Dace – a matlab kriging toolbox,.

Suman, S., Goel, A. and Kushwah, Y. S. (2021), Design Optimization of Battery Thermal Management System for Electric Vehicles, *SAE Technical Papers*, Vol. 196, No. 2021, .

Suresh Patil, M., Seo, J. H. and Lee, M. Y. (2021), A novel dielectric fluid immersion cooling technology for Li-ion battery thermal management, *Energy Conversion and Management*, Vol. 229, No. December 2020, pp. 113715.

Tang, X., Guo, Q., Li, M., Wei, C., Pan, Z. and Wang, Y. (2021), Performance analysis on liquid-cooled battery thermal management for electric vehicles based on machine learning, *Journal of Power Sources*, Vol. 494, No. September 2020, .

Taylor, P. (2013), Experimental Heat Transfer : A Journal of , Thermal Energy Transport , Storage , and Conversion HYDRODYNAMIC Generation AND HEAT TRANSFER STUDY OF DISPERSED FLUIDS WITH SUBMICRON METALLIC OXIDE, *Thermal Energy* No. January 2013, pp. 37–41.

Thompson, S. M., Jamal, T., Paudel, B. J. and Walters, D. K. (2013), Transitional and turbulent flow modeling in a tesla valve, *ASME International Mechanical Engineering Congress and Exposition, Proceedings (IMECE)*, Vol. 7 B, No. November, .

Thompson, S. M., Paudel, B. J., Jamal, T. and D. K. Walters (2015), Numerical Investigation of Multistaged

- Tesla Valves, *Journal of Fluids Engineering*, Vol. 136, No. August 2014, pp. 113–124.
- Tong, W., Somasundaram, K., Birgersson, E., Mujumdar, A. S. and Yap, C. (2015), Numerical investigation of water cooling for a lithium-ion bipolar battery pack, *International Journal of Thermal Sciences*, Vol. 94, pp. 259–269.
- Tong, W., Somasundaram, K., Birgersson, E., Mujumdar, A. S. and Yap, C. (2016), Thermo-electrochemical model for forced convection air cooling of a lithium-ion battery module, *Applied Thermal Engineering*, Vol. 99, pp. 672–682.
- Vertiz, G., Oyarbide, M., Macicior, H., Miguel, O., Cantero, I., Fernandez De Arroiabe, P. and Ulacia, I. (2014), Thermal characterization of large size lithium-ion pouch cell based on 1d electro-thermal model, *Journal of Power Sources*, Vol. 272, pp. 476–484.
- De Vita, A., Maheshwari, A., Destro, M., Santarelli, M. and Carello, M. (2017), Transient thermal analysis of a lithium-ion battery pack comparing different cooling solutions for automotive applications, *Applied Energy*, Vol. 206, No. August, pp. 101–112.
- Wahidi, T., Chandavar, R. A. and Yadav, A. K. (2020), Stability enhancement of supercritical CO<sub>2</sub> based natural circulation loop using a modified Tesla valve, *Journal of Supercritical Fluids*, Vol. 166, pp. 105020.
- Wang, N., Li, C., Li, W., Chen, X., Li, Y. and Qi, D. (2021), Heat dissipation optimization for a serpentine liquid cooling battery thermal management system: An application of surrogate assisted approach, *Journal of Energy Storage*, Vol. 40, No. April, .
- Wu, Weixiong, Wang, S., Wu, Wei, Chen, K., Hong, S. and Lai, Y. (2019), A critical review of battery thermal performance and liquid based battery thermal management, *Energy Conversion and Management*, Vol. 182, No. September 2018, pp. 262–281.
- Wu, X. Y., Zhang, H. Y., Zhu, Z. H. and Song, L. M. (2020), Numerical Investigation of a Liquid Cooled Battery Module With Collaborative Heat Dissipation in Both Axial and Radial Directions, *Kung Cheng Je Wu Li Hsueh Pao/Journal of Engineering Thermophysics*, Vol. 41, No. 7, pp. 1784–1791.
- Xie, Y., Li, W., Hu, X., Tran, M. K., Panchal, S., Fowler, M. and Liu, K. (2022), Co-estimation of SOC and three-dimensional SOT for lithium-ion batteries based on distributed spatial-temporal online correction, *IEEE Transactions on Industrial Electronics*, Vol. 70, No. 6, pp. 5937–5948.
- Xu, H., Zhang, X., Xiang, G. and Li, H. (2021), Optimization of liquid cooling and heat dissipation system of lithium-ion battery packs of automobile, *Case Studies in Thermal Engineering*, Vol. 26, No. April, .
- Xu, X., Li, W., Xu, B. and Qin, J. (2019), Numerical study on a water cooling system for prismatic LiFePO<sub>4</sub> batteries at abused operating conditions, *Applied Energy*, Vol. 250, No. January, pp. 404–412.
- Xun, J., Liu, R. and Jiao, K. (2013), Numerical and analytical modeling of lithium ion battery thermal behaviors with different cooling designs, *Journal of Power Sources*, Vol. 233, pp. 47–61.
- Yalçın, S., Panchal, S. and Herdem, M. S. (2022), A CNN-ABC model for estimation and optimization of heat generation rate and voltage distributions of lithium-ion batteries for electric vehicles, *International Journal of Heat and Mass Transfer*, Vol. 199, .
- Yang, L. and Shami, A. (2020), Neurocomputing On hyperparameter optimization of machine learning

algorithms : Theory and practice, Neurocomputing, Vol. 415, pp. 295–316.

Yang, W. H., Zhang, J. Z. and Cheng, H. E. (2005), The study of flow characteristics of curved microchannel, Applied Thermal Engineering, Vol. 25, No. 13, pp. 1894–1907.

Yang, X., Wei, L., Cao, F., Zhang, L., Lu, Z., Meng, X. and Jin, L. (2019), A parametric study of laminar convective heat transfer in fractal minichannels with hexagonal fins, International Journal of Energy Research, Vol. 2018, No. May, pp. 1–17.

Zhang, J., Jin, R., Yang, Y. and Hauptmann, A. G. (2003), Modified Logistic Regression : An Approximation to SVM and Its Applications in Large-Scale Text Categorization, No. 1999, .

Zubi, G., Dufo-López, R., Carvalho, M. and Pasaoglu, G. (2018), The lithium-ion battery: State of the art and future perspectives, Renewable and Sustainable Energy Reviews, Vol. 89, No. October 2017, pp. 292–308.

## APPENDIX A

Simulation results of the objective functions for the dataset generated using ESE-LHS method in section 4.4.3.

<i>S. No</i>	<i>L</i> (mm)	<i>W<sub>c</sub></i> (mm)	<i>θ</i> (°)	<i>m<sub>w</sub></i> (kg s <sup>-1</sup> )	<i>T<sub>w,in</sub></i> (°C)	<i>T<sub>max</sub></i> (°C)	<i>ΔP</i> (Pa)	<i>h<sub>w</sub></i> (W m <sup>-2</sup> °C <sup>-1</sup> )
1	18.755	4.683	97.706	0.001	30.301	42.037	100.100	328.087
2	17.454	3.937	86.849	0.003	31.489	38.234	555.100	697.430
3	18.079	3.137	64.434	0.002	30.714	39.091	393.900	571.719
4	18.439	3.363	73.315	0.004	31.674	37.667	1020.000	725.397
5	18.667	3.619	95.280	0.004	27.065	33.283	975.300	847.891
6	16.336	4.430	117.176	0.001	31.097	42.519	122.380	277.276
7	16.642	3.424	114.586	0.001	25.316	39.006	179.750	386.105
8	17.485	3.056	81.889	0.003	34.673	41.199	799.900	632.757
9	17.739	4.427	76.246	0.004	32.234	38.156	666.400	482.141
10	17.815	4.853	77.724	0.003	31.291	38.044	374.800	586.332
11	16.997	3.487	72.788	0.003	32.554	39.284	626.800	715.378
12	15.070	3.216	108.400	0.003	27.197	34.199	962.900	547.559
13	17.308	3.283	65.215	0.005	28.081	33.862	1468.200	766.990
14	16.602	3.983	67.059	0.001	34.171	44.443	105.720	274.754
15	16.738	3.384	119.089	0.003	33.776	40.270	924.600	716.810
16	17.911	4.322	79.800	0.004	27.538	33.735	700.800	578.964
17	17.521	4.154	96.219	0.002	30.422	38.782	290.500	390.073
18	17.718	3.537	78.231	0.005	25.013	30.891	1359.300	772.627
19	15.613	4.492	113.340	0.004	31.556	37.390	898.300	658.561
20	15.699	4.934	80.538	0.003	30.254	37.171	372.200	633.043
21	18.779	3.646	70.652	0.003	32.165	38.912	577.500	558.943
22	16.470	3.760	71.881	0.003	31.800	38.600	554.800	633.694
23	18.000	4.602	93.538	0.003	27.290	34.345	442.900	493.045
24	17.361	3.734	84.949	0.003	26.188	33.422	586.900	613.781
25	18.476	4.027	92.403	0.002	27.126	35.951	300.000	470.540
26	17.859	4.646	89.972	0.005	29.249	34.778	937.600	708.156
27	18.531	3.865	81.568	0.004	30.809	36.754	829.900	799.613
28	18.585	4.994	88.208	0.003	33.020	39.608	378.800	708.235
29	15.137	3.704	101.246	0.003	30.006	36.790	742.800	482.846
30	18.250	4.461	78.394	0.002	30.173	38.566	242.700	372.507
31	16.062	3.240	119.732	0.002	29.692	38.087	530.900	495.901
32	17.825	4.624	103.914	0.002	28.910	37.466	256.900	450.215
33	15.455	4.832	118.658	0.003	32.507	39.104	507.000	458.106
34	18.338	4.749	75.351	0.002	33.089	41.050	217.200	313.813
35	18.127	3.360	64.607	0.001	27.351	40.298	132.140	389.846
36	18.175	4.400	107.831	0.005	33.165	38.441	1064.600	584.765
37	16.824	4.865	78.726	0.002	32.870	40.897	213.400	388.001
38	18.347	4.796	103.637	0.004	28.034	34.120	655.600	612.697
39	15.406	4.591	113.420	0.002	32.688	40.637	295.100	273.690
40	18.042	3.464	100.627	0.002	28.816	37.415	381.300	445.101
41	17.116	4.870	82.571	0.004	28.435	34.543	596.700	624.148
42	18.972	3.021	79.216	0.002	27.735	36.513	429.400	452.071
43	15.260	3.585	105.639	0.005	32.788	38.039	1872.000	755.317
44	17.054	3.072	60.793	0.004	33.670	39.594	1132.200	824.177

45	16.558	3.069	111.789	0.005	28.549	34.054	2519.000	633.733
46	18.480	3.292	101.704	0.003	33.727	40.282	756.200	786.759
47	18.632	4.256	97.332	0.004	25.637	31.905	761.400	737.408
48	15.715	4.735	65.576	0.003	28.467	35.581	378.800	504.976
49	16.153	4.803	80.347	0.002	27.214	36.090	222.400	353.005
50	17.032	3.472	82.111	0.004	30.997	37.039	1010.800	758.242
51	17.226	4.579	63.376	0.003	31.762	38.520	389.800	461.001
52	18.395	3.494	61.020	0.002	31.602	39.876	315.500	469.691
53	16.745	4.442	63.295	0.004	26.826	33.194	645.600	634.822
54	16.789	3.792	69.294	0.001	26.297	39.680	115.410	272.341
55	15.770	3.771	115.937	0.005	29.250	34.691	1767.400	708.143
56	17.439	4.553	76.639	0.003	25.477	32.791	414.900	483.568
57	18.116	4.243	100.250	0.002	34.648	42.391	288.500	475.552
58	18.501	4.302	105.979	0.002	32.924	40.904	288.100	450.327
59	18.260	3.659	81.167	0.002	26.364	35.285	327.200	423.003
60	17.192	4.363	84.192	0.005	34.978	40.179	1005.400	750.126
61	18.294	3.754	94.979	0.004	34.283	40.006	944.200	820.389
62	18.312	4.189	76.978	0.003	29.737	36.625	479.500	483.039
63	18.212	4.126	102.378	0.004	26.601	32.832	821.600	623.164
64	17.357	3.413	89.551	0.002	33.550	41.470	373.200	590.014
65	15.943	4.634	67.964	0.002	31.128	39.464	217.500	330.128
66	15.244	3.720	101.549	0.004	25.676	31.863	1196.700	598.685
67	16.911	4.954	62.944	0.002	28.998	37.581	192.180	332.257
68	18.832	3.222	97.152	0.003	31.894	38.601	764.800	855.716
69	18.578	4.041	94.685	0.002	30.358	38.676	300.700	323.621
70	16.530	4.597	86.188	0.003	29.613	36.514	425.800	555.335
71	16.230	4.986	85.751	0.002	25.973	34.945	213.800	362.469
72	16.317	3.318	117.091	0.005	26.978	32.542	2215.000	739.948
73	15.831	3.676	61.907	0.005	25.205	31.191	1234.800	519.268
74	15.241	3.034	107.193	0.004	29.566	35.533	1714.200	665.436
75	16.411	4.865	60.837	0.003	27.852	35.009	356.700	433.357
76	18.911	3.752	97.347	0.004	26.332	32.591	923.900	843.021
77	17.352	4.746	74.141	0.004	27.443	33.700	593.700	628.875
78	15.788	4.360	109.707	0.005	28.971	34.429	1336.700	670.938
79	18.738	4.393	91.990	0.001	28.375	40.921	106.630	331.363
80	16.302	3.300	118.704	0.002	27.691	36.360	508.100	377.683
81	15.613	4.662	68.259	0.003	29.716	36.684	393.100	450.208
82	17.990	4.819	68.962	0.002	29.375	37.896	211.000	435.330
83	18.257	3.485	85.100	0.004	27.764	33.950	989.600	663.482
84	16.409	3.996	111.769	0.004	25.426	31.666	1050.500	540.502
85	17.711	3.439	89.154	0.001	27.027	40.088	146.490	273.724
86	15.082	4.940	94.585	0.004	25.848	32.076	699.100	570.364
87	16.904	4.553	115.275	0.001	29.172	41.379	115.410	331.123
88	18.340	4.063	94.891	0.003	29.264	36.144	529.800	601.874
89	17.858	4.219	70.574	0.004	26.336	32.656	696.800	629.961
90	17.601	4.347	75.132	0.002	25.654	34.718	249.400	259.466
91	16.253	4.085	66.334	0.001	25.278	39.090	102.300	238.130
92	16.564	4.824	81.703	0.003	25.307	32.581	392.300	377.788
93	18.931	3.634	103.627	0.005	25.167	30.913	1401.100	852.255
94	15.942	4.575	118.066	0.003	26.482	33.546	553.700	362.913
95	17.807	3.072	117.137	0.003	26.643	33.717	1050.700	626.983
96	17.540	4.622	93.006	0.003	27.165	34.243	435.500	567.289
97	15.357	3.346	106.482	0.004	28.760	34.790	1470.600	777.871
98	17.909	3.538	96.843	0.002	29.410	37.908	375.300	376.841
99	15.500	3.188	100.652	0.001	25.041	38.854	184.440	305.752



100	16.736	4.886	77.204	0.005	29.515	35.082	825.200	636.880
101	16.376	4.506	69.002	0.002	30.250	38.668	231.400	366.474
102	17.450	3.405	77.845	0.003	33.984	40.571	663.100	724.505
103	17.583	4.056	102.078	0.004	30.321	36.315	822.900	530.593
104	17.180	3.322	118.322	0.004	28.132	34.195	1534.800	629.804
105	18.740	4.693	90.565	0.002	33.077	41.011	240.400	455.279
106	15.700	4.123	71.314	0.001	29.016	41.321	101.950	257.184
107	18.582	3.478	80.304	0.002	28.340	36.995	352.100	495.193
108	16.048	4.447	113.198	0.002	29.342	37.755	308.000	435.136
109	16.643	4.588	83.609	0.004	30.930	36.883	656.700	569.754
110	16.506	3.878	112.408	0.001	34.868	44.849	144.860	400.807
111	17.919	4.189	73.997	0.002	34.125	41.978	258.400	359.224
112	18.619	4.008	104.805	0.002	26.222	35.135	315.900	393.092
113	16.949	3.934	66.801	0.003	33.287	39.951	505.800	393.633
114	15.179	3.619	63.214	0.001	27.557	40.522	114.230	309.007
115	18.767	3.814	70.376	0.002	26.647	35.577	291.500	359.231
116	17.178	4.298	82.004	0.003	28.686	35.697	469.000	559.142
117	18.172	4.697	101.998	0.001	28.482	40.939	101.410	373.228
118	17.995	3.682	94.037	0.003	29.865	36.753	616.000	586.298
119	15.879	4.117	67.301	0.004	25.641	32.122	735.700	654.468
120	15.691	4.228	111.285	0.003	27.798	34.732	617.300	465.509
121	15.788	3.506	115.613	0.002	29.302	37.756	459.300	528.143
122	18.297	4.883	72.786	0.002	26.071	35.048	205.200	422.641
123	18.479	3.451	83.226	0.001	28.823	41.142	139.710	335.505
124	17.854	3.348	63.556	0.004	29.261	35.465	985.700	794.710
125	18.612	4.934	95.682	0.005	28.705	34.229	852.500	695.774
126	17.302	4.554	61.335	0.004	34.295	40.141	599.300	656.943
127	18.071	3.196	69.046	0.002	34.617	42.416	378.900	529.898
128	16.958	4.972	106.046	0.001	33.265	43.868	94.160	310.102
129	16.997	3.576	79.387	0.003	30.446	37.324	615.400	717.649
130	15.932	3.738	71.057	0.005	29.593	35.219	1230.100	717.807
131	18.728	3.941	88.840	0.002	31.354	39.569	305.000	393.835
132	16.734	4.816	64.734	0.002	33.955	41.837	205.800	371.102
133	15.073	4.637	115.566	0.002	26.491	35.291	290.900	362.854
134	16.266	4.579	82.453	0.005	28.356	33.995	926.100	679.959
135	18.657	4.583	98.508	0.005	30.175	35.625	974.300	703.826
136	17.975	3.305	102.212	0.002	32.147	40.235	414.300	644.136
137	17.455	3.012	71.420	0.003	30.712	37.613	786.800	659.102
138	17.427	3.451	80.567	0.002	26.155	35.194	358.000	416.191
139	15.129	4.356	116.001	0.004	30.934	36.803	944.400	696.959
140	16.392	3.623	112.053	0.002	25.954	34.879	428.800	562.951
141	17.168	4.323	84.562	0.001	26.507	39.783	103.650	322.170
142	18.940	3.398	89.857	0.004	29.917	35.933	1057.500	807.603
143	17.099	3.417	116.907	0.001	33.425	43.926	182.700	397.594
144	17.228	4.796	101.795	0.005	32.922	38.220	892.800	752.283
145	17.742	3.259	81.473	0.004	32.732	38.580	789.700	720.330
146	18.490	4.132	92.237	0.001	27.888	40.582	116.530	374.713
147	17.905	3.793	96.880	0.004	26.019	32.321	918.000	693.157
148	18.393	3.832	78.313	0.004	34.567	40.306	832.700	667.956
149	18.843	3.300	60.575	0.003	28.434	35.444	636.400	666.584
150	18.470	3.429	108.489	0.004	32.812	38.648	1083.700	899.759
151	17.877	4.006	80.075	0.003	25.037	32.321	515.600	475.093
152	18.691	3.720	104.285	0.001	26.641	39.813	140.650	350.017
153	18.220	4.154	72.128	0.003	28.594	35.622	465.400	620.960
154	17.626	3.806	74.864	0.002	26.858	35.775	302.800	481.384
155	17.505	3.977	77.652	0.005	31.161	36.659	1140.500	747.437

---

156	16.517	4.192	68.989	0.004	34.450	40.269	718.800	666.038
157	16.763	3.462	119.846	0.004	27.761	33.840	1438.700	752.955
158	17.566	4.854	109.381	0.002	28.964	37.464	237.400	367.733
159	15.352	4.889	119.036	0.003	32.370	38.971	499.800	423.569
160	18.082	4.912	97.656	0.002	29.085	37.614	232.300	497.921

---

# LIST OF PUBLICATIONS

---

---

## International Journals

### Published

1. Monika K, Punnoose EM, Datta SP. Multi-objective optimization of cooling plate with hexagonal channel design for thermal management of Li-ion battery module. **Applied Energy** 2024;368. (Elsevier, IF: 11.2).
2. Monika K, Phani Vivek UVV, Chakraborty C, Roy S, Datta SP. Augmentation of multi-stage Tesla valve design cold plate with reverse flow to enhance thermal management of pouch batteries. **International Journal of Heat and Mass Transfer** 2023;214. (Elsevier, IF: 5.2).
3. Monika K, Datta SP. Comparative assessment among several channel designs with constant volume for cooling of pouch-type battery module. **Energy Conversion and Management** 2022; 251:114936. 251, 114936. (Elsevier, IF: 10.4).
4. Monika K, Chakraborty C, Roy S, Sujith R, Datta SP. A numerical analysis on multi-stage Tesla valve based cold plate for cooling of pouch type Li-ion batteries. **International Journal of Heat and Mass Transfer** 2021; 177:121560. (Elsevier, IF: 5.2).
5. Monika K, Chakraborty C, Roy S, Dinda S, Singh SA, Datta SP. An improved mini-channel based liquid cooling strategy of prismatic LiFePO<sub>4</sub> batteries for electric or hybrid vehicles. **Journal of Energy Storage** 2021; 35:102301. (Elsevier, IF: 9.4).

6. Monika K, Chakraborty C, Roy S, Dinda S, Singh SA, Datta SP. Selection of an Ideal Coolant to Ward off the Thermal Runaway of Pouch Type Li-ion Battery Module. **Journal of Electrochemical Energy Conversion and Storage** 2021; 18:1–42. (ASME, IF: 2.5).
7. Monika K, Chakraborty C, Roy S, Dinda S, Singh SA, Datta SP. Parametric investigation to optimize the thermal management of pouch type lithium-ion batteries with mini-channel cold plates. **International Journal of Heat and Mass Transfer** 2021; 164:120568, (Elsevier, IF: 5.2).

#### **To be communicated**

1. K. Monika, S. P. Datta, Explore the Efficacy of Indirect Liquid Cooling Approach with Mini Channel Cold Plates for Pouch Cells, **Applied Thermal Engineering** (Elsevier, IF: 6.4).
8. Monika K, Trivedi GVN, Parameshwaran R, Datta SP. Experimental investigation of thermal management system coupling phase change material with liquid cooling for pouch-type Li-ion batteries, **Energy Conversion and Management** (Elsevier, IF: 10.4).

#### **International Conferences**

1. K. Monika, S. P. Datta, S. Roy, C. Chakraborty, S. Dinda, S. A. Singh, Investigation of micro channeled cooling plate on the thermal behaviour of li-ion battery module, **Proceedings of the 27th National and 5th International ISHMT-ASTFE Heat and Mass Transfer Conference, 14<sup>th</sup>–17<sup>th</sup> December, 2023, IIT Patna, Patna-801106, Bihar, India.**

2. K. Monika, S. P. Datta, S. Roy, C. Chakraborty, S. Dinda, S. A. Singh, Numerical Analysis of Spiral Channelled Cooling Plates for Thermal Management of Pouch Battery Module, **Proceedings of the 26th National and 4th International ISHMT-ASTFE Heat and Mass Transfer Conference, 17<sup>th</sup>–20<sup>th</sup> December, 2021, IIT Madras, Chennai-600036, Tamil Nadu, India.**
3. K. Monika, S. P. Datta, S. Roy, C. Chakraborty, S. Dinda, S. A. Singh, An energy efficient thermal management strategy of prismatic Li-ion energy storage devices of hybrid vehicles, Proceedings of the **International Conference on Innovations in Thermo-Fluid Engineering and Sciences, 10<sup>th</sup>-12<sup>th</sup> Feb, 2020, NIT Rourkela, India.**

#### **Book Chapter**

1. Monika K, Saraswati R, Chakraborty C, Roy S, Datta SP, Nanostructured, Materials Engineering and Characterization for Battery Applications **2024**, 1st Edition, **Elsevier**, **Paperback ISBN: 9780323913041, eBook ISBN: 9780323914215.**

## **BRIEF BIOGRAPHY OF THE CANDIDATE**

---

---

*Kokkula Monika* is a doctoral student from the department of mechanical engineering at BITS Pilani, Hyderabad Campus, India. Before joining PhD, she worked as an assistant professor for 3 years at Chaitanya Bharati Institute of Technology, Hyderabad, India, from February 2016 to January 2019. She received her master's degree in mechanical engineering with a specialization in thermal engineering from JNTU College of Engineering, Hyderabad, India, in September 2015. She received her bachelor's degree in mechanical engineering from St. Martins Engineering College, India, in August 2013. Her research interests include thermal management, phase change materials and computational fluid dynamics.

## **BRIEF BIOGRAPHY OF THE SUPERVISOR**

---

---

*Prof. Santanu Prasad Datta* is presently serving as an Associate professor in the Department of Mechanical Engineering at BITS Pilani, Hyderabad Campus. He received his PhD degree in mechanical engineering from the Indian Institute of Technology, Kharagpur, India, based on the research carried out in automotive air conditioning systems. His research interests include refrigeration and air-conditioning, hybrid vehicle thermal management, energy and environment impact on society, compact heat exchangers, evaporative cooling and experimental thermo-fluid science. He obtained the certificate of commendation in the 7th Bry-Air Awards for excellence in HVAC&R in the student category in 2011 to 2012, a nationwide competition on innovation in HVAC system design supported by Bry-Air. He received the SERB early career research grant and the DST young scientist research grant to pursue cutting-edge research in applied thermal engineering. As an outcome of his present and past research contribution, he is having more than 28 international journal papers, 1 book chapter and 1 national patent in filing stage.

## **BRIEF BIOGRAPHY OF THE CO-SUPERVISOR**

---

---

*Prof. Sounak Roy* is presently serving as a Head and Professor in the Department of Chemistry, BITS Pilani, Hyderabad Campus, India. He received his PhD degree from the Indian Institute of Science, Bangalore, India, in 2008. Later, he worked as a Post-Doctoral fellow at ETH, Zurich, Switzerland, from 2008 to 2010, followed by the University of Pennsylvania and University of Delaware, USA from 2010 to 2012. His research interests include solid-state chemistry, energy and environmental catalysis, and understanding the reaction mechanism in light of structure-property relationships. Currently, his group is engaged in the area of NO<sub>x</sub> abatement, conversion of CO<sub>2</sub> to biofuels, water splitting and fuel cells.